Title
Transport Phenomena in Liquid Foams and Liquid Marble Colloids

Author
Attia, Joseph

Publication Date
2016

Peer reviewed|Thesis/dissertation

University of California
Los Angeles

Transport phenomena in liquid foams and liquid marble colloids

A dissertation submitted in partial satisfaction
of the requirements for the degree
Doctor of Philosophy in Mechanical Engineering

by

Joseph Ahmed Attia

2016

Abstract of the Dissertation

Transport phenomena in liquid foams and liquid marble colloids

by

Joseph Ahmed Attia

Doctor of Philosophy in Mechanical Engineering

University of California, Los Angeles, 2016

Professor Laurent Pilon, Chair

Liquid foams consist of randomly packed bubbles separated by a thin liquid fluid. They can be found in various industrial applications including separation processes, oil recovery, water treatment, food, and material processings. They are also being considered as coolant in heat exchangers systems for heat transfer enhancement compared with single-phase air. Similarly, liquid marbles, a phase inversion of liquid foams, consisting of a liquid core stabilized by closely packed solid hydrophobic particles, have shown significant promise as functional materials exploiting their photoresponsive behavior. In all of the above mentioned applications, it is necessary to further the current understanding of transport phenomena, such as heat, mass, and radiation transfer, in liquid foam and liquid marble systems.

First, the effects of Ostwald ripening or inter-bubble gas diffusion on the steady-state thickness of aqueous foams were investigated. The governing equation for the time rate of change of bubble radius in the liquid foam accounting for Ostwald ripening was derived and non-dimensionalized. A dimensionless similarity parameter representing the ratio of the average contact time between bubbles to the characteristic time for gas permeation was identified. This dimensionless number was combined with two previously identified dimensionless numbers accounting for viscous, gravitational, and capillary forces. A semi-empirical model predicting the steady-state height of liquid foam was developed based

on experimental data for liquid foams generated by sparging different gases through a porous frit into an aqueous surfactant solution contained in a glass column.

Moreover, the stability of liquid foams exposed to normally incident thermal radiation was experimentally investigated. Here again, liquid foams were generated by injecting air into an aqueous surfactant solution contained in a glass column. Results demonstrated that the steady-state foam height decreased with increasing radiative heat flux. This was attributed to the effects of the foam temperature-dependent thermophysical properties and to liquid evaporation at the top of the foam layer. In addition, a one-dimensional reduced-order thermal model accounting for combined conduction and radiation within the steady-state foam agreed reasonably well with temperature measurements taken across the foam layer.

Furthermore, experimental data and scaling analysis for laminar forced convection of liquid foams flowing in circular and rectangular tubes as well as in tube bundles were reported. First, aqueous solutions of surfactant Tween 20 with different concentrations were used to generate microfoams with various porosity, bubble size distribution, and two-phase pseudoplastic (shear thinning) power-law fluid behaviors. These different microfoams were flowed laminarly in uniformly heated circular tubes of different diameter instrumented with thermocouples. A wide range of heat fluxes and flow rates were explored. Experimental data were compared with analytical and semi-empirical expressions derived and validated for single-phase power-law fluids. These correlations were extended to two-phase foams by defining the Reynolds number based on the effective viscosity and density of microfoams. However, the local Nusselt and Prandtl numbers were defined based on the specific heat and thermal conductivity of water. Indeed, the heated wall was continuously in contact with a film of water controlling convective heat transfer to the microfoams. Overall, good agreement between experimental results and model predictions was obtained for all experimental conditions considered. Finally, the same approach was shown to be also valid for experimental data reported in the literature for laminar forced convection of microfoams in rectangular minichannels and of macrofoams

across aligned and staggered tube bundles with constant wall heat flux.

Finally, the radiation characteristics of liquid marbles made of an aqueous core stabilized by a coating of highly hydrophobic and closely packed monodisperse non-absorbing or absorbing particles were predicted numerically using the superposition T-matrix method and the geometric-optics surface-waves (GOS) method. Particular attention was paid to the effects of the liquid marble's core and coating optical properties, size parameter, and core-to-coating particle radii ratio on their absorption and scattering cross-sections and on the asymmetry factor. Results were compared with predictions by the Lorenz-Mie theory for (i) the water core alone, (ii) the volume and projected area equivalent coated sphere, and (iii) the dimensionally equivalent coated sphere.

The dissertation of Joseph Ahmed Attia is approved.

Nasr Ghoniem

Gaurav Sant

Adrienne Lavine

Laurent Pilon, Committee Chair

University of California, Los Angeles

2016

Table of Contents

List of Figures

List of Tables

Acknowledgments

The path toward my doctoral degree has been especially difficult given my family and work responsibilities away from graduate work. Nonetheless, I am very thankful for the opportunity to pursue my doctorate as it has undoubtedly strengthened my technical acumen and left a valuable mark on my life. First and foremost I would like to thank my adviser, Professor Laurent Pilon, for his guidance, persistence, patience, flexibility given my family and work obligations, and most importantly his encouragement. I highlight his encouragement because he has always pushed me to be better researcher in terms of rigor and standard, and these lessons have carried into other areas of my life aside from academic research, namely, my professional career in industry. Secondly, I would like to thank my doctoral committee members, Professors Nasr Ghoniem, Adrienne Lavine, and Gaurav Sant. Additionally, I would like to acknowledge my fellow students, Hainan Wang, Ian Mckinley, Ri-Liang Heng, and Cenlin He for useful discussions and direction toward completing the work in this thesis. Likewise, I would like to thank my friends outside of the academic setting, specifically, Saken Sherkanov, Habib Ahmad, Rafed Al-Huq, Ivan La Frinere-Sandoval, Mansur Wadalawala, Robert Robertson, and Yernur Rysmagambetov. Moreover, this work would not have been completed without the support and patience of my loving wife Summer. She was and still is my ultimate source of support. Finally, I would like to dedicate this dissertation to my daughters Nabila and Sarah.

Vita

2006	B.S., Mechanical Engineering California Institute of Technology Pasadena, CA
2008	M.S., Mechanical Engineering University of California Los Angeles Los Angeles, CA
2008-2013	Senior Systems Engineer Raytheon Space and Airborne Systems El Segundo, CA
2013-2015	Senior Mechanical Engineer Los Angeles Metropolitan Transportation Authority Los Angeles, CA
2015-present	Propulsion Reliability Engineer Space Exploration Technologies Hawthorne, CA

Publications

J.A. Attia, I.M. Mckinley, D. Moreno-Magana and L. Pilon, Convective heat transfer in foams under laminar flow in pipes and tube bundles, International Journal of Heat and Mass Transfer, Vol. 55, pp. 78237831, 2012.

J.A. Attia, S. Kholi, and L. Pilon, Scaling laws in steady-state aqueous foams including

Ostwald ripening, Colloids and Surfaces A: Physicochemical and Engineering Aspects, Vol. 436, pp. 1000-1006, 2013.

J.A. Attia, C. He, K.N. Liou and L. Pilon, Absorption and Scattering by Liquid Marbles, Journal of Quantitative Spectroscopy and Radiative Transfer, Submitted, 2016.

CHAPTER 1

Introduction

This chapter highlights the motivations for this study. First, it provides a background on traditional liquid foams and microfoams, including how they are generated, their prevalence in industrial applications, and potential areas where they may also be utilized. Similarly, liquid marble colloids are presented as well as applications using their unique optical radiative properties. Finally, the chapter concludes with a brief statement regarding the specific objectives of the study and the organization of this document.

1.1 Motivations

1.1.1 Liquid foams

Liquid foams are a random assembly of gas bubbles separated by a thin film of liquid. They can be generated by injecting gas bubbles into a foaming solution. Bubbles can also be generated chemically within the foaming solution and then rise to its surface where they accumulate. The bubbles within the foam can assume polyhedral or spherical shapes of different sizes. The shape and size of bubbles in foams are affected by various physical phenomena including (i) liquid drainage under the effect of gravity and capillary pressure, (ii) bubble coalescence, and (iii) interbubble gas duffusion also known as Ostwald ripening or coaresning. In fact, small bubbles tend to be spherical and located at the bottom of the foam while large bubbles tend to be polyhedral and located at the top. As bubbles rise through the foam, they may coalesce with adjacent ones. In addition, Ostwald ripening results in large bubbles growing at the expense of smaller adjacent ones. This

phenomenon become important in foams made of low viscosity liquid where liquid films separating the bubbles tend to be thin, particularly near the top, as illustrated in Figure 1.1.

Liquid foams are an important component of numerous technologies including petrochemical [17], pharmaceutical [18], food [19, 20], and water treatment [21], as well as glass [22], iron, and steel manufacturing [23–25]. Depending on the application, foams may prove either beneficial or detrimental. In water treatment, for example, foam is generated by injecting gas bubbles into wastewater and is collected to separate organic waste (i.e., proteins) or impurities from water streams [21]. In such separation processes, foaming agents are typically utilized to achieve faster separation and easier waste disposal [21]. Understanding foam formation and stability is essential for predicting and controlling foam behavior in these various processes.

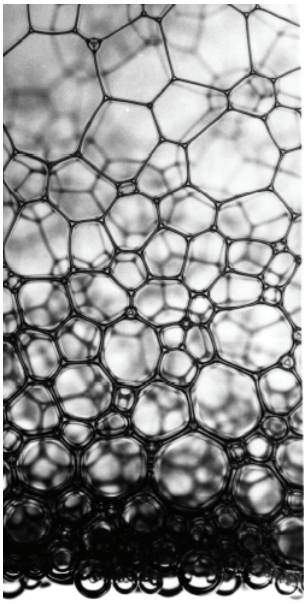

Figure 1.1: Photograph of aqueous foams (courtesy of D. Durian, UPenn, USA).

Microfoams are another class of liquid foams consisting of tightly packed spherical bubbles with diameter between 10 and 100 μm and porosity of up to 70% [26]. These

microfoams can be produced by spinning a disk at 5,000 to 10,000 rpm in an aqueous surfactant solution contained in a baffled beaker at room temperature [26]. Such microfoams have also been termed colloidal gas aphrons (CGA) [26]. However, the multiple surfactant-shell structure forming around individual bubbles proposed by Sebba [26] has not been directly and unequivocally observed [27]. Microfoams have found numerous applications including separation processes [28, 29], soil remediation [30, 31], water treatment [32,33], and biotechnology [34]. These applications take advantage of (i) their large interfacial area, (ii) the adsorption of particles at the microbubble interfaces, and (iii) their stability for enhanced mass transfer [35]. Traditional macrofoams are commonly used as fire suppressant [36]. But microfoam made from mixtures of anionic and cationic surfactants have also been shown to spread over a pool of burning gasoline and to extinguish fire [26]. Therefore, for these applications, understanding the effects of radiant heating on the stability of liquid foams is essential.

Moreover, liquid foams have also been used as a fracturing fluid for improved oil recovery. Here, convective heat transfer takes place between the hot rock formation and the colder injected foams [37]. They have also been considered as a working fluid in heat exchangers to take advantage of the fact that the associated heat transfer coefficient is significantly larger than that achieved using air for the same conditions [14,15]. This could reduce the size and mass of air-based heat exchangers. However, in order to effectively implement this approach, it is necessary to develop models for accurately predicting convective heat transfer complicated by the fact that liquid foams are two-phase shear-thinning pseudoplastic fluids.

1.1.2 Liquid marbles

A phase inversion of traditional liquid foams, is known as "liquid marbles." Liquid marbles are liquid droplets stabilized by a coating of highly hydrophobic and closely packed monodisperse particles [38]. Liquid marbles act as soft solids with excellent non-wetting and non-adhesive properties relative to various surfaces [38–40]. In certain instances, they

exhibit near powder-like fluid properties such as in the case of water droplets stabilized by silica particles also known as dry water [41, 42] as illustrated Figure 1.2. They can be formed by mixing hydrophobic particles in a liquid or by rolling a droplet of liquid across a bed of hydrophobic particles [38, 40, 43, 44]. The liquid marble core diameter is typically on the order of 1 mm while the spherical particles, constituting the coating, are 0.1 - 100 μm in diameter [43].

Liquid marbles have been synthesized with a variety of particle coatings including lycopodium powder, silica, latex, carbon black, carbon nanotubes, and polymer lattices [16, 38]. They can be adapted to a variety of liquid cores for various applications by selecting the material and size of the coating particles.

Figure 1.2: Photograph of liquid marbles about 1 mm in diameter (courtesy of S. Fujii, Osaka Institute of Technology, Japan).

A number of stimuli-responsive liquid marbles have emerged in recent years for sensing and delivery applications [16, 45–47]. Fujii *et al.* [46] prepared liquid marbles from pH-responsive sterically stabilized latex particles. The authors prepared the liquid marbles by rolling water droplets, 15 μL to 2 mL in volume, on a bed of pH-responsive polystyrene latex monodisperse particles, approximately 0.44 μm in diameter. The liquid marbles remained stable when placed on the surface of a liquid with pH $>$ 8. By contrast, they disintegrated when placed on acidic liquid solutions. Another class of

liquid marbles include photoresponsive liquid marbles wherein the hydrophobic coating becomes hydrophillic when irradiated with ultraviolet, visible, or near-infrared radiation [39, 48–50]. Recently, Tan *et al.* [39] exploited the photocatalytic behavior of TiO_2 to create liquid marbles that disintegrated when irradiated with ultraviolet radiation. The same authors have also explored visible light-responsive liquid marbles [39]. Other functional photocatalytic materials, such as WO_3, CeO_2, and ZnO can be readily used to create photoresponsive liquid marbles for delivery and sensing applications or droplet manipulation in optofluidic systems [50].

The majority of liquid marble systems reported in the literature possess an aqueous liquid core. However, liquid metal cores have also recently been explored [51,52]. Tang *et al.* [52] demonstrated photochemical actuation of liquid metal marbles formed by encasing a liquid metal droplet of galinstan with WO_3 nanoparticles. The liquid metal marbles were placed in a hydrogen peroxide (H_2O_2) solution, and exposed to ultraviolet radiation. The photocatalytic behavior of the WO_3 coating led to decomposition of H_2O_2 and the generation of oxygen bubbles in the immediate vicinity of the illuminated area on the liquid metal marble surface. The oxygen bubbles induced a rolling motion of the liquid metal marble, pushing it away from the light source.

Moreover, Taylan and Berberoğlu [42] investigated thermal radiation transport in dry water systems considered for fire suppression applications. The authors approximated a dry water particle consisting of an aqueous core of radius R_w coated with hydrophobic silica particles of radius r_s as a coated sphere with a core of radius R_w and a shell of radius $R_w + 2r_s$. The absorption and scattering cross-sections and the scattering phase function of the dry water particles were calculated from Lorenz-Mie theory for coated spheres [53]. Although intuitive, this dimensionally equivalent coated sphere approximation has not been rigorously validated.

In all of the above applications, understanding and predicting radiation transfer in liquid marbles is important for designing and controlling their behavior and performance.

1.2 Objectives of present study

Liquid foams are already present in a wide range of industrial applications and could be used in other areas such as heat exchanger systems. Likewise, liquid marbles present themselves as a novel functional photoresponsive material for sensing and opto-fluidic applications. The main objective of the present study is to develop predictive and experimentally validated physical models for transport phenomena in liquid foams and liquid marble colloids, including mass, heat, and radiation transfer. This includes (i) developing a physical model for predicting the steady-state height of low viscosity foams affected by Ostwald ripening, (ii) assessing the effects of thermal radiation on transient and steady-state aqueous foams, (iii) developing a thermal model for predicting convective heat transfer in liquid foams in pipes and tube bundles, and (iv) numerically predicting radiation characteristics of liquid marbles of various morphologies and optical properties.

1.3 Organization of this document

Chapter 2 presents a dimensional analysis of the governing equation for the time rate of change of bubble radius in liquid foams accounting for Ostwald ripening leading to the prediction of the steady-state thickness of foams made of low viscosity liquids. Chapter 3 presents experimental measurements and thermophysical modeling of the height and temperature profile in steady-state aqueous foams exposed to thermal radiation. Chapter 4 presents experimental measurements and dimensional analysis for laminar forced convection of liquid foams and microfoams flowing in circular pipes, rectangular pipes, and across different tube bundle arrangements. Chapter 5 presents detailed numerical simulations of light scattering and absorption by liquid marbles stabilized by either non-absorbing or absorbing coatings exposed to visible and infrared radiation. Finally, Chapter 6 summarizes the main contributions of this work.

CHAPTER 2

Scaling Laws in Steady-State Aqueous Foams Including Ostwald Ripening

This chapter presents scaling laws governing the steady-state behavior of pneumatic foams produced by injecting gas in low viscosity surfactant solutions under isothermal conditions and subjected to Ostwald ripening.

2.1 Introduction

Numerous physical phenomena occur in liquid foams such as liquid drainage, bubble coalescence, Ostwald ripening, and even liquid evaporation [8, 54]. Liquid drainage is typically driven by gravitational forces acting on the liquid phase in the foam and is opposed by viscous forces at the plateau borders. Moreover, liquid drainage eventually subsides when capillary forces balance with the effects of gravity. Bubble coalescence and Ostwald ripening are most dominant in aqueous foams due to their relatively low viscosity.

Figure 2.1 summarizes the main phyiscal phenomena occuring in liquid foams. Low viscosity (i.e. ≤ 1.0 mPa/s) foams tend to have bubbles separated by thin and unstable liquid films, making them more susceptible to bubble coalescence and Ostwald ripening [55–58]. The combination of these two phenomena has been termed "foam coarsening." On the one hand, bubble coalescence occurs when two adjacent bubbles merge as a result of rupture of the films separating them [59].

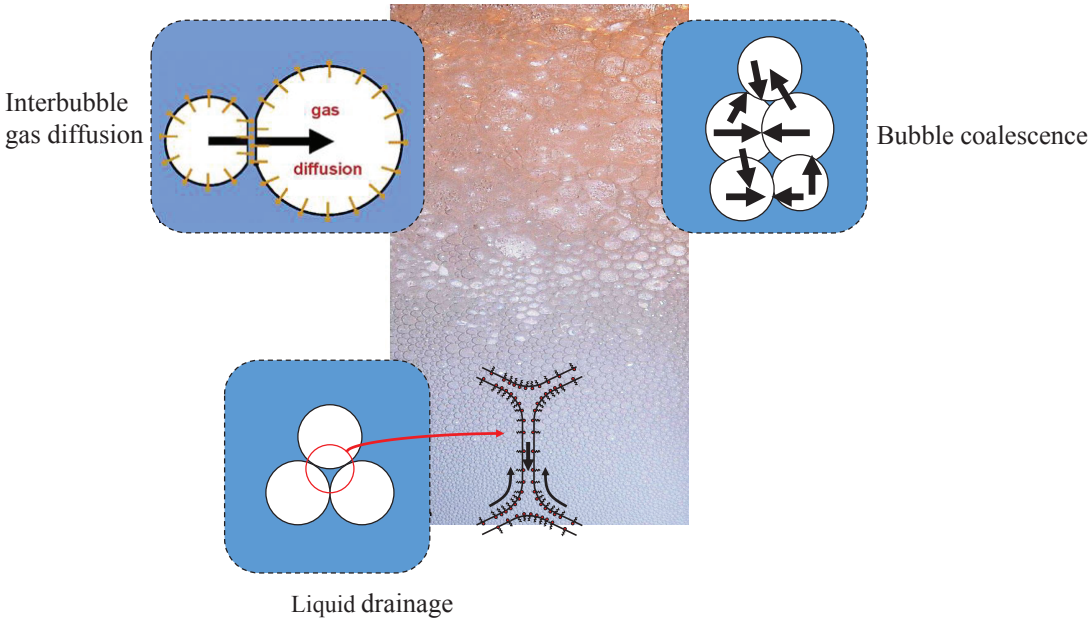

Figure 2.1: Different physical phenomena occurring in liquid foams, namely (a) liquid drainage, (b) bubble coalescence, and (c) interbubble gas diffusion.

This process simultaneously increases the mean bubble size while decreasing the number of bubbles and the liquid-gas interfacial area. On the other hand, Ostwald ripening, also called interbubble gas diffusion or disproportionation, describes mass transfer from small bubbles with higher internal pressure to large bubbles at lower pressure [60]. It causes larger bubbles to grow at the expense of smaller ones. These larger bubbles are less stable and separated by thinner liquid films, making them more prone to coalesce [56–58]. They then burst and discharge the liquid contained in the film which drains through the foam. Ostwald ripening is enhanced when the solubility and the diffusion coefficient of the gas in the liquid phase are large [57, 60, 61].

At early times in the foam's life, bubbles accumulate at the liquid surface surrounded by relatively thick liquid films. The foam grows at its largest rate as no bubble burst at the top. In this phase, mass balance of the gas phase in the foams leads to the following

expression for the transient foam thickness $H(t)$ [1]

$$H(t) = \frac{j}{\bar{\phi}}t \qquad \text{with} \qquad \bar{\phi}(t) = \frac{1}{H(t)}\int_0^{H(t)} \phi(z,t)\mathrm{d}z \tag{2.1}$$

where j is the superficial gas velocity (in m/s) and $\bar{\phi}$ is the average foam porosity while $\phi(z,t)$ is the local foam porosity at height z and time t [1]. The latter was suggested to be taken as 0.82 for all practical purposes [1]. As the foam ages and liquid drainage takes place, adjacent bubbles are more prone to coalesce when the film separating them is thin and more likely to rupture. This phenomenon dominates at the top of the foam column where the bubbles are the oldest and the foam is dry [62]. Soon after the first bubbles burst at the top of the foam which reaches a steady-state height H_∞ when the incoming flow of gas at the bottom of the foam matches the amount of gas released by bubbles bursting at the top.

Moreover, Pilon *et al.* [55] investigated the behavior of liquid foams formed by injecting gas bubbles into viscous fluids under steady-state and isothermal conditions. The authors performed a scaling analysis of the governing equation for the time-dependent foam thickness [62]. The model accounted for the effects of viscous, gravitational, and capillary forces. However, it neglected both bubble coalescence and interbubble gas diffusion because the viscosity of the fluid was large and the films separating the bubbles was consequently thick and relatively stable. Two dimensionless numbers were identified as describing the steady-state behavior of liquid foams generated from high viscosity liquids [55],

$$\Pi_1 = \frac{\rho g r_0^2}{\mu(j - j_m)} \qquad \text{and} \qquad \Pi_2 = \frac{\mu H_\infty (j - j_m)}{\sigma r_0} \tag{2.2}$$

where ρ and μ are the fluid density and dynamic viscosity, respectively. The average bubble radius at the bottom of the foam and the steady-state foam thickness are denoted by r_0 and H_∞, respectively, while j is the superficial gas velocity and j_m is the minimum superficial gas velocity for onset of foaming [63]. The dimensionless parameter Π_1 can be interpreted as the ratio of the gravitational force to the viscous force on an average bubble of radius r_0 having a velocity $(j - j_m)$. Similarly, Π_2 corresponds to the ratio

of the viscous force to the surface tension force multiplied by the ratio H_∞/r_0 scaling the steady-state foam height by the average bubble radius. The relationship between Π_1 and Π_2 was assumed to follow the power-law relation $\Pi_2 = K\Pi_1^n$ where empirical coefficients K and n were found to be 2905 and -1.8, respectively, from more than 120 experimental data points for foams formed from high viscosity liquids such as water containing glycerine, molten slag, and glass [55]. Bubbles were formed by injecting nitrogen, air, or argon through single, multi-orifice nozzles, or a porous medium. The experimental data featured a wide range of physicochemical properties, types of gas, bubble radius, and gas flow rates. Comparison between the developed semi-empirical correlation and the experimental data yielded reasonable agreements given the broad bubble size distribution around the mean value as well as uncertainties in H_∞, and in the thermophysical properties. For low viscosity fluids (e.g., aqueous surfactant solutions), however, the above correlation was shown to be inappropriate [2, 3]. Interestingly, the parameter K changed with the type of gas while n was almost the same and equal to -1.8 for all gases. Deviations from the correlation developed for highly viscous fluids was attributed to foam coarsening that becomes significant for low viscosity fluids but was neglected in the formulation of the governing equations leading to the definition of the dimensionless numbers Π_1 and Π_2.

The present study aims to demonstrate the existence of a third dimensionless similarity parameter governing steady-state aqueous foams accounting for Ostwald ripening. It will enable one to predict the steady-state thickness of aqueous foams from thermophysical properties of the liquid and gas phases and the operating conditions.

2.2 Experiments

Figure 2.2 depicts the experimental setup used in this study. Foam was generated by continuously injecting air through a fritted disc into a vertical glass column (Wilmad-Lab Glass) of diameter 50.8 mm and height 30.0 cm. The fritted disc located at the bottom

of the glass column was 4 mm thick, had coarse porosity (10-15 μm), and spanned the entire column cross-section. The aqueous surfactant solution was made by mixing sodium dodecyl sulfate (SDS) surfactant (99%, Fisher Scientific) in deionized water to achieve SDS mass fraction of 0.4 wt.% or 19.9 mg/l of water.

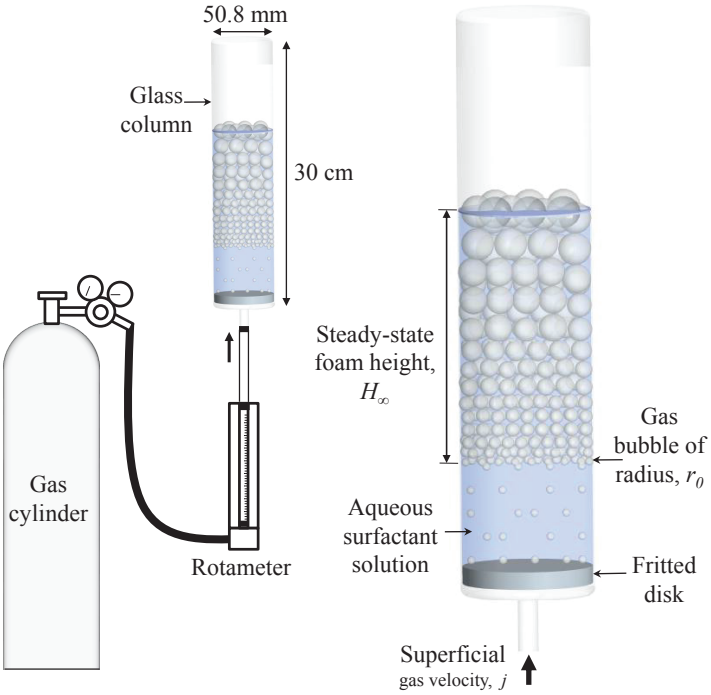

Figure 2.2: Schematic of the experimental setup used in this study to investigate aqueous foams.

The column and the fritted disc were thoroughly washed and the inner walls of the column were wetted before each measurement to ensure uniform wall conditions and remove any impurity that could obstruct the growth of the foam in the column. The column was filled with 136 mL of aqueous surfactant solution and dry air was bubbled through for several minutes to saturate the solution before starting the measurements. All measurements were performed at room temperature. The air flow rate was measured using an Omega FT-042-15-G1-VN rotameter. The foam height $H(t)$ was visually measured as a function of time using a laboratory grade scale mounted along the glass column. Photographs

of the gas bubbles at the bottom of the foam were taken with a Nikon D90 DSLR camera with a Nikon 55-200 mm VR lens. Image processing software (ImageJ) was used to determine the bubble size distribution at the bottom of the foam column. The associated experimental uncertainties were estimated to be (i) $\pm$ 13 mm for foam height $H(t)$ and H_∞ measurements and (ii) $\pm$ 0.1 mm for the bubble radii. Measurements of the foam thickness and bubble radius were repeated at least three times for each value of superficial gas velocity considered.

2.3 Analysis

Liquid drainage, bubble coalescence, and Ostwald ripening must take their course before the foam reaches a steady state. Experimentally it takes typically dozens of minutes to several hours to achieve steady-state conditions when generating foam in a bubble column [2, 64]. This time scale is on the same order of magnitude as the characteristic time for Ostwald ripening [60]. On the other hand, the characteristic time for coalescence is on the order of 1-10 minutes [60]. Experimental observations have also demonstrated that the type of gas had significant effect on the steady-state thickness of foams made from aqueous surfactant solutions [3]. These observations indicate that Ostwald ripening is an essential phenomenon controlling the steady-state foam thickness. The following assumptions were made in developing a physical model and the associated scaling analysis accounting for Ostwald ripening (1) isothermal conditions were maintained in the foam, (2) thermophysical properties of the gas and liquid phases remained constant within the foam, (3) the bubbles within the foam were treated as spherical.

2.3.1 Governing equation

The pressure difference between the gas inside a bubble of radius r and the liquid within the foam can be expressed as [58],

$$p_g - p_l = 2\sigma \left(\frac{1}{r_m} - \frac{1}{r} \right), \tag{2.3}$$

where p_g and p_l are the pressures in the gas and liquid phases, respectively. Here, r is the radius of the bubble of interest and r_m is the mean bubble radius defined as [58],

$$r_m(t) = \frac{\int_0^\infty r^2 f_1(r,t) \mathrm{d}r}{\int_0^\infty r f_1(r,t) \mathrm{d}r}, \tag{2.4}$$

where $f_1(r,t)$ is the bubble size distribution within the foam at time t. Bubble growth or shrinkage is determined from the difference between r and r_m, i.e., if $r > r_m$ the bubble grows while if $r < r_m$ the bubble shrinks.

Moreover, the molar mass transfer rate from a bubble of radius r to the liquid phase can be expressed as [58],

$$\frac{\mathrm{d}N}{\mathrm{d}t} = \frac{kA}{RT}(p_g - p_l), \tag{2.5}$$

where N represents the number of moles of gas within a bubble of radius r, while k is the effective gas permeability expressed in m/s. The surface area of the bubble is $A = 4\pi r^2$, while $R = 8.314$ J/mol.K is the universal gas constant and T is the absolute temperature. Combining Equations (2.3) and (2.5) yields,

$$\frac{\mathrm{d}N}{\mathrm{d}t} = \frac{8\pi k\sigma}{RT} \left(\frac{r^2}{r_m} - r \right). \tag{2.6}$$

Assuming that the gas inside the bubbles behaves as an ideal gas, the number of moles within a spherical bubble can be expressed as,

$$N = \frac{4\pi r^3 p_g}{3RT}. \tag{2.7}$$

Assuming that p_g is constant and slightly above atmospheric pressure, as suggested by Lemlich [58], and combining Equations (2.6) and (2.7) yields,

$$\frac{\mathrm{d}r}{\mathrm{d}t} = \frac{2k\sigma}{p_g} \left(\frac{1}{r_m} - \frac{1}{r} \right). \tag{2.8}$$

The effective gas permeability k from bubbles across liquid films was defined by Princen and Mason [65] and expressed in terms of the thermophysical properties of the gas and liquid phases as,

$$k = \frac{DS_O}{\delta_f + 2D/k_{ml}}, \tag{2.9}$$

where k_{ml} is the permeability of a monolayer of surfactants surrounding the bubble and δ_f is the thickness of the liquid film separating two adjacent bubbles. The diffusion coefficient of the gas in the liquid phase is denoted by D and is assumed to be constant. The Ostwald coefficient of solubility is denoted by S_O (dimensionless) and is defined as the volume of saturated gas absorbed by unit volume of pure liquid at given temperature and pressure [66].

Princen and Mason [65] simplified Equation (2.9) for two limiting cases: (i) when gas permeation is controlled by the surfactant monolayer, i.e. $\delta_f << 2D/k_{ml}$ and (ii) when gas permeation is controlled by the liquid layer or $\delta_f >> 2D/k_{ml}$. In the first case, the diffusivity or effect of interbubble gas diffusion is negligible. This is contrary to the pronounced effects of the gas type on the foam behavior observed in low viscosity fluid foams [3, 58]. Instead, one can assume that gas permeation is controlled by the liquid layer, i.e., $\delta_f >> 2D/k_{ml}$. The effective gas permeability k, therefore, simplifies to $k = DS_O/\delta_f$. Then, the time rate of change in bubble radius is expressed as,

$$\frac{\mathrm{d}r}{\mathrm{d}t} = \frac{2DS_O\sigma}{p_g\delta_f}\left(\frac{1}{r_m} - \frac{1}{r}\right). \tag{2.10}$$

Note that Equation (2.10) is similar to the expression for the time rate of change in bubble radius due to interbubble gas diffusion proposed by Lemlich [58] as,

$$\frac{\mathrm{d}r}{\mathrm{d}t} = \frac{2J\sigma RT}{p_g}\left(\frac{1}{r_m} - \frac{1}{r}\right), \tag{2.11}$$

where J is the effective gas permeability and was defined in terms of the volumetric fraction of liquid in the foam, the second and third moments of the bubble size distribution, the diffusion coefficient, and Henry's law constant [58].

2.3.2 Dimensional analysis

In order to scale Equation (2.10), the following independent dimensionless variables were introduced

$$r^* = \frac{r}{r_0}, \quad \sigma^* = \frac{\sigma}{p_0 r_0}, \quad \delta_f^* = \frac{\delta_f}{r_0}, \quad p_g^* = \frac{p_g}{p_0}, \quad \text{and} \quad t^* = \frac{t}{\tau_c} = \frac{t}{r_0/(j - j_m)} \tag{2.12}$$

where r_0 is the average bubble radius at the bottom of the foam layer [55] taken as the characteristic length, $\tau_c = r_0/(j - j_m)$ is the characteristic contact time between a rising bubble and a bubble at rest in the foam, and p_0 is the atmospheric pressure. Substituting Equation (2.12) into Equation (2.10) yields the following dimensionless governing equation,

$$\frac{\mathrm{d}r^*}{\mathrm{d}t^*} = \frac{2DS_O}{r_0(j - j_m)} \left[\frac{\sigma^*}{p_g^* \delta_f^*} \left(\frac{1}{r_m^*} - \frac{1}{r^*} \right) \right]. \tag{2.13}$$

Then, a third dimensionless number Π_3 accounting for interbubble gas diffusion can be identified as,

$$\Pi_3 = \frac{DS_O}{r_0(j - j_m)} = \frac{\tau_c}{\tau_d} \tag{2.14}$$

This dimensionless number can be interpreted as the ratio of the average contact time between bubbles in the foam $\tau_c = r_0/(j - j_m)$ and the characteristic permeation time defined as $\tau_d = {r_0}^2/(DS_O)$. It could also be expressed as $\Pi_3 = S_O/Pe_{r_0}$ where Pe_{r_0} is the Péclet number for mass transfer defined as the the ratio of advection and diffusion mass transfer rates.

The Buckingham-Pi theorem provides an alternative way of identifying Π_3. This approach is analogous to the treatment undertaken by Lotun and Pilon [67] in modeling slag foaming where the steady-state thickness H_∞ was assumed to depend on six variables namely ρ, g, μ, σ, $(j - j_m)$, and r_0. Their analysis led to four dimensionless numbers which can be combined to yield Π_1 and Π_2 given by Equation (2.2). Here, two additional variables, D and S_O, were introduced to account for Ostwald ripening. Two dimensionless groups were identified, in addition to the four dimensionless numbers derived by Lotun and Pilon [67]. The first new dimensionless group was identified as Π_5=S_O and the second

was Π_6=$\frac{D}{r_0(j-j_m)}$. Multiplying these two new dimensionless groups yields Π_3 given by Equation (2.14). Thus, both approaches give consistent dimensionless numbers. Finally, the relationship between Π_1, Π_2, and Π_3 is assumed to follow a power-law relation given by

$$\Pi_2 = L\Pi_1^n\Pi_3^m, \tag{2.15}$$

where L, n, and m are semi-empirical constants determined from experimental data.

2.4 Results and discussion

2.4.1 Experimental results

Figure 2.3 plots the temporal evolution of the average foam height for superficial gas velocity j equal to 0.015 and 0.018 mm/s. Each data point represents the average of at least three independent runs for each value of j. The error bars correspond to 95% confidence interval and indicate that measurements were reproducible from the transient foam growth to its steady state. Figure 2.3 also plots the transient foam height predicted by Equation (2.1) using $\bar{\phi} = 0.82$.

Good agreement between experimental data and model predictions was observed early in the foaming process. As previously mentioned, Equation (2.1) is based on the assumption that gas accumulates but does not escape the control volume defined by the foam. Despite interbubble gas diffusion, the gas remains within the foam. Thus, Ostwald ripening does not affect the early foam growth rate. However, it affects the time at which bubbles start bursting at the top of the foam. In fact, experimental data deviated from the model predictions as the foam approached its steady-state height H_∞. Moreover, the average residence time of a bubble in the foam can be estimated as H_∞/j which was equal to more than 2 hours for j=0.015 and 0.018 mm/s. This time scale confirms that Ostwald ripening played an important role in the steady-state behavior of the aqueous foams investigated.

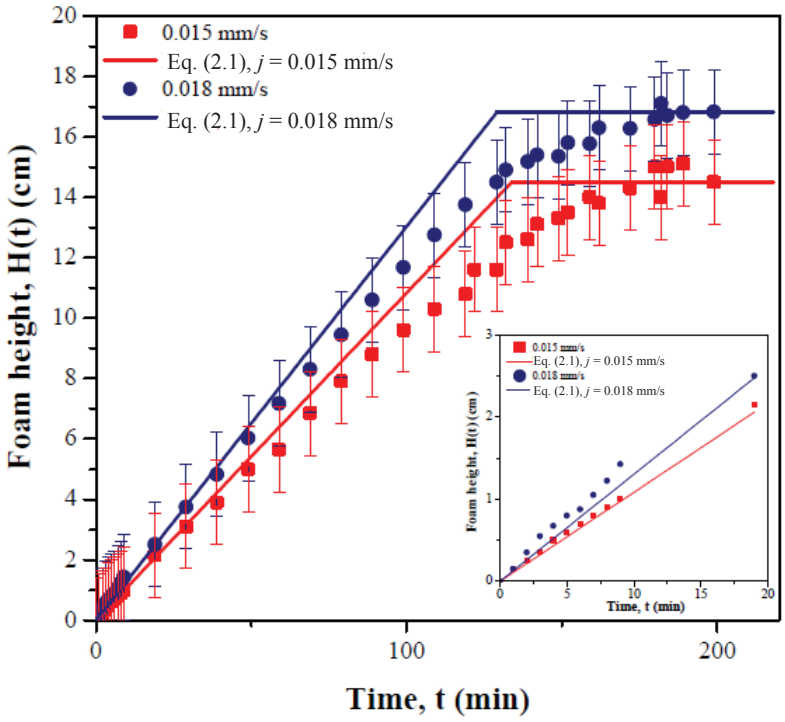

Figure 2.3: Evolution of foam height as a function of time and superficial gas velocity. Solid and dashed lines represent transient foam height model [1] as a function of superficial gas velocity.

2.4.2 Scaling analysis

The steady-state foam thickness data collected in the present study along with those reported in the literature [2–8] for foams made by injecting oxygen, nitrous oxide, nitrogen, xenon, air, or carbon dioxide gases into various aqueous surfactant solutions were used to validate the previously described scaling analysis. Table 2.1 summarizes the experimental conditions and the liquid and gas properties corresponding to these various studies. The viscosity of water at room temperature was estimated from the DIPPR database. The surface tension of the 0.4 wt.% SDS aqueous solution was reported to be 40.8 mN/m [68]. The Ostwald coefficient of solubility S_O for each gas in water at 293

K was reported by Hartland *et al.* [3]. The gas diffusion coefficient in water D was also reported by Hartland *et al.* [3] and calculated from the correlation developed by Wilke and Chang [69] accounting for the viscosity, temperature, and molecular weight of the gases. Additionally, the diffusion coefficient of carbon dioxide in water was reported by Feitosa *et al.* [4]. The properties of air were approximated as those of nitrogen.

Overall, the experimental data covered a wide range of physical parameters associated with the foam formation process, i.e., $0.02 \leq j \leq 0.78$ mm/s, $0.0 \leq j_m \leq 0.1$ mm/s, $0.1 \leq r_0 \leq 2.5$ mm, $1.26\times10^{-9} \leq D \leq 1.8\times10^{-9}$ m^2/s, $0.02 \leq S_O \leq 0.92$, and $31.1 \leq \sigma \leq 41.1$ mN/m corresponding to H_∞ varying between 26 and 1390 mm. Note that the experimental data considered focused exclusively on aqueous foams and do not present any significant fluctuations in viscosity ($\mu \approx 1.22$ mPa/s) and density ($\rho \approx 1014$ kg/m^3). A total of 51 different data points were collected resulting in dimensionless numbers Π_1 ranging from 602 to 122,625, Π_2 varying between 3×10^{-4} and 2.1×10^{-2}, and Π_3 from 1×10^{-5} to 6.2×10^{-2}.

Figure 2.4 plots Π_2 versus Π_1 for foams made by injecting various gases in aqueous surfactant solutions [2–8]. Unlike what was observed for high viscosity fluids [55], experimental data for aqueous foams did not collapse on a single line. However, the different data sets shows similar trend expressed as $\Pi_2 = K(\Pi_3)\Pi_1^n$ where the semi-empirical function $K(\Pi_3)$ depends on Π_3, i.e., $K(\Pi_3) = L\Pi_3^m$. Our previous study [55] estimated n to be -1.8 not only for both high viscosity fluids but also for low viscosity fluids albeit for a subset of the experimental data considered in the present study [2, 3]. Here, the datasets considered is much larger and broader and least squares fitting also yielded a value of n close to -1.8.

Table 2.1: Experimental conditions and thermophysical properties for different gases injected in aqueous surfactant solutions [2–8].

Aqueous solution of	Conc. (mg/l)	Gas	σ (mN/m)	μ (mPa·s)	ρ (kg/m^3)	D (m^2/s)	S_O	Ref.
10% glycerine+Marlophen 89	120	N_2	32.1	1.22	1014	1.45×10^{-9}	1.69×10^{-2}	
10% glycerine+Marlophen 89	80	N_2	35.4	1.22	1014	1.45×10^{-9}	1.69×10^{-2}	
10% glycerine+Marlophen 89	40	N_2	41.1	1.22	1014	1.45×10^{-9}	1.69×10^{-2}	[2]
10% glycerine+Marlophen 812	80	N_2	36.3	1.22	1014	1.45×10^{-9}	1.69×10^{-2}	
10% glycerine+Marlophen 89	120	N_2	32.1	1.22	1014	1.45×10^{-9}	1.7×10^{-2}	
10% glycerine+Marlophen 89	120	NO_x	31	1.22	1014	1.43×10^{-9}	67.6×10^{-2}	
10% glycerine+Marlophen 89	120	Xe	31.52	1.22	1014	1.26×10^{-9}	12.1×10^{-2}	[3]
10% glycerine+Marlophen 89	120	CO_2	31.13	1.22	1014	1.43×10^{-9}	91.9×10^{-2}	
0.4 wt.% AOS and 0.01 wt.% NaCl	–	CO_2	44.0	1.10	1000	1.80×10^{-9}	91.9×10^{-2}	[4]
0.4 wt.% AOS and 0.01 wt.% NaCl	–	CO_2	44.0	1.10	1000	1.80×10^{-9}	91.9×10^{-2}	[5]
Teepol	4120	Air*	40.0	1.0	1000	1.45×10^{-9}	1.69×10^{-2}	[6]
SDS	7800	Air*	36.3	1.0	1000	1.45×10^{-9}	1.69×10^{-2}	
5-O-dodecyl isosorbide sulfate a	2900	Air*	41.2	1.0	1000	1.45×10^{-9}	1.69×10^{-2}	[7]
SLE_2S	3500	Air*	39.6	1.0	1000	1.45×10^{-9}	1.69×10^{-2}	
SDS	2920	Air*	40.0	1.0	1000	1.45×10^{-9}	1.69×10^{-2}	[8]
0.4 wt.% Sodium dodecyl sulfate (SDS)	19.9	Air*	40.8	0.9	1000	1.45×10^{-9}	1.69×10^{-2}	This study

*Properties of N_2 assumed in analysis

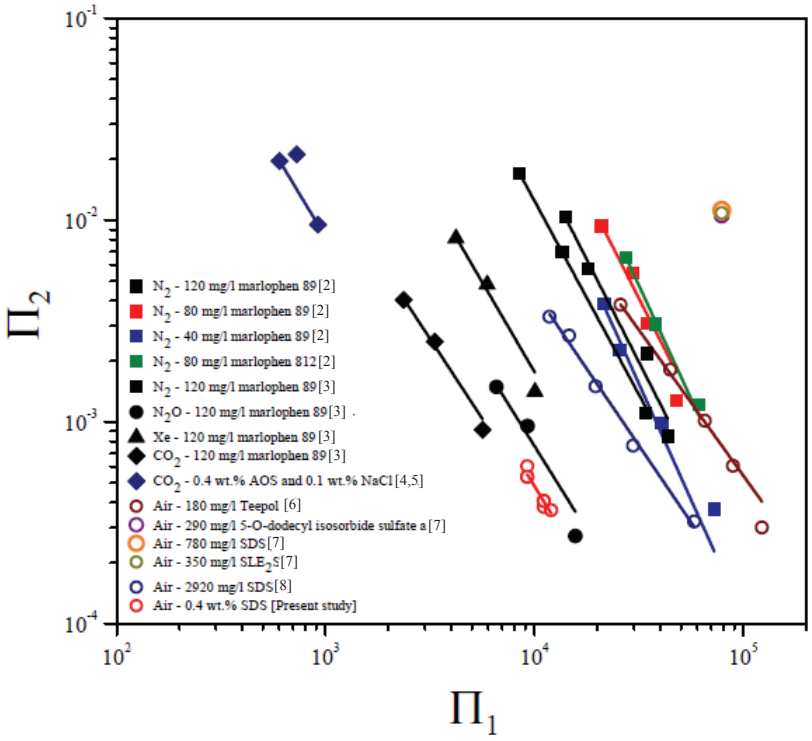

Figure 2.4: Relationship between Π_2 vs. Π_1 for aqueous foams made from different surfactant solutions and gases measured in the present study and reported in the literature [2–8]. Experimental conditions and fluid properties are summarized in Table 2.1.

Moreover, Figure 2.5 plots $\Pi_1^{1.8}\Pi_2$ versus Π_3 for the same data shown in Figure 2.4. Equation (2.15) appears to fit experimental data over a wide range of thermophysical properties with the parameters $L = 118$ and $m = -0.96$ with a coefficient of determination $R^2_{corr} = 0.95$. Figure 2.5 also shows the 95% confidence and prediction intervals for the derived power-law relationship. Note that the derived correlation spans four and five orders of magnitude in terms of $\Pi_1^{1.8}\Pi_2$ and Π_3, respectively. Furthermore, the average relative error between model predictions given by Equation (2.15) and the 95% confidence and prediction intervals was less than $\pm 4\%$ and $\pm 10\%$, respectively. Such spread is ex-

pected in two-phase flow, particularly for foams given (1) their inherent metastability, (2) the different interdependent physical phenomena (i.e., drainage, Ostwald ripening, and bubble coalescence) and (3) the resulting experimental uncertainty. Differences between experimental data and power law predictions can be attributed to two primary factors: (i) the limited amount of data available for steady-state thicknesses of foams generated with low viscosity solutions and (ii) the uncertainties of the actual measured physical quantities (i.e., r_0, H_∞, D) used to estimate the dimensionless number Π_1, Π_2, and Π_3.

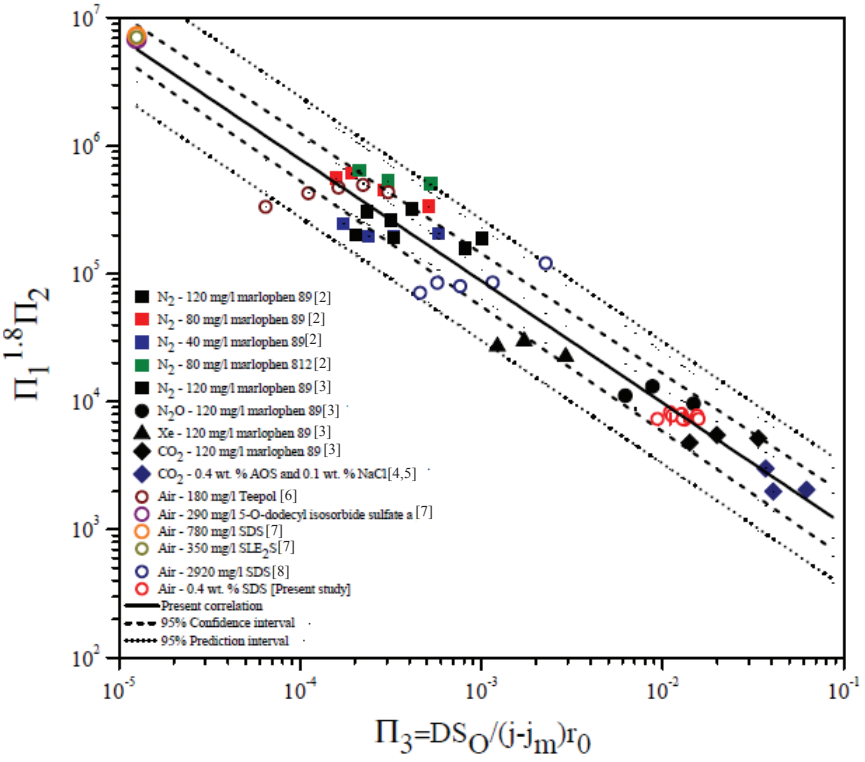

Figure 2.5: Correlation between dimensionless numbers $\Pi_2\Pi_1^{1.8}$ and Π_3 for aqueous foams made from different surfactant solutions and gases as summarized in Table 2.1. The same data sets were presented in Figure 2.4.

For instance, typical uncertainties include $\pm 5\%$ for the variation in measured foam thickness [2], and $\pm 10\%$ for the diffusion coefficient estimated by the model presented by Wilke

and Chang [69]. Additionally, measurements of bubble radius, particularly, in cases where the radius is visually determined, have been shown to be a significant source of experimental uncertainty [70]. Furthermore, due to increased interbubble gas diffusion in lower viscosity fluids, the use of the average radius r_0 in the dimensional analysis is clearly a first order approximation as bubbles change size as they rise through the foam. Lastly, as pointed out in previous studies [55], differences between correlation predictions and experimental data were larger in cases when the superficial gas velocity approached j_m corresponding to smaller foam thicknesses.

In order to identify the significant physical phenomena influencing the steady-state foam thickness, Equation (2.15) can be expressed in dimensional form as,

$$H_\infty = 118 \frac{\sigma}{r_0^{1.64}} \frac{\mu^{0.8}(j - j_m)^{1.76}}{(\rho g)^{1.8}(D S_O)^{0.96}}. \tag{2.16}$$

The effects of gravity, liquid viscosity, and density captured by Π_1 and Π_2 have been discussed previously and need not be reported [55]. Only the effects of parameters appearing in Π_3 should be discussed. Equation (2.16) indicates that the steady-state foam thickness decreases as either the Ostwald solubility coefficient S_O or the diffusion coefficient D increases. As previously discussed, coarsening destabilizes the foam and is enhanced by larger values of D and S_O. In addition, the steady-state foam thickness increases with increasing superficial gas velocity j. This is consistent with experimental observations [2, 3, 55]. Foam thickness has also been shown to be significantly dependent on bubble radius r_0 [2] as evidenced by the associated exponent of 1.7 in Equation (2.16). Moreover, Ogawa *et al.* [71] experimentally established that the bubble radius is linearly proportional to surface tension σ. Therefore, Equation (2.16) suggests that increasing σ causes the ratio $\sigma/r_0^{1.64}$, and therefore H_∞, to decrease.

2.5 Chapter summary

This chapter presented a dimensional analysis of the governing equation for the time rate of change of bubble radius in foams accounting for Ostwald ripening. It led to the defini-

tion of a dimensionless number accounting for the effects of both the diffusion and solubility of the gas from the bubbles to the liquid phase identified as $\Pi_3 = DS_O/(j - j_m)r_0$. It represents the ratio of the average contact time between bubbles to the characteristic time for gas permeation. This number was combined with the dimensionless numbers Π_1 and Π_2 identified by Pilon *et al.* [55] and accounting for viscous, surface tension, and gravitational forces. Note that the same dimensionless number was also obtained by applying the Buckingham-Pi theorem to the relevant variables associated with steady-state foam thickness. A new power-law relation between Π_1, Π_2, and Π_3 was determined as $\Pi_2 = 118\Pi_1^{-1.8}\Pi_3^{-0.96}$ based on experimental data reported in the literature [2–8]. These results can be used in a wide range of applications such as petrochemical, pharmaceutical, food, and water treatment processes.

NOMENCLATURE

A	Surface area of bubble in foam (m^2)
D	Diffusion coefficient (m^2/s)
$f_1(r,t)$	Bubble size distribution in the foam (m)
g	Specific gravity (m/s^2)
$H(t)$	Transient foam thickness (m)
H_∞	Steady-state foam thickness (m)
J	Effective gas permeability [Equation (2.11)]
j	Superficial gas velocity (m/s)
j_m	Superficial gas velocity for onset of foaming (m/s)
k	Effective gas permeability [Equation (2.9)]
k_{ml}	Monolayer gas permeability or bubble lamella permeability (m/s)
K, L, m, n	Semi-empirical constants
N	Number of moles of gas inside a bubble (mol)
p_g	Pressure in the gas bubble (Pa)
p_l	Pressure in the liquid phase (Pa)
R	Universal gas constant (=8.314 J/mol.K)
r	Bubble radius in the foam (m)
r_m	Mean bubble radius in the foam (m)
r_0	Average bubble radius at the bottom of the foam (m)
S_O	Ostwald solubility coefficient
T	Temperature (K)
t	Time (s)

Greek symbols

δ_f	Thickness of the fluid region bounded by Plateau borders (m)
μ	Dynamic viscosity of the liquid phase (Pa· s)
Π_i	Dimensionless similarity parameters, i=1, 2, 3

ρ	Density (kg/m^3)
σ	Surface tension (N/m)
τ_c, τ_d	characteristic times of contact and permeation between bubbles (s)

Superscript

$*$	Refers to dimensionless properties

CHAPTER 3

Effect of Radiation on the Stability and Temperature Profile of Aqueous Foams

The present chapter experimentally and theoretically investigates the stability and temperature profile within aqueous foams exposed to normally incident infrared radiation.

3.1 Introduction

3.1.1 Background

As discussed in Chapter 1, aqueous foams are an excellent fire protection material due to their thermal insulating properties [54]. In addition, when aqueous foam coat a flame, liquid drainage douses the fire; liquid drainage rates are faster in low viscosity foams because of reduced shearing between bubbles and the adjacent liquid. In these applications it is important to understand the various transport phenomena in foams and the effects of incident thermal radiation on foam stability and heat transfer.

3.1.2 Radiation transfer in liquid foams

Boyd and Di Marzo [54] studied the effect of thermal radiation incident on fire-protection foam. They assumed that all the incident radiation was entirely absorbed by the aqueous foam and treated it as a cold medium. They also assumed the foam was gray, i.e., its radiation characteristics were independent of wavelength. They solved the steady-state radiative transfer equation (RTE) for a gray, homogeneous absorbing, scattering, but

non-emitting medium governing the radiation intensity $I(\hat{r}, \hat{s})$ at spatial location $\hat{r}$ in the direction $\hat{s}$ and expressed as [72]

$$\hat{s} \cdot \nabla I(\hat{r}, \hat{s}) = -\beta I(\hat{r}, \hat{s}) + \frac{\sigma_s}{4\pi} \int_{4\pi} I(\hat{r}, \hat{s}) \Phi(\hat{r}, \hat{s}_i \rightarrow \hat{s}) \mathrm{d}\hat{s}_i. \tag{3.1}$$

Here, β denotes the effective extinction coefficient of the foam defined as the sum of its absorption coefficient κ and the scattering coefficient σ_s. The scattering phase function $\Phi(\hat{r}, \hat{s}_i \rightarrow \hat{s})$ is defined as the probability that radiation from direction $\hat{s}_i$ will be scattered in direction $\hat{s}$. Additionally, they demonstrated that heat transfer by convection in the bubbles and conduction across the foam were minimal compared with radiative heat transfer in standing foams exposed to thermal radiation [54]. However, heat transfer by evaporation contributed on a similar order to that of radiative heat transfer in the overall energy transfer [54]. The authors used Beer-Lambert's law to predict the radiation intensity as a function of depth in the foam column. However, Beer-Lambert's law is the solution of the RTE if single scattering prevails and if the foam boundaries are non-reflecting [72]. These conditions are not satisfied in moderately thick foams where multiple scattering is significant. Another approach, albeit more rigorous, involves solving the RTE using the Schuster-Schwartzchild two-flux approximation [72]. For example, Fedorov and Viskanta [73] used the two-flux approximation to solve the RTE to determine expressions for the internal reflectance, transmittance, and absorbance of a plane-parallel foam slab.

Let us consider a plane-parallel foam slab as shown schematically in Figure 3.1. Pottier *et al.* [74] provided an analytical solution for the spectral fluence rate G_λ in a one-dimensional absorbing and scattering medium of thickness H_∞ with a transparent face and a reflecting back of reflectivity ρ_λ based on the two-flux approximation for normally incident irradiance $G_{in,\lambda}$ given by

$$\frac{G_\lambda(z)}{G_{in,\lambda}} = 2\frac{[\rho_\lambda(1+\alpha_\lambda)e^{-\delta_\lambda H_\infty} - (1-\alpha_\lambda)e^{-\delta_\lambda H_\infty}]e^{\delta_\lambda z} + [(1+\alpha_\lambda)e^{\delta_\lambda H_\infty} - \rho_\lambda(1-\alpha_\lambda)e^{\delta_\lambda H_\infty}]e^{-\delta_\lambda z}}{(1+\alpha_\lambda)^2 e^{\delta_\lambda H_\infty} - (1-\alpha_\lambda)^2 e^{-\delta_\lambda H_\infty} - \rho_\lambda(1-\alpha_\lambda^2)e^{\delta_\lambda H_\infty} + \rho_\lambda(1-\alpha_\lambda^2)e^{-\delta_\lambda H_\infty}}. \tag{3.2}$$

Here, α_λ and δ_λ are expressed as [74]

$$\alpha_\lambda = \sqrt{\frac{\bar{C}_{abs,\lambda}}{\bar{C}_{abs,\lambda} + 2b_\lambda \bar{C}_{sca,\lambda}}} \qquad \text{and} \qquad \delta_\lambda = N_T \sqrt{\bar{C}_{abs,\lambda}(\bar{C}_{abs,\lambda} + 2b_\lambda \bar{C}_{sca,\lambda})} \tag{3.3}$$

where $\bar{C}_{abs,\lambda}$ and $\bar{C}_{sca,\lambda}$ are the average effective absorption and scattering cross-sections of bubbles in the foam, respectively. Here, N_T is the total number of bubbles per unit volume of foam and b_λ is the backward scattering fraction defined as

$$b_\lambda = \frac{1}{2} \int_{\pi/2}^{\pi} \Phi_\lambda(\theta) \sin\theta \mathrm{d}\theta. \tag{3.4}$$

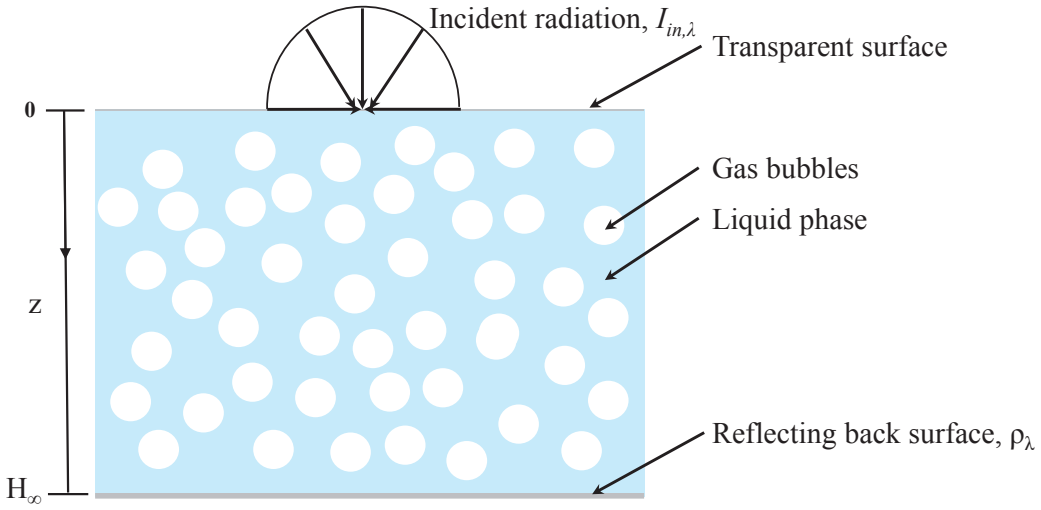

Figure 3.1: Schematic of the plane-parallel slab representative of radiation intensity incident on semi-transparent media containing bubbles.

3.2 Experiments

3.2.1 Experimental setup

Figure 3.2 depicts the experimental setup used in the present study. Aqueous foam was generated by injecting air into an aqueous surfactant solution contained in a vertical glass column (Wilmad-Lab Glass) of diameter 5.1 cm and height 30.0 cm.

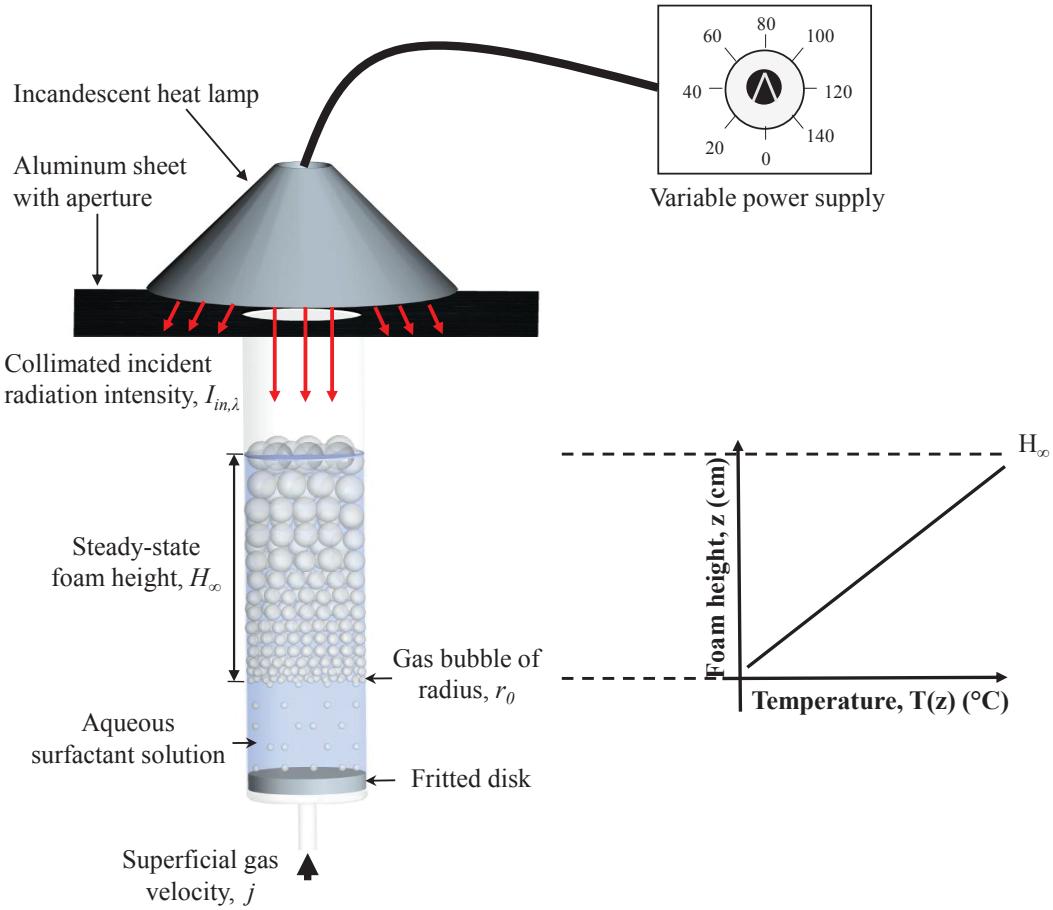

Figure 3.2: Schematic of the experimental apparatus used for determining thickness and temperature profiles of aqueous foams exposed to different incident irradiance.

The aqueous surfactant solution was made by mixing sodium dodecyl sulfate (SDS) surfactant of purity $\geq$99 % in deionized water with mass fraction equal to 0.4 wt.%. Sub-millimeter size bubbles were formed by constantly injecting air through a fritted disk with pore diameter ranging from 10-15 microns located at the bottom of the glass column. An incandescent heat lamp (Sylvania 175W/PAR38/HEAT120V) connected to a variable power supply was mounted and centered over the glass column. An aluminum sheet with a 6.0 cm diameter aperture was placed between the heat lamp and the glass column in order to collimate the incident radiation onto the foam surface.

3.2.2 Experimental procedure and data reduction

The applied power to the heat lamp generating the incident radiation was varied between 0 and 181 W. The air volumetric flow rate was measured using an Omega FT-042-15-G1-VN rotameter and was kept constant such that the superficial gas velocity remained equal to 0.015 mm/s. The foam steady-state height was visually measured using a laboratory grade scale mounted against the glass column. Photographs of the gas bubbles at the bottom of the foam were taken with a Nikon D90 DSLR camera equipped with a Nikon 55-200 mm VR lens. Image processing software ImageJ was used to determine the bubble size distribution at the bottom of the foam column. The temperature along the foam layer for different incident irradiances were measured by immersing a thin type-K thermocouple into the foam after it had reached a steady-state height. Note that the foam remained stable and its height did not change during the temperature profile measurements. The viscosity of the water in the foam at different temperatures was estimated from the DIPPR database. The viscosity of the liquid phase in the foam varied between 0.73 and 0.93 mPa/s as a function of the average temperature in the foam at different steady-state thicknesses. The surface tension of the aqueous SDS solution was reported by Zhao *et al.* [75] as 40.82 mN/m. Finally, measurement uncertainties for the gathered data were (i) $\pm$ 13 mm for foam height measurements, (ii) $\pm$ 2°C for foam temperature measurements, (iii) $\pm$ 0.6 W for power measurements, and (iv) $\pm$ 0.1 mm for the bubble radius.

3.3 Thermal analysis

3.3.1 Assumptions

In developing the governing equation for predicting the temperature profile along the steady-state foam column the following assumptions were made: (1) convective heat transfer was negligible, (2) there was no viscous dissipation within the foam, (3) steady-state conditions prevailed, (4) evaporative heat transfer was considered small compared to

radiative heat transfer, (5) the bubbles were assumed to be spherical, (6) thermophysical properties of the gas phase remained constant within the foam.

3.3.2 Governing equations

The two-flux approximation solution for the RTE given in the form of the analytical expression for the fluence rate [Equation (3.2)] can be further simplified by assuming that the bubbles in the aqueous foam layer scatter strongly in the forward direction. Then, b_λ approaches zero and therefore, α_λ approaches unity. Additionally, in the case of wet foams the refractive index mismatch at the aqueous liquid solution-foam interface at the bottom of the steady-state foam column is minimal and therefore, $\rho_\lambda \approx 0$. Then, Equation (3.2) reduces to

$$G_\lambda(z) = G_{in,\lambda} e^{-\delta_\lambda z} \qquad \text{with} \qquad \delta_\lambda = N_T \bar{C}_{abs,\lambda} = \kappa_\lambda. \tag{3.5}$$

3.3.3 Energy balance

Given the above assumptions, the one-dimensional steady-state energy conservation equation can be expressed as

$$\frac{\mathrm{d}}{\mathrm{d}z}\left(k_{eff}\frac{\mathrm{d}T}{\mathrm{d}z} - q_r\right) = 0. \tag{3.6}$$

Where k_{eff} is the foam effective thermal conductivity assumed to be independent of temperature and identical throughout the foam. The spatial derivative of the radiative heat flux term q_r is related to the local fluence rate according to [72]

$$\frac{\mathrm{d}q_r}{\mathrm{d}z} = \int_0^\infty \kappa_\lambda [4\pi I_{b,\lambda}(T) - G_\lambda(z)]\mathrm{d}.\lambda \tag{3.7}$$

Moreover, the foam was assumed to be a cold medium so that Equation (3.7) reduced to

$$\frac{\mathrm{d}q_r}{\mathrm{d}z} = -\int_0^\infty \kappa_\lambda G_\lambda(z)\mathrm{d}\lambda. \tag{3.8}$$

The total incident irradiance G_{in} on the steady-state foam was estimated by treating

the incandescent lamp as a blackbody source and given by

$$G_{in} = \pi \int_0^\infty I_{b,\lambda}(T_b) d\lambda = \sigma T_b^4. \tag{3.9}$$

The operating temperature of the lamp T_b was assumed to vary between 2800 and 3000 K for the power considered in this study [76].

Let $m_d = n_d - ik_d$ and $m_c = n_c - ik_c$ be the complex indices of refraction of the dispersed phase and of the continuous phase, respectively. Hale and Querry [77] reported the spectral complex indicex of refraction of water. The peak intensity of the incandescent heat lamp occured at wavelength of about 1 μm and thermal radiation emission from the lamp was concentrated in the near-infrared region [76]. Therefore, calculations were carried out in the wavelength region of 750 nm to 2 μm. This wavelength band captures over 90% of the spectral emission from the incandescent lamp used in the present experiment. Therefore, Equation (3.8) was approximated as

$$\frac{\mathrm{d}q_r}{\mathrm{d}z} = -\bar{\kappa} \int_{750}^{2000} G(z) \mathrm{d}\lambda \tag{3.10}$$

where $\bar{\kappa}$ is the average absorption coefficient within the spectral band ranging from 750 nm to 2 μm.

The combined Equations (3.5), (3.6), and Equation (3.10) were solved analytically subject to experimentally determined boundary conditions specifying the temperature at the air-foam and at the foam-liquid interfaces given by

$$T(z = 0) = T_0 \qquad \text{and} \qquad T(z = H_\infty) = T_f. \tag{3.11}$$

Then, the temperature profile across the foam column was expressed as

$$T(z) = \frac{G_{in}}{k_{eff}\bar{\kappa}} \left(1 - e^{-\bar{\kappa}z}\right) + \frac{z}{H_\infty} \left[T_f - T_0 + \frac{G_{in}}{k_{eff}\bar{\kappa}} \left(e^{-\bar{\kappa}H_\infty} - 1\right)\right] + T_0. \tag{3.12}$$

3.3.4 Constitutive relationships

First, the effective thermal conductivity of the foam k_{eff} was estimated using the series model [78] and expressed as

$$k_{eff} = (1 - f_v)k_c + f_v k_d \tag{3.13}$$

where the subscripts "d" and "c" refers to the dispersed (bubble) and the continuous (liquid) phase, respectively.

The total number of bubbles per unit volume of foam N_T at the bottom of the foam is given by

$$N_T = \frac{3f_v}{4\pi r_0^3} \tag{3.14}$$

where f_v is the foam porosity and r_0 is the average bubble radius. The radius r_0 was measured experimentally while the porosity, ϕ was taken as 0.70 for the aqueous foam generated in the present study [79].

The effective scattering and absorption coefficients of the foam were estimated based on the analysis by Fedorov and Viskanta [73]. Assuming all the bubbles have uniform radius r_0, the effective absorption and scattering coefficients of the foam were expressed as [73]

$$\kappa_\lambda = \kappa_\lambda^c - \pi \left[Q_{abs,\lambda}^c(r_0) - Q_{abs,\lambda}^d(r_0) \right] r_0^2 N_T \tag{3.15}$$

$$\sigma_{s,\lambda} = \pi Q_{sca,\lambda}^d(r_0) r_0^2 N_T \tag{3.16}$$

where $Q_{abs,\lambda}(r_0)$ and $Q_{sca,\lambda}(r_0)$ denote the absorption and scattering efficiency factors, respectively.

Moreover, the gas bubbles in the foam layer were considered weak absorbers and primarily act as strong radiation scatterers. Therefore, based on the anomalous diffraction approximation, the extinction efficiency factor for a weakly absorbing sphere was given as [73]

$$\begin{aligned} Q_{ext,\lambda}^j(\rho_j, m_j) = 2 - 4\frac{\cos(g_j)}{\rho_j} \times \left[e^{-\rho_j \tan(g_j)} \sin(\rho_j - g_j) \right] + \\ 4\left(\frac{\cos(g_j)}{\rho_j} \right)^2 \times \left[cos(2g_j) - e^{-\rho_j \tan(g_j)} \cos(\rho_j - 2g_j) \right] \end{aligned} \tag{3.17}$$

where $\rho_j = 2(n_j - 1)(2\pi r_0/\lambda)$ and $g_j = \arctan[k_j/(n_j - 1)]$ are the van de Hulst's normalized size and absorption parameters [80], respectively, such that $\rho_j \times \tan(g_j)$ gives the energy absorbed along the axial ray within the sphere. Here the subscript j refers to the dispersed or continuous phase optical properties denoted by subscripts d or c,

respectively. The absorption and scattering contributions to the extinction efficiency factor for a weakly absorbing sphere used in Equation (3.15) and (3.16) were expressed as

$$Q^j_{abs,\lambda}(\rho_j, m) = 1 + \frac{e^{-\rho_j \tan(g_j)}}{\rho_j \tan(g_j)} + \frac{e^{-\rho_j \tan(g_j)-1}}{2\left[\rho_j \tan(g_j)\right]^2} \tag{3.18}$$

and

$$Q^j_{sca,\lambda}(\rho_j, m) = Q^j_{ext,\lambda}(\rho_j, m) - Q^j_{abs,\lambda}(\rho_j, m). \tag{3.19}$$

Figure 3.3 plots the effective (a) absorption and (b) scattering coefficients predicted by Equations (3.15) and (3.16) of the aqueous foam as a function of wavelength spanning the near-infrared spectrum between 750 and 2000 nm, respectively. It is evident that the effective scattering coefficient of the foam is nearly independent of the wavelength for the ranges considered. Indeed, Vera *et al.* [81] analyzed the transport mean free path of photons in aqueous foam and determined that wavelength dependence of the scattering coefficient was minimal. Interestingly, the effective absorption coefficient of the aqueous foam was nearly constant across the near-infrared region except around 2000 nm, where it increased by one order of magnitude. This increase can be attributed to the fact that water strongly absorbs at wavelengths above 2000 nm [77]. The average effective scattering and absorption coefficients $\bar{\sigma_s}$ and $\bar{\kappa}$, respectively, are also shown in the figure.

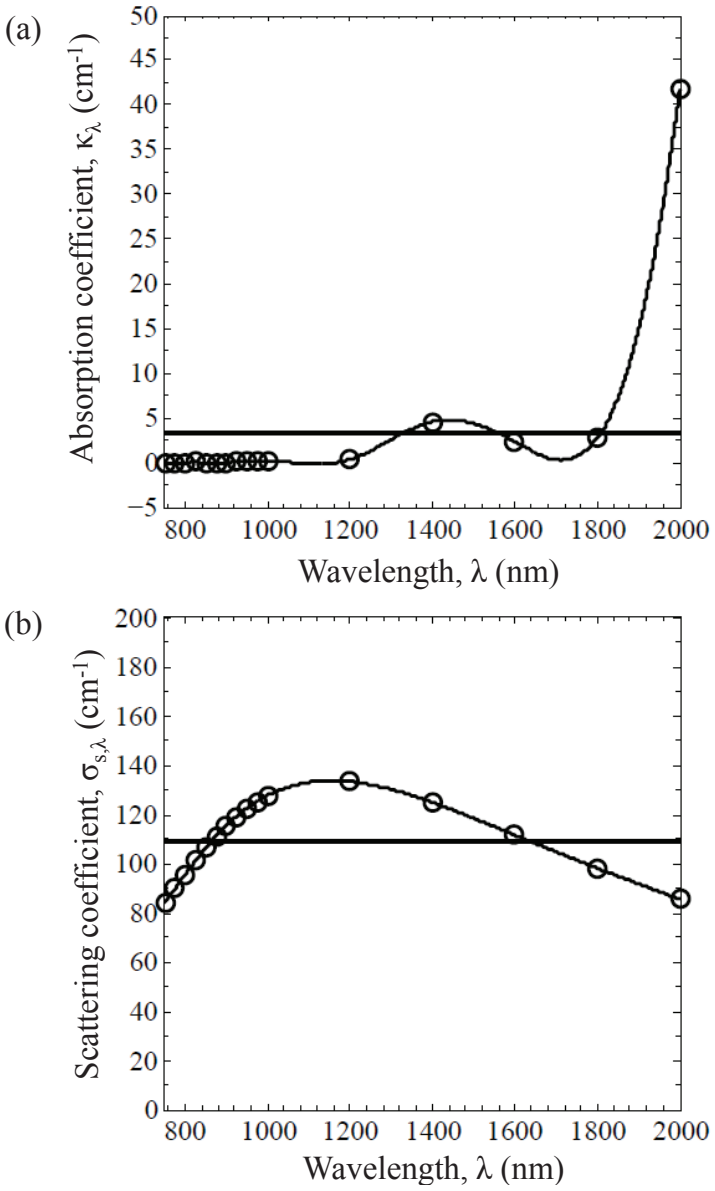

Figure 3.3: Effective spectral (a) absorption κ_λ and (b) scattering $\sigma_{s,\lambda}$ coefficients of aqueous foam with 70 % porosity calculated from Equations (3.15) and (3.16). Horizontal lines indicate the mean effective absorption $\bar{\kappa}$ (=3.3 cm^{-1}) and scattering $\bar{\sigma}_s$ (=110 cm^{-1}) coefficients.

3.4 Results and discussion

3.4.1 Foam morphology

Figures 3.4a and 3.4b show photographs of the foam generated experimentally under applied lamp power of 128 and 181 W, respectively. It indicates that the bubbles at the top of the foam layer are smaller under 128 W than under 181 W. This can be attributed to larger evaporation rates of liquid between adjacent bubbles associated with higher lamp power settings. Larger evaporation rates lead to increased bubble coalescence or the merging of bubbles to form larger bubbles.

Figure 3.5 plots the temporal evolution of the foam height under different incident irradiances. It indicates that the foam thickness increased nearly linearly before reaching a plateau corresponding to the steady-state thickness, H_∞. Figure 3.5 also shows a model for the transient foam thickness develop by Pilon *et al.* [1] and expressed as

$$H(t) = \frac{jt}{\phi} \tag{3.20}$$

Equation (3.20) agrees well with experimental data at and early stage the transient foam growth for all incident irradiances supplied by the incandescent lamp.

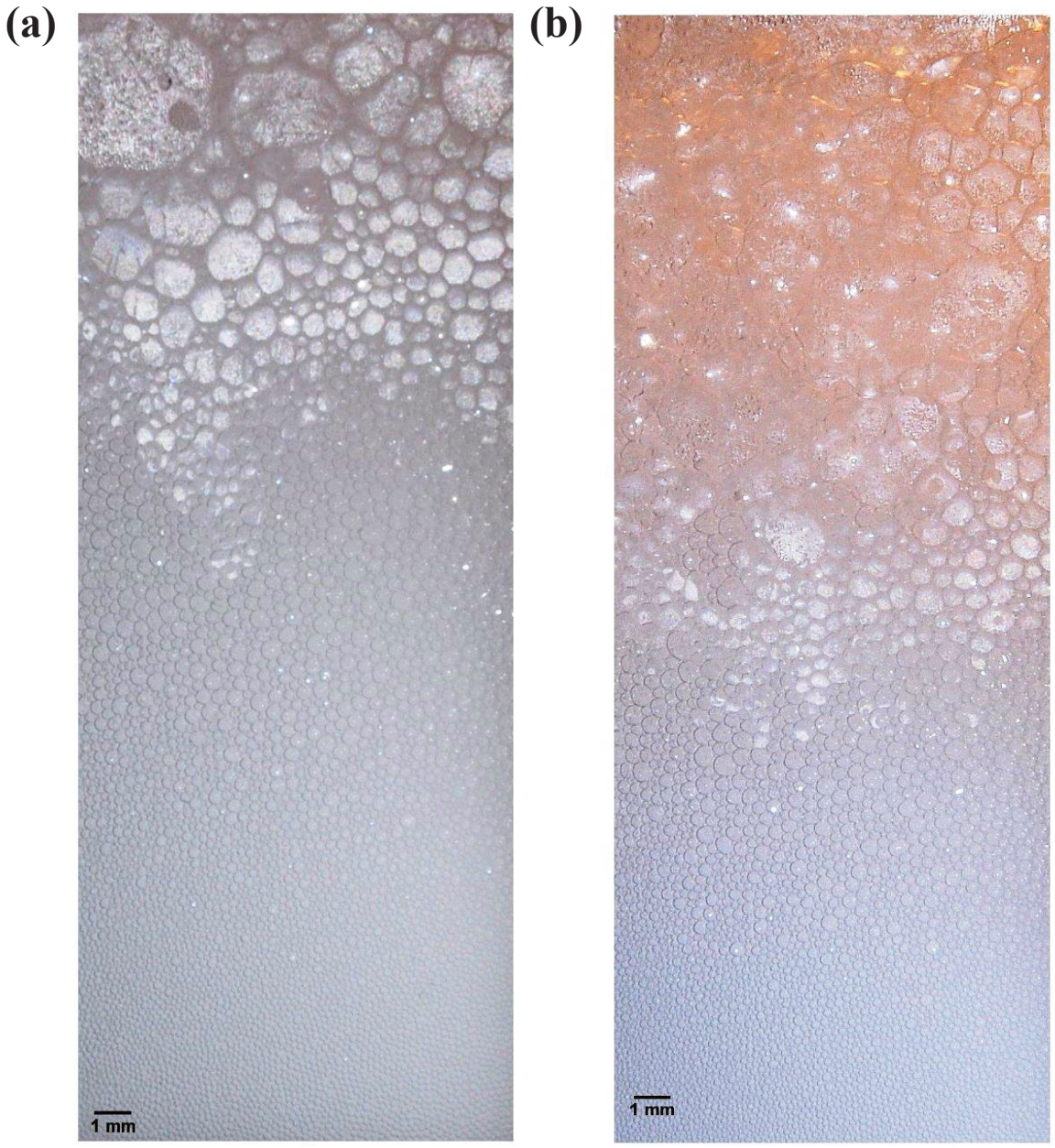

Figure 3.4: Pictures of steady-state aqueous foam generated during experimentation and exposed to irradiation from an incandescent lamp at (a) 128 W and (b) 181 W.

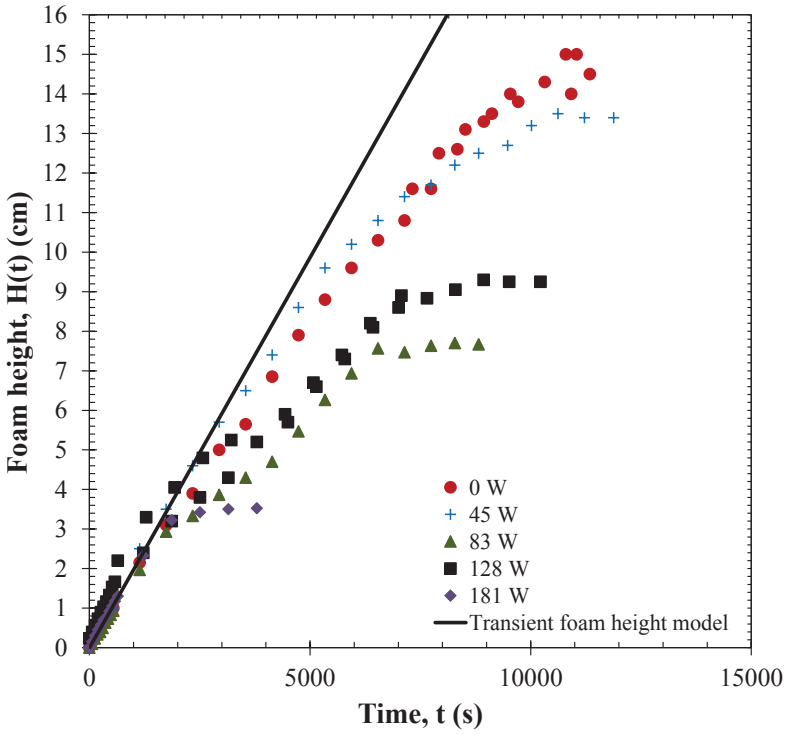

Figure 3.5: Temporal evolution of the height of aqueous foams generated by injecting air in a foaming solution at superficial gas velocity of 0.015 mm/s for different incident irradiances supplied by an incandescent heat lamp. The solid line represents the transient foam height model given by Equation (3.20) [1].

Figure 3.6 shows the average steady-state thickness of the foam as a function of the incident irradiance on the foam. It is evident that the steady-state foam thickness decreased as the incident irradiance increased. This can be attributed to the evaporation of fluid between adjacent foam bubbles that destabilizes the liquid film separating the bubbles at the surface. This results in bubble coalescence and/or bursting and ultimately in a thinner foam layer. In fact, the top surface of the steady-state foam featured a parabolic shape for low incident irradiance, whereas it was nearly flat for larger incident irradiance. The average bubble radius measured at the bottom of the steady-state foam column was found to be 0.125 mm for all incident irradiances.

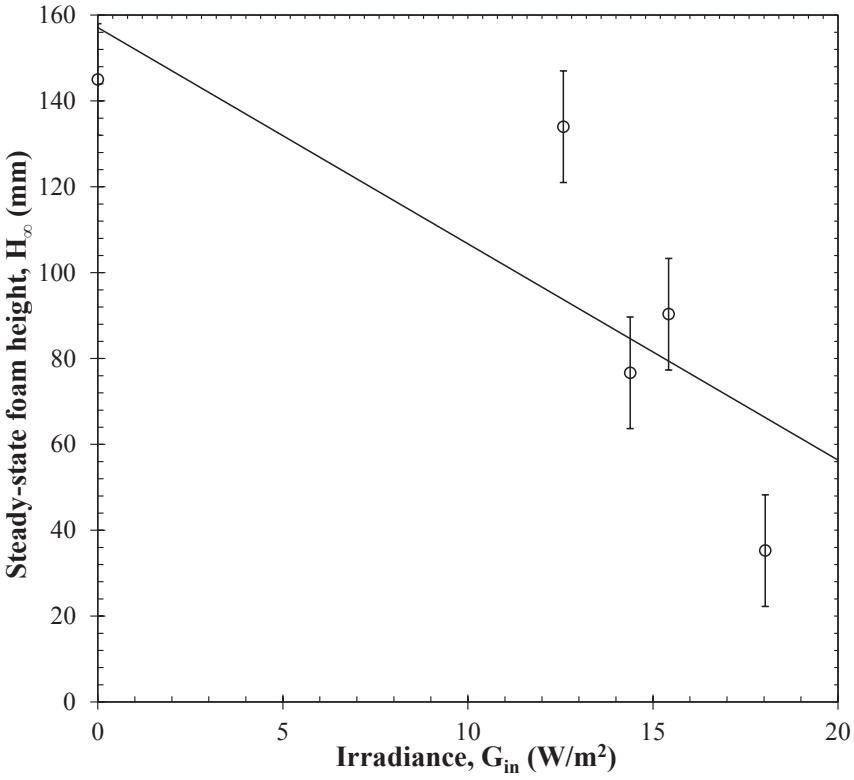

Figure 3.6: Steady-state height H_∞ of aqueous foams as a function of incident irradiance. Error bars correspond to uncertainty in steady-state height measurements, i.e. $\pm$ 13 mm.

3.4.2 Comparison with steady-state foam thickness model

Steady-state foam thickness measurements under both isothermal conditions and radiative heating were compared with the steady-state foam thickness predicted by Equation (2.16) discussed in Chapter 1. In the absence of radiative heating, Equation (2.16) predicted the foam thickness within 10 %. These results were very good given the experimental uncertainty associated with r_0 and H_∞. However, under radiative heating the differences between the predicted and experimental steady-state foam height were very large and increased with increasing incident irradiance. This is mainly attributed to the temperature dependence of thermophysical properties of the aqueous foam that was not

considered in the model given by Equation (2.16).

3.4.3 Temperature profile

The temperatures at different points along the steady-state foam layer were found to vary between 23 and 40°C depending on the incident irradiance.

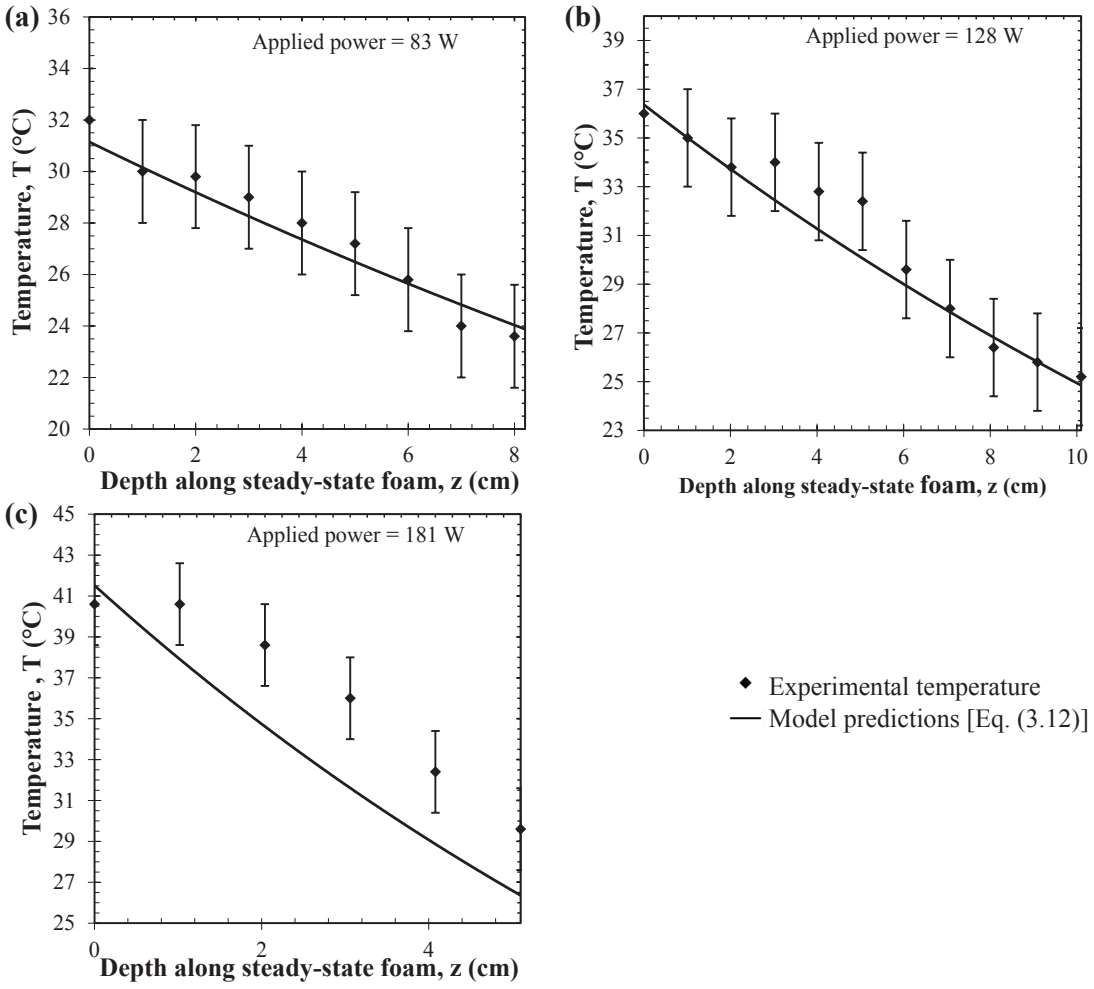

Figure 3.7: Experimentally measured temperature profile compared with predictions by Equation (3.12) for applied lamp power settings of (a) 83 W, (b) 128 W, and (c) 181 W. Error bars correspond to experimental uncertainty estimated to be i.e. $\pm$ 2.0°C.

Figure 3.7 shows the measured temperature profiles across the steady-state foam thickness for heat lamp power levels of (a) 83 W, (b) 128 W, and (c) 181 W, respectively. It is evident that the temperature decreased from the top (z =0) to the bottom ($z = H_\infty$) of the steady-state foam layer. Additionally, good agreement was observed between the experimental data and the model predictions of Equation (3.12). Here, deviations between the experimental data and the model predictions could be attributed to evaporative heat transfer that was not accounted for in the thermal model.

3.5 Chapter summary

The present chapter measured the evolution of aqueous foam exposed to normally incident thermal radiation. Aqueous foams were generated by injecting air bubbles into an aqueous surfactant solution made of 0.4 wt.% SDS. Steady-state foam thickness was found to decrease with increasing incident irradiance. Additionally, temperature profiles across the steady-state foam was measured for different incident irradiances. Experimental data agreed well with predictions from an analytical one-dimensional thermal model accounting for combined conduction and radiation through foam treated as a gray and cold medium. The radiation model was based on the two-flux approximation. Future studies should focus on incorporating the effects of temperature-dependent thermophysical properties and evaporation in both the physical model governing the steady-state foam thickness and in the thermal model for the temperature profile.

NOMENCLATURE

b_λ	Backward scattering fraction
$\bar{C}_{abs}$	Average bubble absorption cross-section (m^2)
$\bar{C}_{sca}$	Average bubble scattering cross-section (m^2)
f_v	Foam porosity
G_λ	Spectral fluence rate (W/m^2)
g	Specific gravity (m/s^2)
g_j	van de Hulst normalized absorption parameter
H_∞	Steady-state foam thickness (m)
I_λ	Spectral radiation intensity ($W/m^2 \cdot sr \cdot \mu m$)
j	Superficial gas velocity (m/s)
k	Absorption index
k_{eff}	Effective foam thermal conductivity [Equation (3.13)] (W/m/K)
m	Complex index of refraction, m = n - ik
n	Refraction index
N_T	Total number of bubbles per unit volume of foam ($1/m^3$)
Q	Efficiency factor
q_r	Radiative heat flux (W/m^2)
r_0	Average bubble radius (m)
$\hat{s}$	Direction vector (m)
T	Temperature (K)
t	Time (s)
z	Axial distance along foam column (m)

Greek symbols

α_λ	Parameter defined in Equation (3.3)
β_λ	Spectral extinction coefficient (1/cm)
δ_λ	Parameter defined in Equation (3.3)

θ	Angle between incident and scattered directions (rad)
$\bar{\kappa}$	Average absorption coefficient (1/m)
κ_λ	Spectral absorption coefficient (1/m)
ρ	Density (kg/m^3)
ρ_j	van de Hulst normalized size parameter (=2(n$_j$-1)/(2πr$_0$/λ))
ρ_λ	Reflectivity of aqueous surfactant solution
σ	Liquid/gas interface surface tension (N/m)
$\sigma_{s,\lambda}$	Spectral scattering coefficient (1/cm)
Φ	Scattering phase function
ϕ	Azimuth angle (rad)
$\hat{\Omega}$	Solid angle (sr)

Subscript

0	Refers to lower limit boundary condition
abs	Refers to absorption
in	Refers to incident radiation
sca	Refers to scattering
b	Refers to blackbody condition
f	Refers to upper limit boundary condition
λ	Refers to spectral properties

Superscript

c	Refers to continuous phase (liquid) in foam
d	Refers to dispersed phase (bubble) in foam

CHAPTER 4

Convective Heat Transfer in Foams Under Laminar Flow in Pipes and Tube Bundles

As previously discussed in Chapter 1, liquid foams represent a complex two-phase pseudoplastic fluid consisting of tightly packed bubbles of various diameter separated by a thin film of liquid. They have found applications in separation processes, oil recovery, water treatment, food processing, as well as in fire fighting and heat exchangers. In many of these applications, it is necessary to understand convective heat transfer in flowing liquid foams. This chapter reports experimental data and dimensional analysis for forced convection of foams and microfoams in laminar flow in circular and rectangular tubes as well as in tube bundles.

4.1 Background

4.1.1 Microfoam rheology

The rheological behavior of foams and microfoams can be described by the pseudoplastic power-law model expressed as [79],

$$\tau_w = K_P \dot{\gamma}_w^n = K'_P \dot{\gamma}_a^n = \mu_f \dot{\gamma}_a \tag{4.1}$$

where τ_w is the wall shear stress, $\dot{\gamma}_w$ is the true wall shear rate, and $\dot{\gamma}_a$ is the apparent shear rate while the effective foam viscosity is denoted by μ_f. The empirical constants K_P and n are the so-called flow consistency and flow behavior index, respectively. The true wall shear rate $\dot{\gamma}_w$ can be derived from $\dot{\gamma}_a$ through the Rabinowitsch-Mooney relationship [82],

$$\dot{\gamma_w} = \left(\frac{3n+1}{4n}\right)\dot{\gamma_a} \qquad \text{and} \qquad K'_P = K_P\left(\frac{3n+1}{4n}\right)^n. \tag{4.2}$$

Recently, Larmignat *et al.* [79] investigated the rheology of microfoams flowing through cylindrical pipes. Experimental data were collected for aqueous solutions of non-ionic surfactant polyoxyethylene (20) sorbitan monolaurate (Tween 20) with mass fraction ranging from 0.03 to 9.96 wt.%. The authors defined the volume equalized dimensionless shear stress and Capillary number as

$$\tau^* = \frac{\tau_w r_{32}}{\sigma\epsilon} \quad \text{and} \quad Ca^* = \frac{\mu_w r_{32}\dot{\gamma_a}}{\epsilon\sigma} \tag{4.3}$$

where r_{32} is the Sauter mean bubble radius, σ is the surface tension, μ_w is the viscosity of water, and ϵ is the specific expansion ratio defined as the ratio of the densities of the liquid phase and microfoam. Experimental data established that $\tau^* = C(\chi)(Ca^*)^{2/3}$ where $C(\chi)$ is an empirical function dependent on the surfactant mass fraction χ (in wt.%). In practice, microfoams made with aqueous solutions of Tween 20 can be treated as a shear-thinning fluid with an effective viscosity given by [79],

$$\mu_f = \mu_w C(\chi)(Ca^*)^{-1/3} \qquad \text{with} \qquad C(\chi) = 0.4 + 0.8(1 - e^{-\chi/0.018}) \tag{4.4}$$

These results were in good agreement with the model developed by Denkov *et al.* [83,84] for foams with porosity larger than 90% made of fluids with low surface dilatational modulus resulting typically in tangentially mobile bubble surface. They were also confirmed by experimental measurements for anionic and cationic surfactants including hexadecyltrimethyl-ammonium bromide (CTAB) and sodium lauryl sulfate (SDS) [68].

4.1.2 Convective heat transfer in power-law fluids in circular pipes

Bird [11] derived an analytical solution predicting the local Nusselt number in the entry region Nu_x^* and in the thermally fully developed region Nu_∞^* for single phase power-law fluids with flow behavior index n flowing through circular pipes subject to constant wall

heat flux as,

$$Nu_x^* = \frac{h_x D_h}{k} = 1.41\left(\frac{3n+1}{4n}\right)^{1/3}\left(\frac{2}{x^+}\right)^{1/3} \qquad \text{and} \qquad Nu_\infty^* = \frac{8(5n+1)(3n+1)}{31n^2+12n+1}. \tag{4.5}$$

Here, D_h is the hydraulic diameter of the wetted perimeter, k is the thermal conductivity of the power-law fluid, and h_x is the local heat transfer coefficient. The dimensionless axial length x^+ is defined as $x^+ = 2x/D_h Re_D Pr$ where x is the axial location measured from the heated pipe entrance. The Reynolds and Prandtl numbers respectively denoted by Re_D and Pr were defined as,

$$Re_D = \frac{4\rho\dot{Q}}{\pi D_h \mu} \qquad \text{and} \qquad Pr = \frac{c_p \mu}{k}. \tag{4.6}$$

where c_p is the specific heat of the power-law fluid, ρ is the fluid density, μ is the fluid effective dynamic viscosity, and $\dot{Q}$ is the volumetric flow rate.

Alternatively, Joshi and Bergles [12] applied a non-Newtonian correction factor developed by Mizushina *et al.* [85] to the correlation for Newtonian fluids proposed by Churchhill and Usagi [86]. For constant fluid thermal properties this model is expressed as [12],

$$Nu_x^* = 4.36\left(\frac{3n+1}{4n}\right)^{1/3}\left\{1+\left[0.376(x^+)^{-0.33}\right]^6\right\}^{1/6}. \tag{4.7}$$

The authors experimentally validated this model with a single-phase power-law fluid made from 0.9 and 1.0 wt.% aqueous solution of hydroxy ethyl methyl cellulose (HEMC) flowing through a circular pipe subject to constant wall heat flux. Note that thermally fully developed flow is reached when the dimensionless axial length x^+ is greater than 0.1 [87]. In addition, for flow behavior $n = 2/3$, such as that exhibited by microfoams [68,79,83,84], the local Nusselt number predicted by Equations (4.5) and (4.7) falls within 10% of each other in the entry region and within 4% in the fully developed region.

Furthermore, Tseng *et al.* [13] experimentally investigated both the rheology and convective heat transfer of microfoams made of Tween 20 in horizontal minichannels with a rectangular cross-section and heated from three walls. The authors found that

the local heat transfer coefficient and Nusselt number for microfoams under imposed heat flux and laminar flow conditions were independent of mass flow rate and heat flux. These results were similar to observations and theory for Newtonian fluids under the same conditions [88]. They also determined that the heat transfer coefficient for microfoams made of aqueous surfactant solutions was smaller than for single-phase water due to the microfoams' large porosity and low thermal conductivity.

More recently, Gylys *et al.* [14, 15] investigated convective heat transfer in dry aqueous foams with porosity of 99.6%, 99.7% and 99.8% and velocities between 0.14 m/s and 0.32 m/s. The authors reported the local heat transfer coefficient as a function of fluid velocity for upward and downward vertical aqueous foam flow across staggered and aligned tube bundles of diameter D =0.02 m at different tube locations. Foams were generated by injecting gas in an aqueous surfactant solution through a perforated plate with 1 mm holes. Unfortunately, (i) the type of surfactant used to make the foam, (ii) the surface tension of the air/solution system, and (iii) the average bubble radius were not reported. Therefore, it was impossible to estimate the foam's effective viscosity and capillary number. Gylys *et al.* [14, 15] derived an empirical correlation for predicting the local Nusselt number, based on the effective foam thermal conductivity given by the parallel model. The average Nusselt number was expressed as a function of the gas phase Reynolds number for foam flow across staggered tube bundles [15]. The average heat transfer coefficient was given as a function of foam porosity and velocity for foam flow across the aligned tube bundle [14]. Unfortunately, these correlations were derived from a limited data set with specific geometric features and therefore the validity of these correlations for other tube bundle dimensions and different foam properties is unknown.

4.1.3 Convective heat transfer in rectangular channels

Lee and Garimella [89] derived a generalized correlation for predicting the local Nusselt number $Nu_{x,4}$ for convective heat transfer of laminar Newtonian flow in rectangular

microchannels with constant wall heat flux from all four sides. It is expressed as [89]

$$Nu_{x,4} = \frac{h_x D_h}{k} = \frac{1}{C_1(x^+/2)^{C_2} + C_3} + C_4 \tag{4.8}$$

Here C_1, C_2, C_3, and C_4 were empirical constants depending on the aspect ratio α of the rectangular channel ($1 \leq \alpha \leq 10$) and given by Equation (12) in Ref. [89]. Secondly, the dimensionless axial length x^+ is defined as previously using Re_D based on the hydraulic diameter of the channel D_h.

For constant wall heat flux from three sides with one adiabatic side, Phillips [90] introduced a correction factor to express the Nusselt number as,

$$Nu_{x,3} = Nu_{x,4} \times \left(\frac{Nu_{\infty,3}}{Nu_{\infty,4}}\right) \tag{4.9}$$

Here, $Nu_{\infty,3}$ and $Nu_{\infty,4}$ are the fully developed Nusselt number for three and four sided uniform wall heat flux boundary conditions, respectively expressed as [91]

$$Nu_{\infty,3} = 8.235\left(1 - \frac{1.883}{\alpha} + \frac{3.767}{\alpha^2} - \frac{5.814}{\alpha^3} + \frac{5.361}{\alpha^4} - \frac{2.0}{\alpha^5}\right) \tag{4.10}$$

and

$$Nu_{\infty,4} = 8.235\left(1 - \frac{2.0421}{\alpha} + \frac{3.0853}{\alpha^2} - \frac{2.4765}{\alpha^3} + \frac{1.0578}{\alpha^4} - \frac{0.1861}{\alpha^5}\right) \tag{4.11}$$

4.1.4 Convective heat transfer in tube bundles

Khan *et al.* [92, 93] presented an analytical correlation for single phase convective heat transfer in laminar flows across aligned and staggered tube bundles under constant temperature and wall heat flux. The average Nusselt number over the entire tube bundle in the fully developed region was expressed as

$$\bar{Nu}_{D,th} = C_1 Re_{D,max}^{1/2} Pr^{1/3} \tag{4.12}$$

where C_1 is a constant depending on the tube arrangement while the Reynolds number $Re_{D,max}$ was defined based on the maximum fluid velocity U_{max} as [93]

$$Re_{D,max} = \frac{\rho U_{max} D}{\mu} \tag{4.13}$$

The maximum velocity in the minimum flow area is denoted by U_{max} and expressed as [93]

$$U_{max} = max\left(\frac{l_T}{l_T - 1}\dot{Q}_f/A, \frac{l_T}{l_D - 1}\dot{Q}_f/A\right) \tag{4.14}$$

where A is the cross-sectional area of the test section and $l_D = \sqrt{l_L^2 + (l_T/2)^2}$ while l_T and l_L are the dimensionless longitudinal and transverse pitches defined as [93]

$$l_L = s_L/D \quad \text{and} \quad l_T = s_T/D \tag{4.15}$$

Here, s_L and s_T are the interaxial distance between tubes of diameter D in the direction of the flow and normal to the flow, respectively.

Finally, the above correlations [Equations (4.5) and (4.7)] have been validated and used for single-phase power-law fluids. However, it is not clear whether they are valid for two-phase fluids such as foams and microfoams. To the best of our knowledge, no experimental data and analysis have been reported for forced convective heat transfer in microfoams flowing in cylindrical pipes.

4.2 Experiments

4.2.1 Experimental setup

In the present study, microfoams were generated by continuously stirring an aqueous surfactant solution with a Silverson L4RT mixer at 7,000 rpm in a baffled container as described in detail in Refs. [68,79]. The aqueous surfactant solutions were made by mixing Tween 20 purchased from USB Corp. (USA) in deionized water with mass fraction χ equal to 0.22, 0.55, 2.17, and 4.23 wt.%. The container was placed in a large tank of water acting as a thermal reservoir to maintain the microfoam at constant temperature. Type-T thermocouples were used to monitor the microfoam and water temperatures. The microfoam was continuously produced and pumped into the test section to ensure that it had the same inlet morphology, porosity, and temperature. The foam porosity, Sauter mean bubble radius, and surface tension of the solution/air system were reported

in Table 1 of Ref. [79].

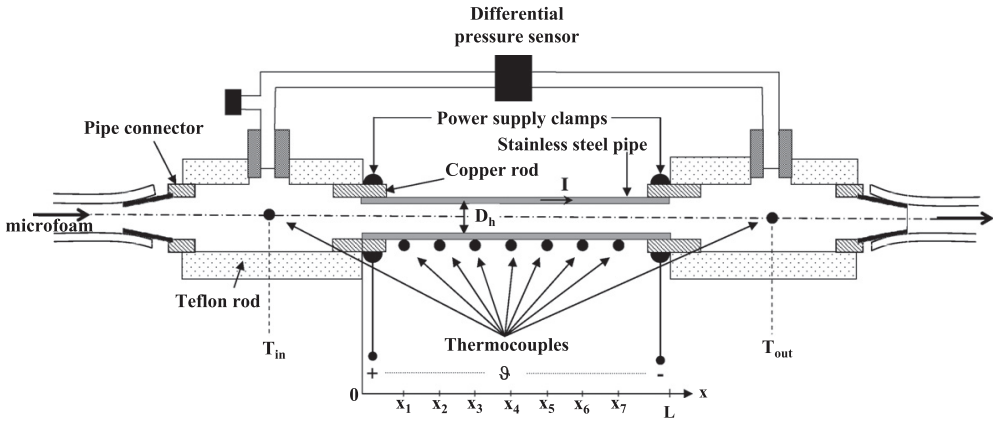

Figure 4.1: Schematic of the experimental test section used along with dimensions and locations of the thermocouples.

The experimental setup was typical of a pipe flow experiment and consisted of (i) a supply tank, (ii) a volumetric pump (Cole-Parmer, model 75225), (iii) a data acquisition system (IOTECH DAQTEMP 14 A) connected to a personal computer, and (iv) a test section shown in Figure 4.1. The test section consisted of a 0.305 m long stainless steel 304 cylindrical pipe tightly fitted through a copper rod. The pipes had inner diameter equal to 1.52 mm or 2.41 mm with corresponding outer diameter equal to 1.78 mm or 3.15 mm. Sealing was achieved by soldering the steel pipe and the copper rods. The latter was then screwed into Teflon rods used to connect the test section with the rest of the experimental setup. A differential pressure sensor (Omega PX26-015DV) was used to measure the pressure drop between the inlet and outlet of the pipe (Figure 4.1). The pressure drop was corrected for minor losses due to sudden expansion and contraction in the test section (Figure 4.1). Microfoam rheology was discussed in details in Ref. [79] and need not be repeated. The test section was heated by connecting the leads of a Sorensen DCS8-125E power supply to the copper rods thereby flowing a constant current and thus creating a constant wall heat flux along the stainless steel pipe (Figure 4.1). The microfoam temperatures at the inlet and outlet of the test section were measured by type-

K thermocouples. Likewise, seven type-K thermocouples were mounted axially along the top of the stainless steel pipe's outer wall with high thermal conductivity cement. The seven thermocouple axial locations x_i measured from the channel entrance were x_1=0.027 m, x_2=0.056 m, x_3=0.078 m, x_4=0.118 m, x_5=0.157 m, x_6=0.197 m, and x_7=0.260 m as illustrated in Figure 4.1. The test section was supported by G10 slabs placed above and underneath the pipe to ensure that it remained straight and horizontal. The heated pipe was also thermally insulated from the surroundings by several centimeters of fiberglass insulation to minimize heat losses.

Finally, the volume of microfoam $V_f(t)$ flowing out of the test section between times 0 and t was determined by using either a graduated Kimax 100 mL cylinder or a Nalgene 1 L beaker while the time t was measured by a stop watch. Simultaneously, the corresponding mass of microfoam $M_f(t)$ was measured by using a compact digital bench Ohaus Scout Pro SP401 scale. The plots of $V_f(t)$ and $M_f(t)$ as functions of time were linear and their slopes were the volumetric flow rate $\dot{Q}_f$ and the mass flow rate $\dot{m}_f$ of microfoam, respectively. The microfoam density ρ_f was experimentally determined by dividing the mass flow rate $\dot{m}_f$ by the volumetric flow rate $\dot{Q}_f$, i.e., $\rho_f = \dot{m}_f/\dot{Q}_f$. The microfoam porosity, defined as the ratio of the volume of gas to the total volume of foam, was estimated by [13]

$$\phi = 1 - \frac{\dot{m}_f}{\rho_w \dot{Q}_f} = 1 - \frac{\rho_f}{\rho_w} \tag{4.16}$$

where ρ_w is the density of water.

4.2.2 Experimental procedure and data reduction

The parameters measured experimentally for different values of flow rate and heat input were (i) the pressure drop along the cylinder, (ii) the inlet and outlet temperatures T_{in} and T_{out}, (iii) the local temperatures along the outer pipe wall $T_{wall}(x_i)$, (iv) the volumetric flow rate $\dot{Q}_f$, (v) the mass flow rate $\dot{m}_f$, and (vi) the microfoam density ρ_f and porosity ϕ.

Prior to collecting the data, the microfoam was flowed through the heated pipe for 5-10 minutes to ensure that a steady state had been reached. Then, the temperature readings were recorded for 1 minute and averaged. In addition, micrographs of the microfoam were taken at the inlet and outlet of the test section to verify that the microfoam morphology did not change significantly as it was flowed and heated in the pipe. Note that the residence time of the microfoams in the heated pipe was less than 3 seconds for the volumetric flow rates considered. Given the short residence time in the connecting pipes and in the test section, flow stratification caused by liquid drainage between the microfoam generation point and exit of the test section was assumed to be negligible.

The total power input was determined as the product of the current I and voltage ϑ applied across the test section,

$$q_{total} = \vartheta I. \tag{4.17}$$

The actual heat input from the wall to the microfoam q_f was determined from an energy balance on the microfoam given by,

$$q_f = \dot{m}_f c_{p,f}(T_{out} - T_{in}) \tag{4.18}$$

where $c_{p,f}$ is the specific heat of microfoam at the average temperature expressed as [13]

$$\rho_f c_{p,f} = \rho_w(1-\phi)c_{p,w} + \rho_g \phi c_{p,g}. \tag{4.19}$$

Here, ρ_g and $c_{p,g}$ are the density and specific heat of air, respectively, while ρ_w and $c_{p,w}$ are those of water.

The heat losses to the surroundings were quantified by subtracting the total heat input from the actual input into the microfoam, i.e., $q_{loss} = q_{total} - q_f$. In the present study, approximately 90% of the total electric power consumed was transferred to the microfoam flowing in the test section, i.e., heat losses from the test section to the surroundings were about 10%.

Finally, the wall heat flux $q_w^{''}$ was calculated from the heat input q_f to the microfoam according to,

$$q_w^{''} = q_f/\pi D_h L \tag{4.20}$$

where L is the length of the heated test section.

Furthermore, the cylinder inner wall temperature $T_i(x_i)$ at specified axial locations $(x_i)_{1\leq i\leq 7}$ were determined from temperature measurements at the outer wall $T_{wall}(x_i)$ by correcting for radial heat conduction through the pipe according to [13]

$$T_i(x_i) = T_{wall}(x_i) + ln(r_o/r_i)q_w^{''}r_i/k_{pipe} \tag{4.21}$$

where k_{pipe} (=14.9 W/m.K [88]) is the thermal conductivity of the stainless steel pipe used in the experiment and r_i and r_o are its inner and outer radii, respectively. The local temperature of the microfoam, $T_f(x)$ at different axial locations was estimated based on an energy balance given by [88],

$$T_f(x_i) = T_{in} + \left(\frac{T_{out} - T_{in}}{L}\right) x_i. \tag{4.22}$$

Then, the local heat transfer coefficient at location x_i was expressed as [13]

$$h_x(x_i) = \frac{q_w^{''}}{T_f(x_i) - T_i(x_i)}. \tag{4.23}$$

Finally, measurement uncertainties associated with the data were (i) ± 5 mL for volume V_f, (ii) ± 1.0 g for mass M_f, (iii) ± 5% for the volumetric flow rate $\dot{Q}_f$, (iv) ± 0.01 V for the voltage ϑ, (v) ± 0.01 A for the current I, and (vi) ± 0.2 °C for the temperature measurements T_{in}, T_{out}, and $T_{wall}(x_i)$. All properties were evaluated at the arithmetic mean of the inlet and outlet temperatures.

4.3 Results and discussion

4.3.1 Validation

The experimental procedure and data reduction were validated with single-phase deionized water flowing in 2.4 mm diameter pipe under laminar flow conditions with constant wall heat flux. Analytical expressions for the local Nusselt number Nu_x as a function of dimensionless axial length of the pipe $x^+ = 2x/D_hRe_DPr$ for these conditions were reported in Equation (8-42) in Ref. [9] and Equation (6.137) in Ref. [10].

Figure 4.2 compares Nu_x versus x^+ predicted by these expressions with our experimental data obtained with deionized water for wall heat transfer rate ranging from 74 to 125 W and Reynolds number between 727 and 1362. The dimensionless numbers were estimated using fluid properties [94] determined at $(T_{in} + T_{out})/2$. It is evident that the local Nusselt number decreased in the entry region as the thermal boundary layer develops. It reached a constant value independent of heat flux and Reynolds number in the thermally fully developed region where $Nu_x = 4.36$ [88]. These results establishes the validity of the experimental setup and data analysis.

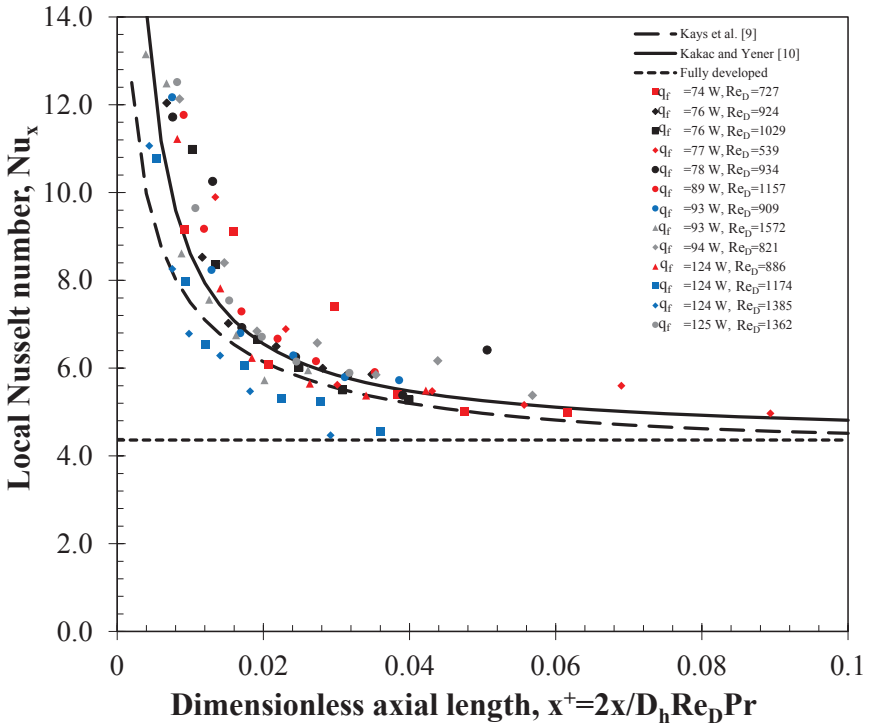

Figure 4.2: Comparison of the local Nusselt number as a function of dimensionless axial length of the pipe $x^+ = 2x/D_h Re_D Pr$ between experimental measurements and predictions from correlations given by Equation (8-42) in Ref. [9] and Equation (6.137) in Ref. [10] for laminar flow of single-phase deionized water under constant heat flux in 2.4 mm diameter pipe.

4.3.2 Dimensional analysis for convective heat transfer in foams

The dimensionless numbers Re_D, Nu_x, and Pr used in correlations for single-phase power-law fluids were given by Equations (4.5) and (4.6). However, for microfoams it remains unclear what expressions and fluid properties ρ, μ, c_p, and k should be used. One could treat microfoams as a homogeneous fluid with some effective properties estimated using an effective medium approximation (EMA). For example, a wide variety of EMAs exist for estimating the effective thermal conductivity k_f of heterogeneous materials including the series and parallel models [78] as well as Russel [95], son Frey [96], Rayleigh [97], De Vries [98], Maxwell [99], Bruggeman [100], and the dispersion thermal conductivity [101] models. However, no specific model has been validated for the thermal conductivity of microfoams. Note that experimental measurements are made difficult by the foam metastability and relatively rapid decay.

Alternatively, Lévêque's approximation [102], commonly applied to power-law fluids, assumes that at the wall the temperature boundary layer is controlled by a thin layer of fluid. In the case of aqueous foams, the heated wall is in direct and continuous contact with a thin layer of water separating the bubbles from the wall [83, 84] and controlling the overall convective heat transfer from the wall to the foam. In addition, based on dimensional analysis of the boundary layer equations, the Nusselt number can be interpreted as a dimensionless temperature gradient at the fluid/wall interface [88]. Thus, it is reasonable to define the Nusselt and Prandtl numbers based on the thermal properties of water, namely $c_{p,w}$ and k_w, as opposed to the effective properties of foams. However, from a rheological point of view, microfoams and macrofoams were showed to flow like a single-phase power-law fluid with some effective viscosity and density [68, 79, 83]. Then, the Reynolds number can be defined based on the effective physical properties of the microfoam, namely ρ_f and μ_f. In summary, for forced convection in foams, we define the dimensionless numbers Nu_x^*, Re_D^* and Pr^*, respectively, as,

$$Re_D^* = \frac{4\rho_f \dot{Q}_f}{\pi D_h \mu_f}, \qquad Nu_x^* = \frac{h_x D_h}{k_w}, \qquad \text{and} \qquad Pr^* = \frac{c_{p,w}\mu_f}{k_w}. \tag{4.24}$$

4.3.3 Results

The experimental data collected covered a broad range of microfoam properties as well as hydrodynamic and thermal conditions. In fact, the surfactant mass fraction ranged from 0.22 to 4.23 wt.% resulting in microfoams density between 254 kg/m^3 and 422 kg/m^3 corresponding to a porosity ϕ between 0.58 and 0.74. The microfoam volumetric flow rate $\dot{Q}_f$ varied between 0.336 cm^3/s and 1.46 cm^3/s. As a consequence, the effective viscosity μ_f of the microfoam varied from 0.005 N·s/m^2 to 0.022 N·s/m^2. Finally, the wall heat flux q''_w was varied between 4,360 W/m^2 and 21,380 W/m^2. In all cases (i) the microfoam Reynolds number was less than 1000 so that the flow was laminar and (ii) the dimensionless axial length x^+ reached at least 0.1 to ensure that thermally fully developed conditions were reached by the end of the test section. The uncertainty in the temperature measurements contributed an average of ± 7% error to the experimentally determined Nusselt number.

First, Figure 4.3 shows the measured heat transfer coefficient h_x estimated using Equation (4.23) versus the axial location x for microfoams made of surfactant solution with concentration 2.17 % flowing in pipes with diameter 1.5 mm and 2.4 mm under various wall heat fluxes and mass flow rates. It indicates that the heat transfer coefficient decreased along the channel length and reached a plateau for large enough values of x.

Figure 4.4 shows the local Nusselt number Nu_x^* versus the dimensionless axial length $x^+ = 2x/D_h Re_D^* Pr^*$ obtained with microfoams for all Tween 20 mass fractions, heat fluxes, and flow rates considered. The dimensionless numbers Nu_x^*, Re_D^*, and Pr^* were defined according to Equation (4.24). Figure 4.4 indicates that Nu_x^* decreased in the entry region and reached a constant in the fully developed region. The spread in the experimental data can be attributed to differences in porosity, bubble size distribution, and viscosity caused by differences in surfactant concentrations and flow rates. Such a spread in experimental data is typical of two-phase flow heat transfer experiments as reviewed in Ref. [103] and references therein.

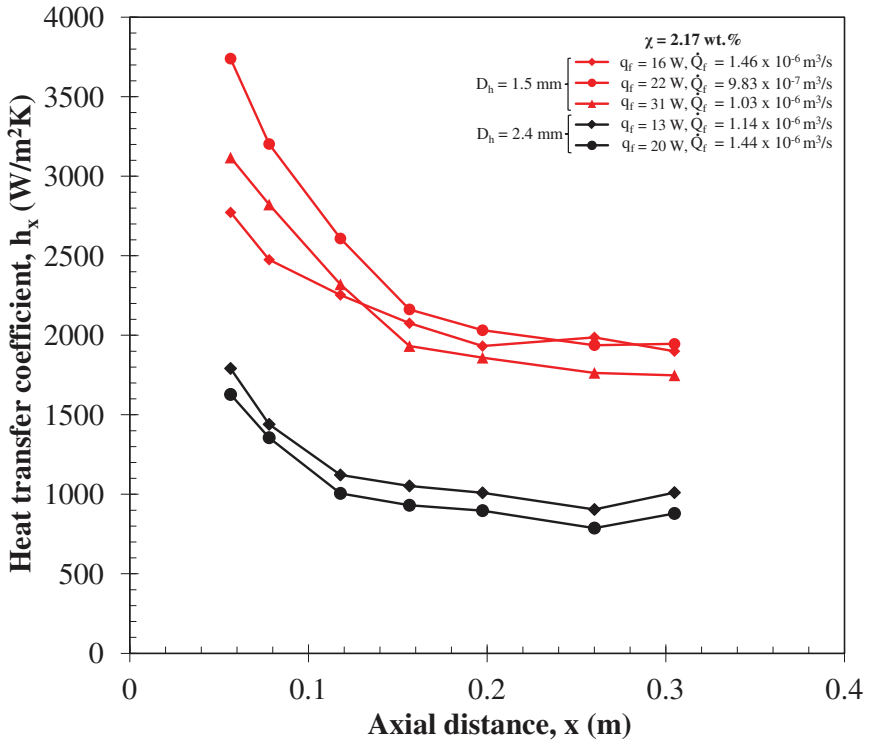

Figure 4.3: Local heat transfer coefficient calculated from Equation (4.23) versus axial length x for microfoam made from Tween 20 aqueous solution with concentration χ=2.17 wt.% flowing in 1.5 and 2.4 mm diameter tubes under different heat transfer rates q_f and mass flow rates $\dot{Q}_f$.

Overall, the data appeared to be consistent and overlap relatively well despite the large variation in microfoam morphology, rheological behavior, as well as imposed flow rates and heat fluxes. It is important to note that poor agreement was observed when defining Nu_x^* and Pr^* using the effective thermal properties c_p and k of the microfoam given by previously mentioned EMAs. This indicates that the expression of the dimensionless numbers Nu_x^*, Re_D^*, and Pr^* given by Equation (4.24) properly captured the phenomena taking place in convective heat transfer in microfoams flowing in uniformly heated pipes.

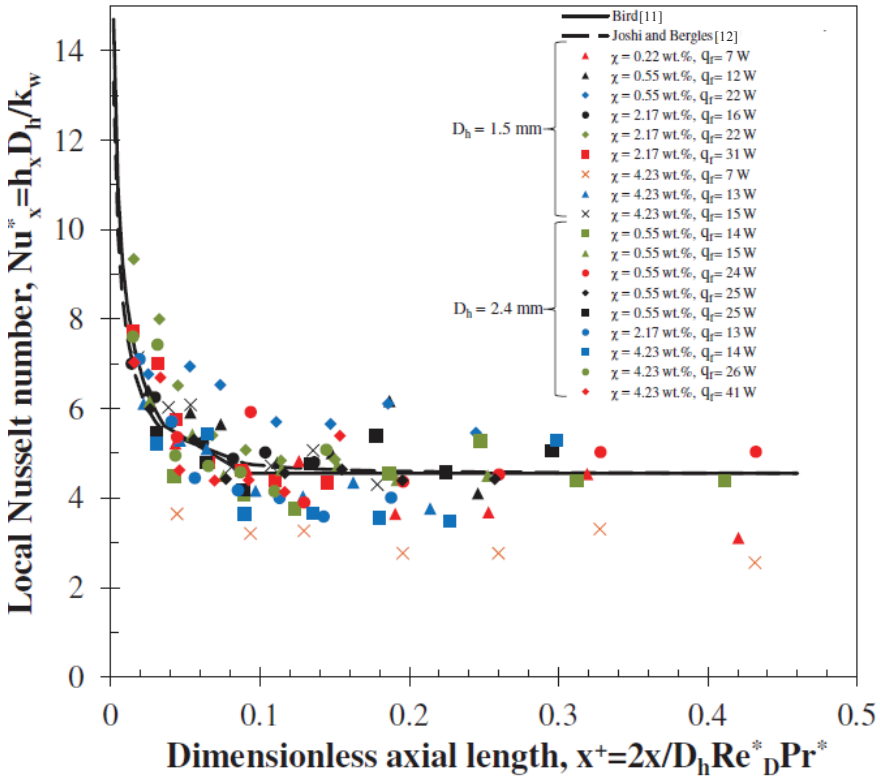

Figure 4.4: Comparison between experimental data and model predictions for the local Nusselt number $Nu_x^* = h_x D_h/k_w$ as a function of dimensionless axial length $x^+ = 2x/D_h Re_D^* Pr^*$ for microfoams with different surfactant mass fractions flowing in uniformly heated pipes. The dimensionless numbers were defined in Equation (4.24) while the models derived by Bird [11] and Joshi and Bergles [12] were given by Equations (4.5) and (4.7), respectively.

Moreover, Figure 4.4 also plots the analytical expressions of Nu_x^* for power-law fluids given by Equations (4.5) and (4.7) proposed by Bird [11] and Joshi and Bergles [12], respectively. Here, the index n was taken as 2/3. Given the experimental uncertainty, the experimental data for the Nusselt number are in good agreement with the model predictions for all microfoams and test conditions investigated. In fact, the average deviation between the fully developed Nusselt number $Nu_\infty^* = 4.55$ or 4.56 predicted by

Equations (4.5) and (4.7), respectively and the experimental values of Nu^*_∞ was less then 18%.

Finally, we speculate that the same results will be valid for microfoams made with other surfactants (e.g., CTAB, SDS) by analogy with previous isothermal rheological studies [68, 79]. However, it is unclear if the same approach would prevail for laminar forced convection under constant wall temperature, for turbulent convective heat transfer, and forced convection in different geometries such as rectangular channels and tube bundles. If so, existing correlations for single-phase pseudoplastic fluids could be easily extended to two-phase pseudoplastic fluids such as foams by defining the dimensionless numbers according to Equation (4.24) and using the non-Newtonian correction factor introduced by Mizushina *et al.* [85] and successful used by Joshi and Bergles [12] to account for the non-Newtonian behavior of microfoams. The next two sections aims to demonstrate the validity and generality of this approach.

4.3.4 Application to convective heat transfer to microfoams in rectangular minichannels

In order to apply the correlation giving $Nu^*_{x,3}$ for single-phase Newtonian fluid flowing in laminar flow in rectangular pipes heated from 3 walls to the data reported by Tseng *et al.* [13], Equations (4.9) and (4.10) were modified with the non-Newtonian correction factor $[(3n+1)/4n]^{1/3}$ so that

$$Nu^*_{x,3} = \frac{h_x D_h}{k} = Nu_{x,3} \left(\frac{Nu_{\infty,3}}{Nu_{\infty,4}} \right) \left(\frac{3n+1}{4n} \right)^{1/3} \tag{4.25}$$

and

$$Nu^*_{\infty,i} = Nu_{\infty,i} \left(\frac{3n+1}{4n} \right)^{1/3} \qquad \text{with i = 3 or 4} \tag{4.26}$$

where $Nu_{x,3}$ and $Nu_{\infty,3}$ are given by Equation (4.9) and (4.10) for Newtonian fluids while $Nu^*_{x,3}$ and $Nu^*_{\infty,3}$ are their counterparts for pseudoplastic fluids. Note that $Nu^*_{\infty,3}/Nu^*_{\infty,4}$ $= Nu_{\infty,3}/Nu_{\infty,4}$.

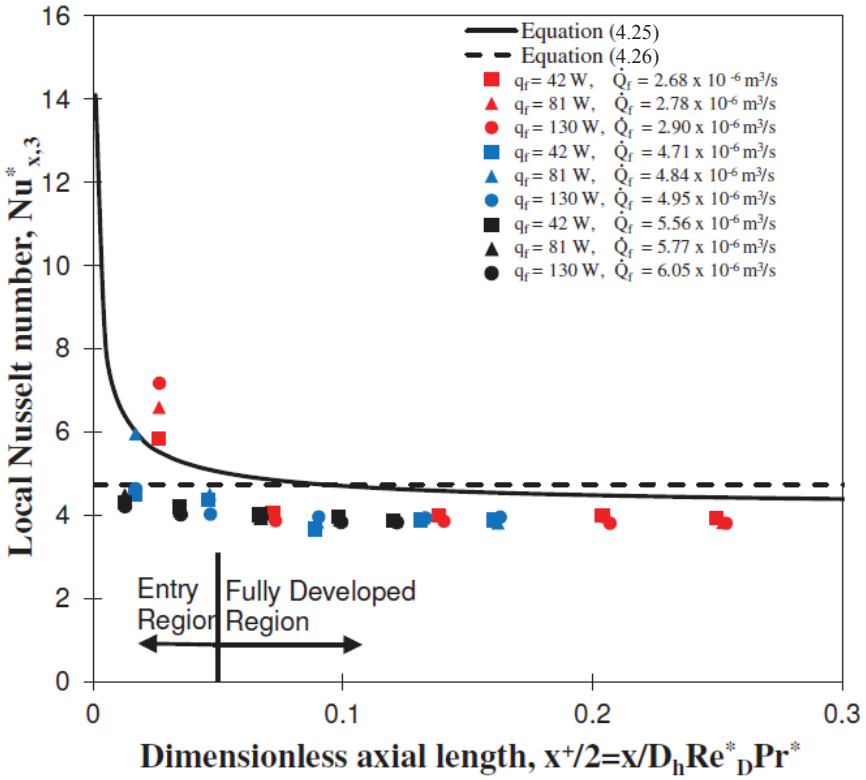

Figure 4.5: Comparison between experimental data and model predictions for the local Nusselt number $Nu^*_{x,3} = h_x D_h/k_w$ as a function of dimensionless axial length $x^+/2$ for aqueous microfoams made with Tween 20 and flowing through a rectangular mini-channel heat from three surfaces under different imposed heat fluxes and flow rates [13]. The dimensionless numbers were defined in Equation (4.24) while the models modified to account for non-Newtonian fluids were given by Equations (4.25) and (4.26).

Figure 4.5 shows the local Nusselt number $Nu^*_{x,3}$ versus the dimensionless axial length $x^+/2 = x/D_h Re^*_D Pr^*$ obtained with microfoams flowing in rectangular minichannels ($\alpha = 2.08$) heated from three sides under various heat fluxes and flow rates as reported by Tseng *et al.* [13]. Here also, the dimensionless numbers $Nu^*_{x,3}$, Re^*_D and Pr^* for microfoams were defined according to Equation (4.24). Figure 4.5 indicates that $Nu^*_{x,3}$ decreased in the entry region and rapidly reached a constant value in the fully developed

region. Furthermore, it is evident that the experimental data overlap quite well in the fully developed region thus further confirming that the expressions for the dimensionless numbers given by Equation (4.24) properly capture the phenomena occurring in convective heat transfer in microfoams under laminar flow conditions. Figure 4.5 also plots the modified correlations for convective heat transfer of pseudoplastic fluids under laminar flow in rectangular channels for both the local and fully developed Nusselt number given by Equations (4.25) and (4.26), respectively. Here also, the flow index n was taken as 2/3 [68,79,83,84]. Given the experimental uncertainty and the accuracy of the empirical correlations, the predictions of the modified correlations were in reasonable agreement with experimental data for the broad range of physical conditions considered.

4.3.5 Application to convective heat transfer to macrofoams in tube bundles

In this section, the data reported by Gylys *et al.* [14, 15, 104] and previously discussed were used. In their measurements, the cross-sectional area A was equal to 0.02 m^2 while $l_T = l_L = 1.5$ for the aligned tubes and $l_T = 3.5$ and $l_L = 0.875$ for the staggered tubes.

Figures 4.6(a) and 4.7(a) plots the average heat transfer coefficient versus U_{max} reported for foam flows across aligned and staggered arrangements, respectively [14,15,104]. They indicate that the heat transfer coefficient increases with increasing flow velocities. Note that the measured heat transfer coefficients were independent of tube location for tubes A4, B4, and C4 in aligned tube bundles and for tubes A3 and C3 in staggered tubes. Then, the flow was thermally fully developed.

Moreover, by analogy with the previous analysis for convective heat transfer in microfoams, the experimental average Nusselt number was defined based on the thermal conductivity of water in contact with the tubes as [93]

$$\bar{Nu}^*_{D,exp} = \frac{hD}{k_w}. \tag{4.27}$$

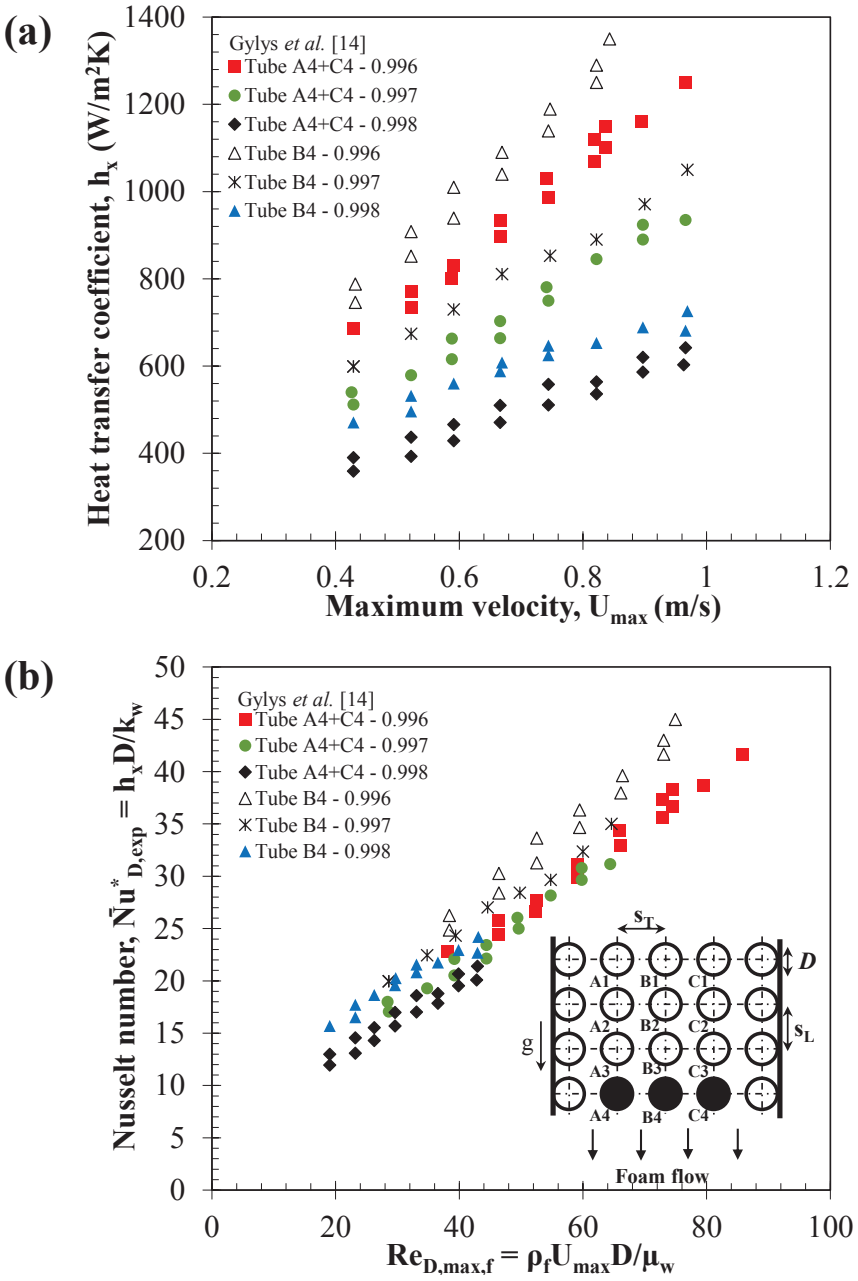

Figure 4.6: (a) Average heat transfer coefficient as a function of maximum velocity U_{max} measured by Gylys *et al.* [14] and (b) average experimental Nusselt number defined in Equation (4.27) versus $Re_{D,max,f} = \rho_f U_{max} D/\mu_w$ for downward flowing foams across tubes A4, B4, and C4 in aligned tube bundles.

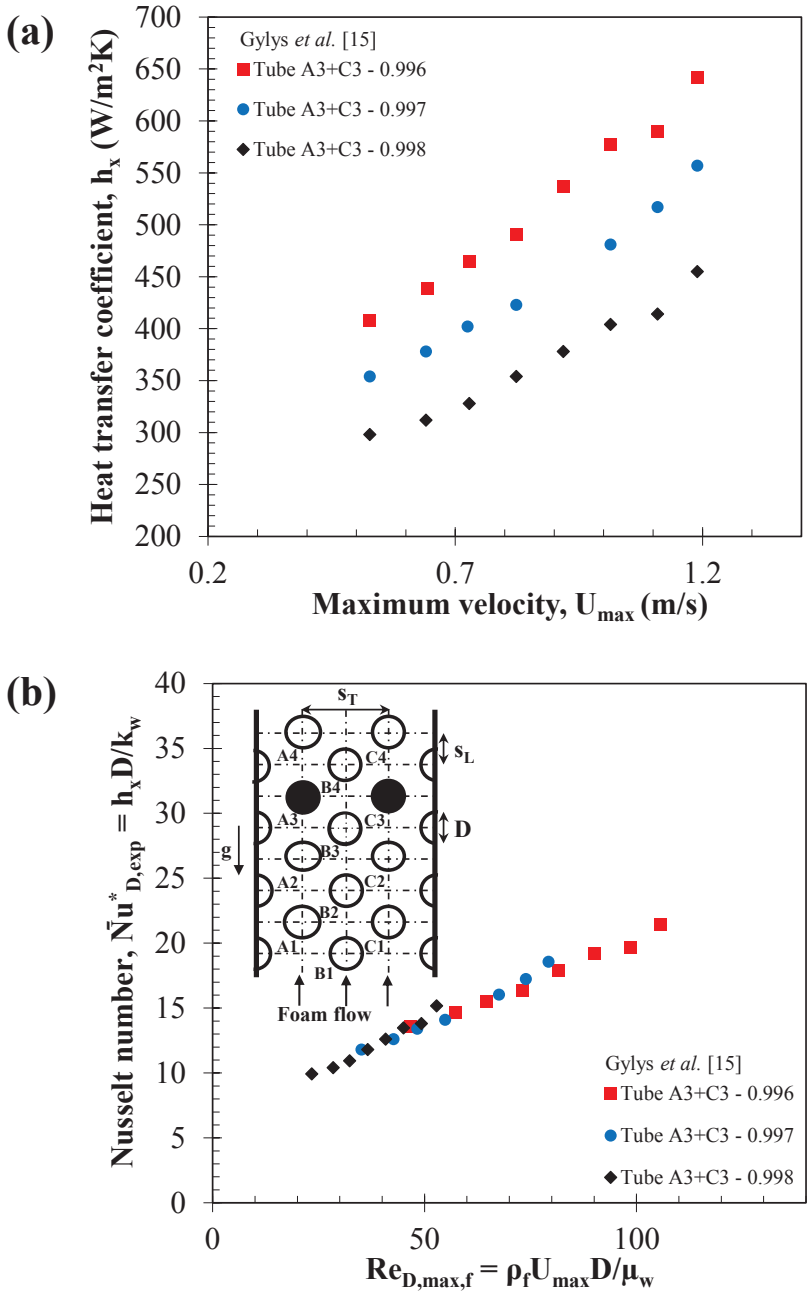

Figure 4.7: (a) Average heat transfer coefficient in the fully developed region as a function of maximum velocity U_{max} measured by Gylys *et al.* [15] and (b) average experimental Nusselt number defined in Equation (4.27) versus $Re_{D,max,f} = \rho_f U_{max} D/\mu_w$ for downward flowing foams across tubes A3 and C3 in staggered tube bundles.

Similarly, the Reynolds and Prandtl numbers for macrofoams in tube bundles were defined as

$$Re^*_{D,max,f} = \frac{\rho_f U_{max} D}{\mu_f} \qquad \text{and} \qquad Pr^* = \frac{c_{p,w}\mu_f}{k_w} \tag{4.28}$$

where ρ_f and μ_f are the foam density and viscosity while k_w and $c_{p,w}$ are the water thermal conductivity and specific heat, respectively. If the conclusions for microfoams can be applied to convective heat transfer macrofoams, the correlation developed by Khan *et al.* [93] for Newtonian fluids could be extended to macrofoams and expressed as

$$\bar{Nu}^*_{D,th} = C_1 C(\chi)^{-1/6} (Ca^*)^{1/18} \left(\frac{\rho_f U_{max} D}{\mu_w}\right)^{1/2} Pr_w^{1/3} \left(\frac{3n+1}{4n}\right)^{1/3} \tag{4.29}$$

where Pr_w is the Prandtl number of water while the term $[(3n+1)/4n]^{1/3}$ is the non-Newtonian correction factor introduced by Mizushina *et al.* [85]. The effective foam viscosity μ_f given by Equation (4.4) as well as $C(\chi)$ and Ca^* could not be estimated from the data provided by Gylys *et al.* [14, 15]. However, the term $C(\chi)^{-1/6}(Ca^*)^{1/18}$ appearing in the above equation is constant for a given surfactant mass fraction used to make the foaming solution.

Figures 4.6(b) and 4.7(b) plot the experimental average Nusselt number $\bar{Nu}^*_{D,exp}$ given by Equation (4.27) versus $\rho_f U_{max} D/\mu_w$ for the same locations in the aligned and staggered tube bundle arrangements as those shown in Figures 4.6(a) and 4.7(a). It is evident that the data collapse on a single line indicating the dimensionless numbers $\bar{Nu}^*_{D,exp}$ and $Re^*_{D,max,f}$ capture the physical phenomena occurring in the macrofoam flow across the tube bundles. The slight spread in the data can be attributed to variations in foam porosity, bubble size distribution, rheological behavior, as well as in imposed flow rates and temperature. Finally, in order to fully validate Equation (4.29), and in particular the non-Newtonian correction factor and the term $C(\chi)^{-1/6}(Ca^*)^{1/18}$, experiments with foams made from solutions with different surfactants and/or fluids other than water should be performed. Their bubble radius, surface tension, and effective viscosity should also be known or measured.

4.4 Chapter summary

The study outlined in this chapter collected and analyzed experimental data for convective heat transfer of microfoams in laminar flow condition in circular tubes under constant wall heat flux. Microfoams were made from aqueous solutions with Tween 20 surfactant concentrations with mass fraction ranging from 0.22 to 4.23 wt.%. A wide range of porosity, viscosity, flow rate, heat flux, and two different pipe diameters were explored. The results were compared with existing analytical and semi-empirical dimensionless correlations developed and validated with single-phase power-law fluids. Here, the Reynolds number Re_D^* was defined using the effective density and viscosity of microfoams. However, the dimensionless numbers Nu_x^* and Pr were defined based on the thermal properties of water. This can be justified by the fact that the heated pipe wall was in direct and continuous contact with a thin layer of water which controlled convective heat transfer to the foam. Good agreement was observed between the model predictions and experimental data when defining Nu_x^*, Re_D^* and Pr^* according to Equation (4.24). The same approach was successfully applied to experimental data collected for laminar flow of microfoams in rectangular minichannels heated from three walls and macrofoams across aligned and staggered tube bundles [14, 15]. Finally, it remains to be determined whether this simple and convenient approach can be extended to convective heat transfer in foams made of different fluids under different geometries and/or flow and boundary conditions.

NOMENCLATURE

A	Cross-sectional area of test section (m^2)
Ca^*	Volume equalized capillary number, Eq. (4.3)
$C(\chi)$	Empirical function, Eq. (4.4)
c_p	Specific heat (J/kg·K)
D_h	Hydraulic diameter (m)
h_x	Local heat transfer coefficient (W/m^2·K)
I	Current (A)
k	Thermal conductivity (W/m·K)
K_p	Flow consistency constant
L	Length of the test section (m)
l_L	Dimensionless longitudinal pitch, Eq.(4.15)
l_T	Dimensionless traverse pitch, Eq.(4.15)
$\dot{m}$	Mass flow rate (kg/s)
M_f	Mass of microfoam (Kg)
n	Flow behavior index
Nu_x	Local Nusselt number, $Nu_x = h_x D_h/k$
$Nu_{D,exp}$	Experimental local Nusselt number for tube bundles, Eq.(4.27)
Nu_∞	Nusselt number for thermally fully developed conditions
Pr	Prandtl number, $Pr = c_p\mu/k$
$\dot{Q}$	Volumetric flow rate (m^3/s)
q_f	Actual heat input to the microfoam (W)
q_{loss}	Heat loss to the surrounding (W)
q_{total}	Total power input (W)
$q_w^{''}$	Wall heat flux (W/m^2)
Re_D	Reynolds number, $Re = \rho\dot{Q}/\frac{1}{4}\pi D_h\mu$
$Re_{D,max}$	Reynolds number for flows across tube bundles, Eq. (4.13)

r_i	Inner pipe radius (m)
r_o	Outer pipe radius (m)
r_{32}	Sauter mean bubble radius (m)
$T_f(x_i)$	Average local temperature of microfoams (K)
T_{in}	Microfoam temperature at test section inlet (K)
T_{out}	Microfoam temperature at test section outlet (K)
$T_i(x_i)$	Inner wall temperature at location x_i (K)
$T_{wall}(x_i)$	Outer wall temperature at location x_i (K)
t	Time (s)
U_{max}	Maximum velocity in minimum flow area (m/s)
ϑ	Voltage (V)
V_f	Volume of microfoams (mL)
V_p	Volume of tube bundles (m^3)
x	Dimensional axial length (m)
x_i	Thermocouple location from pipe entrance (m)
x^+	Dimensionless axial length for cylindrical pipe, $x^+ = 2x/D_h Re_D Pr$

Greek symbols

α	Rectangular channel aspect ratio, (α =width/height)
χ	Surfactant mass fraction (wt.%)
ϵ	Specific expansion ratio
ϕ	Microfoam porosity
$\dot{\gamma}_a$	Apparent shear rate (1/s)
$\dot{\gamma}_w$	Wall shear rate (1/s)
μ	Dynamic fluid viscosity (Pa·s)
σ	Surface tension (N/m)
τ_w	Wall shear stress (Pa)
τ^*	Dimensionless shear stress

Subscript

f	refers to microfoam or foam property
g	refers to air in microfoam
$pipe$	refers to stainless steel pipe property
w	refers to water property or wall shear
$3, 4$	refers to rectangular channels heated from 3 or 4 walls

Superscript

$*$	refers to power-law fluid dimensionless numbers and correlations

CHAPTER 5

Absorption and Scattering by Liquid Marble Colloids

As discussed in Chapter 1, photoresponsive liquid marbles are a novel material that can be used as functional materials in sensing, delivery, and optofluidic applications [39,48–50]. In order to develop and optimize their use in these applications, it is necessary to understand their interaction with electromagnetic waves, and develop accurate and efficient means for predicting their radiation characteristics. As previously mentioned, the geometry and structure of a liquid marble consists of a spherical liquid core surrounded by a large number of small solid particles. A priori, the interaction of electromagnetic waves with liquid marbles depend on marble morphology, size, and on the materials used for the core and coating particles and their respective optical properties. This chapter reports predictions of the radiation characteristics of liquid marbles made of an aqueous core stabilized by a coating of highly hydrophobic and closely packed monodisperse non-absorbing or absorbing particles. It also discusses approximate methods based on simpler equivalent geometries for estimating the integral radiation properties of liquid marbles.

5.1 Background

5.1.1 Scattering matrix

The intensity and polarization of an electromagnetic wave are described by the Stokes vector, consisting of the four Stokes parameters I, Q, U, and V [105]. The Stokes vector of the radiation incident on a scatterer of arbitrary shape and orientation in direction $\hat{s}_i$ is given by $\mathbf{I}_{inc}(\mathbf{r}, \hat{s}_i) = (I_{inc}, Q_{inc}, U_{inc}, V_{inc})^T$. The incident Stokes vector is related

to the scattered Stokes vector $\mathbf{I}_{sca}(\mathbf{r},\hat{s}) = (I_{sca}, Q_{sca}, U_{sca}, V_{sca})^T$ via the Mueller matrix $[\mathbf{Z}(\Theta)]$ according to [106]

$$\mathbf{I}_{sca}(\mathbf{r},\hat{s}) = \frac{1}{r^2}[\mathbf{Z}(\Theta)]\mathbf{I}_{inc}(\mathbf{r},\hat{s}_i). \tag{5.1}$$

Here, r is the norm of the location vector $\mathbf{r}$ corresponding to the distance between the particle center and the observation point. The scattering angle Θ is defined as the angle between the incident $\hat{s}_i$ and scattered $\hat{s}$ directions. For randomly oriented aggregates of particles it is more convenient to use the normalized or Stokes scattering matrix $[\mathbf{F}(\Theta)]$ given by [105]

$$[\mathbf{F}(\Theta)] = \frac{4\pi}{C_{sca}}[\mathbf{Z}(\Theta)] \tag{5.2}$$

where C_{sca} is the scattering cross-section of the aggregate. It is defined as the energy of the incident electromagnetic (EM) wave falling on the area C_{sca}. Similarly, the absorption cross-section C_{abs} of the aggreage represents the energy of the incident EM wave falling on the area C_{abs}. Finally, the extinction cross-section is defined as $C_{ext} = C_{abs} + C_{sca}$. For a randomly oriented aggregate, the normalized scattering matrix is expressed as

$$[\mathbf{F}(\Theta)] = \begin{bmatrix} F_{11}(\Theta) & F_{12}(\Theta) & 0 & 0 \\ -F_{12}(\Theta) & F_{22}(\Theta) & 0 & 0 \\ 0 & 0 & F_{33}(\Theta) & F_{34}(\Theta) \\ 0 & 0 & -F_{34}(\Theta) & F_{44}(\Theta) \end{bmatrix}. \tag{5.3}$$

Here, $F_{11}(\Theta)$ represents the scattering phase function normalized according to [105]

$$\frac{1}{4\pi}\int_{4\pi} F_{11}(\Theta)d\Omega = 1 \tag{5.4}$$

where Ω is the solid angle around the scattering angle Θ. The asymmetry factor g is defined as

$$g = \frac{1}{4\pi}\int_{4\pi} F_{11}(\Theta)\cos\Theta \mathrm{d}\Omega. \tag{5.5}$$

It describes the shape of the scattering phase function. It is equal to 0, -1, and 1 for isotropic, purely backward, and purely forward scattering scatterers, respectively [53]. Moreover, the scattering matrix element F_{12}/F_{11} represents the degree of linearly

polarized scattered radiation for a particle exposed to unpolarized radiation [107]. In addition, the sphericity of the particle is identified by the ratio F_{22}/F_{11} [107]. The ratio F_{34}/F_{11} represents the fraction of obliquely polarized light at 45° that is transformed into circularly polarized radiation [107]. Finally, for spherical scatterers, $F_{22}(\Theta) = F_{11}(\Theta)$ and $F_{33}(\Theta) = F_{44}(\Theta)$, i.e., $F_{22}/F_{11} = F_{33}/F_{44} = 100\%$.

5.1.2 Superposition T-matrix method

The superposition T-matrix provides an accurate method for numerically determining the radiation characteristics of multisphere clusters including C_{abs}, C_{sca}, g, and the scattering matrix coefficients F_{ij} [108]. Given a cluster or aggregate of spheres, the superposition T-matrix estimates the scattered EM field of the aggregate as the sum of the EM fields scattered by each sphere. These interacting fields are transformed into a system of sphere-centered equations and inverted to obtain the T-matrix [109]. Then, the absorption Q_{abs} and scattering Q_{sca} efficiency factors, and the scattering matrix elements are obtained from simple operations on the T-matrix [109].

Mackowski [110] successfully utilized the superposition T-matrix method to predict absorption and scattering cross-sections of soot particles modeled as fractal aggregates of carbon spherical nanoparticles. This method has been used in a variety of other applications including (i) plasmon resonance in aggregates of gold [111] and silver [112] nanoparticles, (ii) interpretation of solar radiation scattered by cometary dust [113], (iii) and radiation characteristics of filamentous cyanobacteria [114, 115] and of bispheres, quadspheres, and rings of spheres [116]. More recently, Mishchenko *et al.* [117] used the superposition T-matrix to predict the absorption and scattering cross-sections, the asymmetry factor, the single-scattering albedo, and the scattering matrix elements of external, semi-external, and internal mixtures of micrometer-sized water droplets and containing soot particles. The authors demonstrated that the absorption cross-sections were highly dependent on the spatial arrangement of the soot particles. The absorption cross-section was larger when the soot particles were uniformly mixed within the water

droplet and smaller when the soot particles were aggregated. This was attributed to shading effects by the strongly absorbing soot particles.

5.1.2.1 Geometric-optics surface wave method

Alternatively, the geometric-optics surface-wave (GOS) method provides a means of predicting the absorption Q_{abs} and Q_{sca} efficiency factors, and the asymmetry factor g for spherical aggregates and spheres with spherical inclusions with overall size parameter χ larger than 2.0 [118–120]. First, the scattering and absorption efficiency factors are computed from the ray-by-ray integration algorithm developed for cases when geometric optics prevails, i.e., for $\chi >> 1$ [118, 121]. Then, following the work of Nussenzveig and Wiscombe [122], the extinction and absorption efficiency factors are computed for surface waves accounting for the interaction of waves at grazing angles near the periphery of a spherical particle. The extinction efficiency factors computed by the geometric optics method and for surface waves are added to predict the integral radiation characteristics of the aggregate [118].

5.1.3 Equivalent scatterers

A number of studies have focused on the development of approximate methods for predicting the radiative characteristics of aggregates of spherical particles by approximating these aggregates as equivalent scatterers with simpler geometries. For example, Latimer [123] approximated randomly oriented fractal aggregates of latex spherical particles of radius r_s in water as coated spheres in which the core and the coating had the complex index of refraction of the water and latex, respectively. Here, the inner $r_{L,i}$ and outer $r_{L,o}$ radii of the coated sphere were defined as [123]

$$r_{L,i} = N_{s,L}^{1/3} r_s \left(1 - \frac{1}{F^{1/3}}\right) \quad \text{and} \quad r_{L,o} = \left(\frac{r_s^3 N_{s,L}}{F}\right)^{1/3} \tag{5.6}$$

where $N_{s,L}$ refers to the number of particles in the aggregate. Here, F is the ratio of the total volume of particles and the volume of the smallest sphere enclosing the aggregate

expressed as a function of fractal dimension D_f as [123]

$$F = N_{s,L}^{\left(1-\frac{3}{D_f}\right)}. \tag{5.7}$$

Good agreement between the equivalent coated sphere predictions and experimental results of scattering intensities were observed for scattering angles between 0° and 15°. However relative errors reached up to 80% for scattering angles greater than 90° [123].

Taylan and Berberoğlu [42] approximated dry water particles as coated spheres for determining their radiation characteristics. For a given liquid marble particle with a water core of radius R_w stabilized by spherical silica particles of radius r_s, the dimensionally equivalent coated sphere had inner and outer radii given by

$$r_{R+2r,i} = R_w \quad \text{and} \quad r_{R+2r,o} = (R_w + 2r_s). \tag{5.8}$$

More recently, Heng *et al.* [116] demonstrated that the scattering and absorption cross-sections and asymmetry factor of randomly oriented and optically soft bispheres, quadspheres, and rings of spheres could be approximated by an equivalent coated sphere with identical volume and average projected area. Similarly, Kandilian *et al.* [124] showed that this coated sphere approximation was also valid for the absorption and scattering cross-sections and the asymmetry factor of randomly oriented fractal aggregates of spherical monomers.

Mishchenko *et al.* [117] approximated a spherical water droplet containing randomly distributed spherical carbon particles as a volume equivalent homogeneous sphere with effective refractive and absorption indices computed from the Maxwell Garnett Theory (MGT) for two-phase mixtures. The absorption and scattering cross-sections, the single-scattering albedo, and the asymmetry factor predictions by Lorenz-Mie theory for the volume equivalent homogenous sphere were in good agreement with the predictions by the superposition T-matrix method.

The present study aims to accurately predict the radiation characteristics of liquid marbles using the superposition T-matrix method. It also aims to assess whether liquid

marbles can be approximated by simpler geometries for the purpose of determining their radiation characteristics in an accurate and computationally inexpensive manner.

5.2 Analysis

5.2.1 Modeling liquid marbles

Liquid marbles made of aqueous cores and stabilized by either latex or TiO_2 monodisperse spheres of various sizes exposed to monochromatic EM waves with wavelength were investigated. Liquid marbles can be geometrically described as a spherical core of radius R_w coated by highly-ordered tangential monodispere spheres of radius r_s, as illustrated in Figure 5.1b [38, 43]. Figure 5.1c shows two adjacent and identical spheres of radius r_s tangential to the spherical core of radius R_w whose center coincides with the origin in the spherical coordinate system. The angle $\Delta\theta$ of the sector defined by the centers of two adjacent coating spheres and the center of the liquid marble core can be determined from the law of cosines as

$$\Delta\theta = \cos^{-1}\left(1 - \frac{2r_s^2}{R_t^2}\right). \tag{5.9}$$

Here, R_t is the sum of the core radius R_w and the coating radius r_s, i.e., $R_t = R_w + r_s$. Then, the number of spheres along a meridian between the North and South poles of the spherical core of radius R_w is given by $p = \pi/\Delta\theta$. Note, here the value of p was rounded down to the nearest integer to ensure that there is no sphere overlap or partial spheres. Moreover, there is a complete ring of spheres coating the core whose centers follow the same parallel increment $\Delta\theta$. For example, the center-to-center distance between an arbitrary sphere at index $i = 0$ and a sphere at the i^{th} level is given by

$$\mu_i = R_t \sin\theta_i \quad \text{with} \quad \theta_i = i\Delta\theta \quad \text{for} \quad i = 0, 1, 2, ...p.$$

Figure 5.1d shows a top view of a liquid marble indicating that the centers of the spheres form a polygon that is a function of the number of spheres at a given level i. Once again, the law of cosines can be employed to determine the minimum angle between

the centers of two adjacent spheres $\Delta\phi_i$ at the i^{th} level given as

$$\Delta\phi_i = \cos^{-1}\left(1 - \frac{2r_s}{\mu_i}\right). \tag{5.10}$$

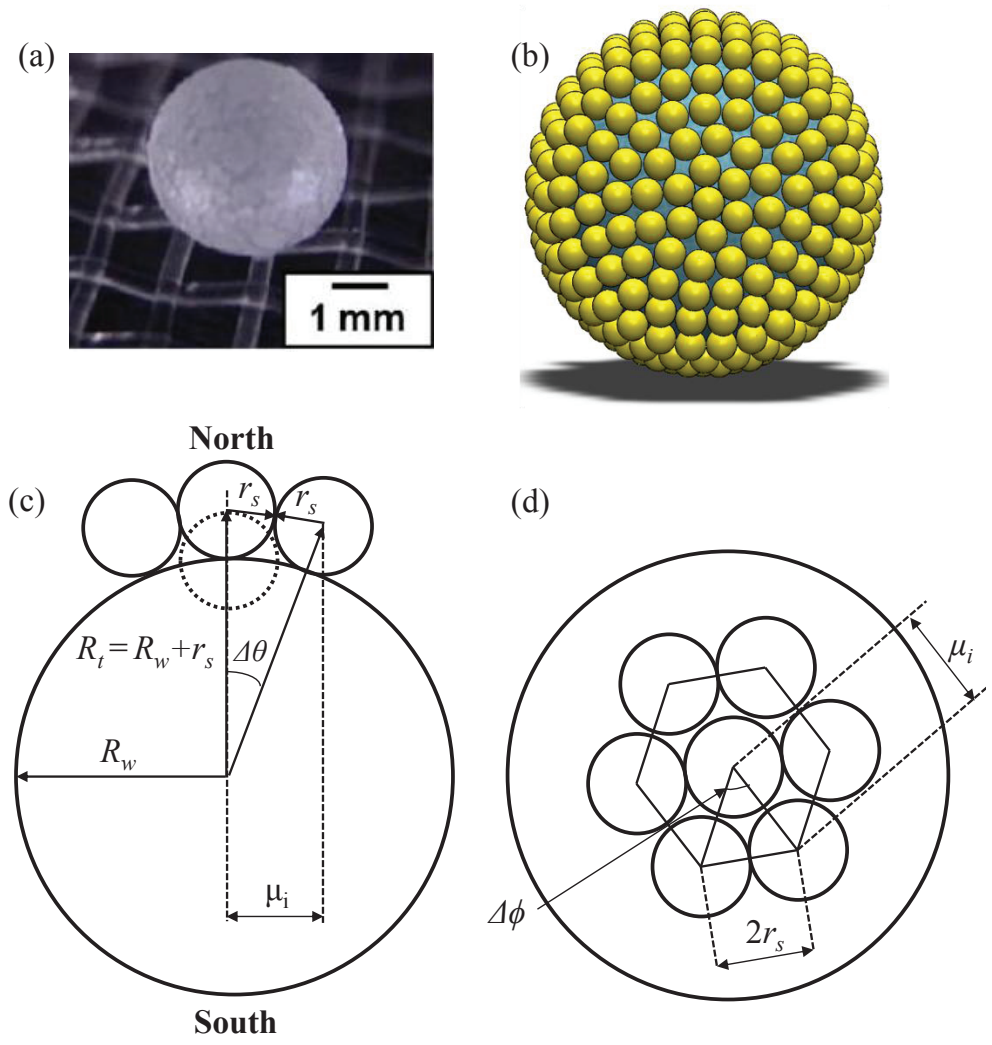

Figure 5.1: (a) Micrograph of liquid marble consisting of a water droplet coated with monodisperse polystyrene latex particles, 0.44 μm in diameter [16]. (b) General, (c) side, and (d) top view of simulated liquid marble along with geometric parameters.

Therefore, the number of spheres coating the core at the i^{th} level making up a complete ring of spheres is given by

$$q(i) = \frac{2\pi}{\Delta\phi_i}. \tag{5.11}$$

Then, in the spherical coordinate system, the coordinates of the centers of the tangential spheres, in terms of the azimuthal increment j and the i^{th} level is given by

$$(r, \theta, \phi) = (R_t, ({}_i\Delta\theta)_{0\leq i\leq p}, ({}_j\Delta\phi)_{0\leq j\leq q(i)}). \tag{5.12}$$

5.2.2 Modeling liquid marbles as equivalent coated spheres

Consider a liquid marble of core radius R_w coated with monodisperse spheres of radius r_s, as shown in Figure 5.1. Then, the volume equivalent radius of a liquid marble can be expressed as

$$r_{v,eq} = (R_w^3 + N_s r_s^3)^{1/3} \tag{5.13}$$

where $N_s = \sum_{i=0}^{p} q(i)$ refers to the total number of spheres coating the spherical core of radius R_w. The corresponding volume equivalent size parameter is given as

$$\chi_{v,eq} = \frac{2\pi r_{v,eq}}{\lambda} \tag{5.14}$$

where, λ represents the wavelength of the incident EM wave.

Furthermore, the projected area of a liquid marble particle is defined as the sum of the projected area of the spheres coating the core $A_{p,s}$ and of the spherical core $A_{p,w}$ expressed as [116]

$$A_p = A_{p,s} + A_{p,w} = 2p\pi r_s^2 + \pi R_w^2. \tag{5.15}$$

Then, the inner and outer radii of the volume and projected area equivalent coated sphere are respectively given by

$$r_{V+A_p,i} = [(A_p/\pi)^{3/2} - 2pr_s^3]^{1/3} \quad \text{and} \quad r_{V+A_p,o} = (2pr_s^2 + R_w^2)^{1/2}. \tag{5.16}$$

5.2.3 Radiation characteristics

First, the absorption Q_{abs} and scattering Q_{sca} efficiency factors, and asymmetry factor g of aqueous liquid marbles stabilized by latex or TiO_2 particles were computed using the superposition T-matrix method and the GOS method. The computer code implementing the superposition T-matrix method developed by Mackowski and Mishchenko [125] and that implementing the GOS method developed by Liou *et al.* [119, 120] were used. Both codes utilize (i) the spatial coordinates of the sphere centers given by Equation (5.12), (ii) the relative complex refractive index $m_{r,w} = m_w/n_m$ of the spherical core with respect to the surrounding medium and (iii) the relative complex index of refraction $m_{r,s} = m_s/n_m$ of the N_s spheres of radius r_s coating the core, and (iv) the size parameters of the core and coating spheres expressed, respectively, as

$$\chi_s = \frac{2\pi r_s}{\lambda} \quad \text{and} \quad \chi_w = \frac{2\pi R_w}{\lambda} \tag{5.17}$$

where, λ represents the wavelength of the incident EM wave. Due to limitations of the superposition T-matrix code in handling large size parameters, only size parameters, χ_s and χ_w ranging from 0.01 to 10 were examined using the superposition T-matrix method. Alternatively, the GOS method allowed for size parameters χ_w and χ_s, between 2 and 10,000 such that $\chi_{v,eq} > 10$.

The optical properties of the liquid water core and of the latex or TiO_2 coating spheres were obtained from Refs. [77, 126–128]. Here, the refraction index of the surrounding medium was taken to be that of air, $n_m = 1$, i.e, $m_{r,w} = m_w$ and $m_{r,s} = m_s$. At wavelength of 500 nm, latex and TiO_2 can be treated as non-absorbing [127, 128]. Then, the complex index of refraction of water was taken as $m_w = 1.33 + i10^{-9}$ [77], that of latex as $m_s = 1.6 + i0.0$ [126], and that of TiO_2 as $m_s = 2.16 + i0.0$ [127, 128]. Finally, at wavelength of 300 nm, the relative complex index of refraction of water and TiO_2 were taken as $m_w = 1.35 + i10^{-8}$ [77] and $m_s = 2.31 + i0.27$ [127, 128], respectively. The simulated liquid marbles featured a wide range of radii and size parameters. The spherical core and stabilizing spherical particle radii varied between 8.0 nm and 800 μm

and between 0.8 nm and 72 μm, respectively. This corresponds to size parameters χ_w and χ_s between 0.1 and 9,000 and 0.01 and 900, respectively. Three values of core-to-coating radii ratio R_w/r_s were considered, namely 10, 50, and 75.

The scattering and absorption efficiency factors obtained from the superposition T-matrix method and from the GOS method were converted to absorption C_{abs} and scattering C_{sca} cross-sections by multiplying them by the projected surface area of the volume equivalent sphere $\pi r_{v,eq}^2$ [125], i.e.,

$$C_{abs} = \pi r_{v,eq}^2 Q_{abs} \quad \text{and} \quad C_{sca} = \pi r_{v,eq}^2 Q_{sca}. \tag{5.18}$$

Alternatively, the absorption and scattering cross-sections of (i) volume and projected area equivalent coated spheres and (ii) dimensionally equivalent coated sphere with inner and outer radii $r_{R+2r,i} = R_w$ and $r_{R+2r,o} = R_w + 2r_s$, respectively, were calculated from Lorenz-Mie theory [129, 130] with the Matlab® code obtained from Ref. [131]. The scattering and absorption efficiency factors were computed based on the inner $\chi_{V+A_p,i}$ and outer $\chi_{V+A_p,o}$ size parameters corresponding to the inner and outer radii $r_{V+A_{p,i}}$ and $r_{V+A_{p,o}}$ given by Equation (5.16) and expressed as

$$\chi_{V+A_p,i} = \frac{2\pi r_{V+A_p,i}}{\lambda} \quad \text{and} \quad \chi_{V+A_p,o} = \frac{2\pi r_{V+A_p,o}}{\lambda}. \tag{5.19}$$

Then, the absorption $C_{abs,V+A_p}$ and scattering $C_{sca,V+A_p}$ cross-sections of the volume and projected area equivalent coated spheres were calculated according to

$$C_{abs/sca,V+A_p} = \pi r_{V+A_p,o}^2 Q_{abs/sca}(m_w, m_s, \chi_{V+A_p,i}, \chi_{V+A_p,o}). \tag{5.20}$$

The Lorenz-Mie theory for coated spheres was also used to determine the cross-sections of dimensionally equivalent coated spheres with respective core and coating shell radii $r_{R+2r,i} = R_w$ and $r_{R+2r,o} = R_w + 2r_s$ according to

$$C_{abs/sca,R+2r} = \pi r_{R+2r,o}^2 Q_{abs/sca}(m_w, m_s, \chi_{R+2r,i}, \chi_{R+2r,o}). \tag{5.21}$$

Furthermore, for the sake of comparison, the absorption $C_{abs,w}$ and scattering $C_{sca,w}$ cross-sections of the liquid marble were also compared with those of the aqueous core alone for cases when the coating particles were non-absorbing, i.e., at $\lambda = 500$ nm.

5.3 Results and discussion

5.3.1 Absorption cross-section

Figure 5.2 plots the absorption cross-sections C_{abs} of liquid marbles made of an aqueous core stabilized by (a) latex or (b) TiO_2 coating particles for $\lambda = 500$ nm and by (c) TiO_2 coating particles for $\lambda = 300$ nm, as functions of their respective volume equivalent size parameter $\chi_{v,eq}$. Several values of core-to-coating radii ratio R_w/r_s were considered namely 10, 50, and 75. The absorption cross-section was predicted by the superposition T-matrix method for χ_w and χ_s ranging from 0.01 to 10 and by the GOS method for χ_w and χ_s between 2 and 10,000. In all cases, it is evident that the absorption cross-sections increased monotonously with increasing volume equivalent size parameter $\chi_{v,eq}$. Figures 5.2a and 5.2b establish that the absorption cross-sections at 500 nm of liquid marbles stabilized with either latex or TiO_2 particles were independent of the ratio R_w/r_s and identical to one another.

Indeed, at this wavelength both latex and TiO_2 particles are non-absorbing and the absorption was only due to the aqueous core. In fact, Figures 5.2a and 5.2b also show the absorption cross-section of the liquid marble aqueous core alone predicted by the Lorenz-Mie theory for size parameter χ_w. Figure 5.3a and 5.3b plot the ratio of the absorption cross-sections C_{abs} predicted by the superposition T-matrix or GOS methods and the absorption cross-section $C_{abs,w}$ estimated from Lorenz-Mie theory for the liquid marble core alone as a function of the liquid marbles volume equivalent size parameter $\chi_{v,eq}$. They show good agreement between the exact predictions of the liquid marbles absorption cross-section and those estimated from Lorenz-Mie theory for the liquid marbles core. In fact, the results agreed on average within 10% of the superposition T-matrix method predictions for $\chi_{v,eq} \epsilon$ [0.1,10] and within 20% with the GOS method predictions for $\chi_{v,eq}$ ϵ [10,10,000]. In other words, the refracting but non-absorbing coating particles had no significant effect on the absorption cross-section of the liquid marbles. Note also that predictions for (i) the dimensionally equivalent coated spheres and (ii) for the volume

and projected area equivalent coated spheres did not provide better predictions of C_{abs}.

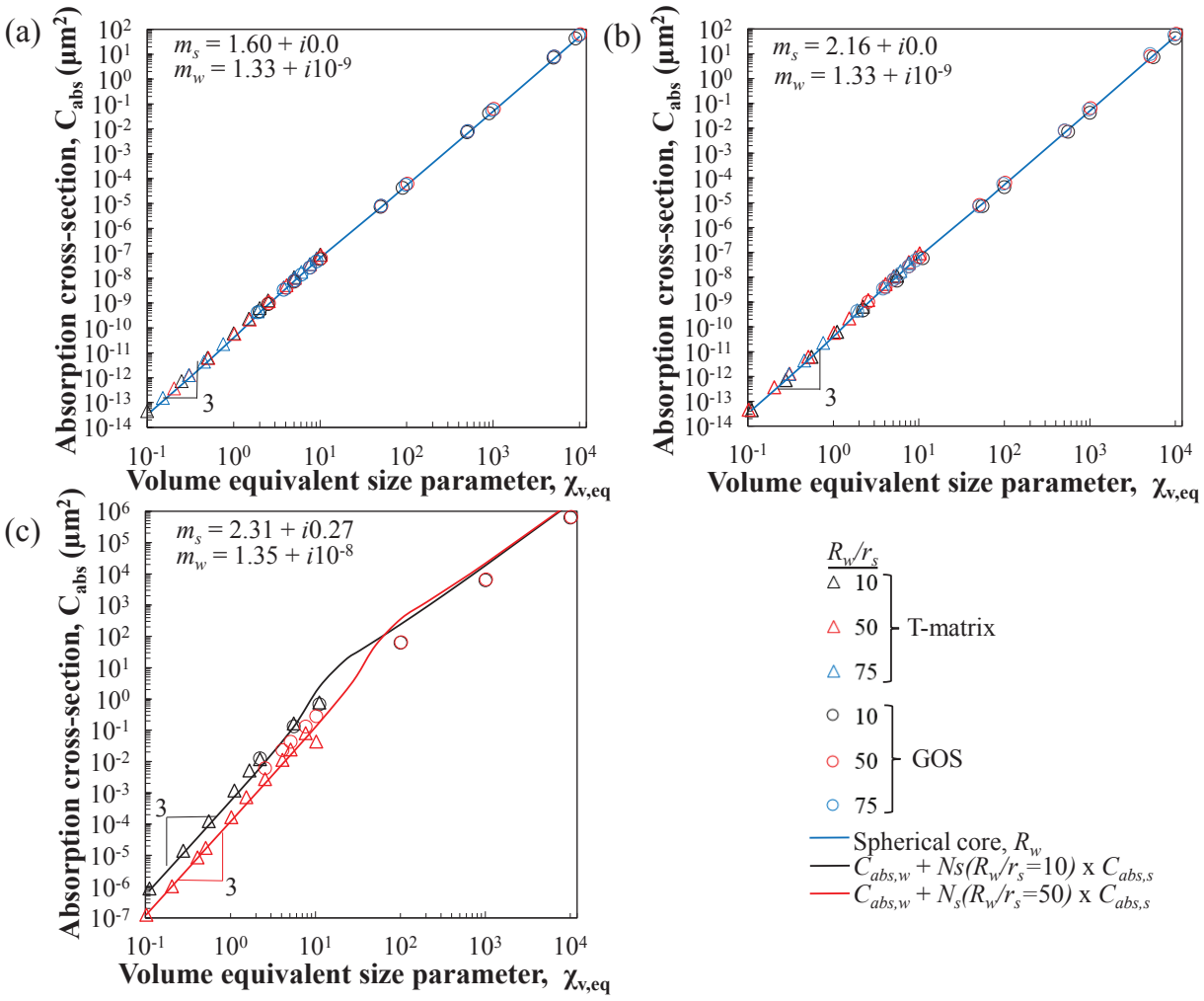

Figure 5.2: Absorption cross-sections predicted by the superposition T-matrix method and the GOS method for liquid marbles with core and coating particle complex index of refraction (a) $m_w = 1.33 + i10^{-9}$ and $m_s = 1.60 + i0.0$, (b) $m_w = 1.33 + i10^{-9}$ and $m_s = 2.16 + i0.0$, and (c) $m_w = 1.35 + i10^{-8}$ and $m_s = 2.31 + i0.27$. Also shown are predictions of C_{abs} for the liquid core alone and for the volume and projected area equivalent coated sphere, and a dimensionally equivalent coated sphere.

Finally, in the asymptotic case when $\chi_{v,eq} << 1$, the absorption cross-sections were

proportional to $\chi_{v,eq}^3$ according to Rayleigh scattering for a spherical water droplet [53].

On the other hand, Figure 5.2c establishes that the absorption cross-section of liquid marbles stabilized by TiO_2 particles was much larger at 300 nm than at 500 nm due to the fact that, at this wavelength, not only the core but also the coating particles absorbed the EM waves. In addition, for absorbing coating particles, the liquid marble absorption cross-section C_{abs} increased with decreasing ratio R_w/r_s. Indeed, in the case considered, the coating particles absorbed much more strongly than the water droplet. Therefore, the absorption cross-section of the liquid marble increased with increasingly large coating particles, i.e, decreasing ratio R_w/r_s. However, here also, the absorption cross-sections was proportional to $\chi_{v,eq}^3$ for $\chi_{v,eq} << 1$ with a coefficient of proportionality depending on R_w/r_s.

Figure 5.2c also compares the absorption cross-section predicted by the superposition T-matrix and GOS methods with the cumulative absorption cross-section of the liquid marble constituents, namely the aqueous core and the $N_s(R_w/r_s)$ coating particles expressed as

$$C_{abs,t} = C_{abs,w} + N_s(R_w/r_s) \times C_{abs,s}. \tag{5.22}$$

Here, $C_{abs,w}$ and $C_{abs,s}$ are the absorption cross-sections of the aqueous core and of a single coating particle predicted by Lorenz-Mie theory, respectively.

Figure 5.3c plots the ratio of the superposition T-matrix or GOS predicted absorption cross-sections C_{abs} and the absorption cross-section $C_{abs,t}$ estimated by Equation (5.22). Figure 5.3c shows good agreement between predictions by Equation (5.22) and those by the superposition T-matrix method for volume equivalent size parameter $\chi_{v,eq} < 1$. Unfortunately, poor agreement was observed between predictions for C_{abs} by the GOS method and by Equation (5.22). Finally, here again, predictions by the volume and projected area and dimensionally equivalent coated spheres did not agree with neither predictions by the superposition T-matrix or by the GOS methods and were not shown.

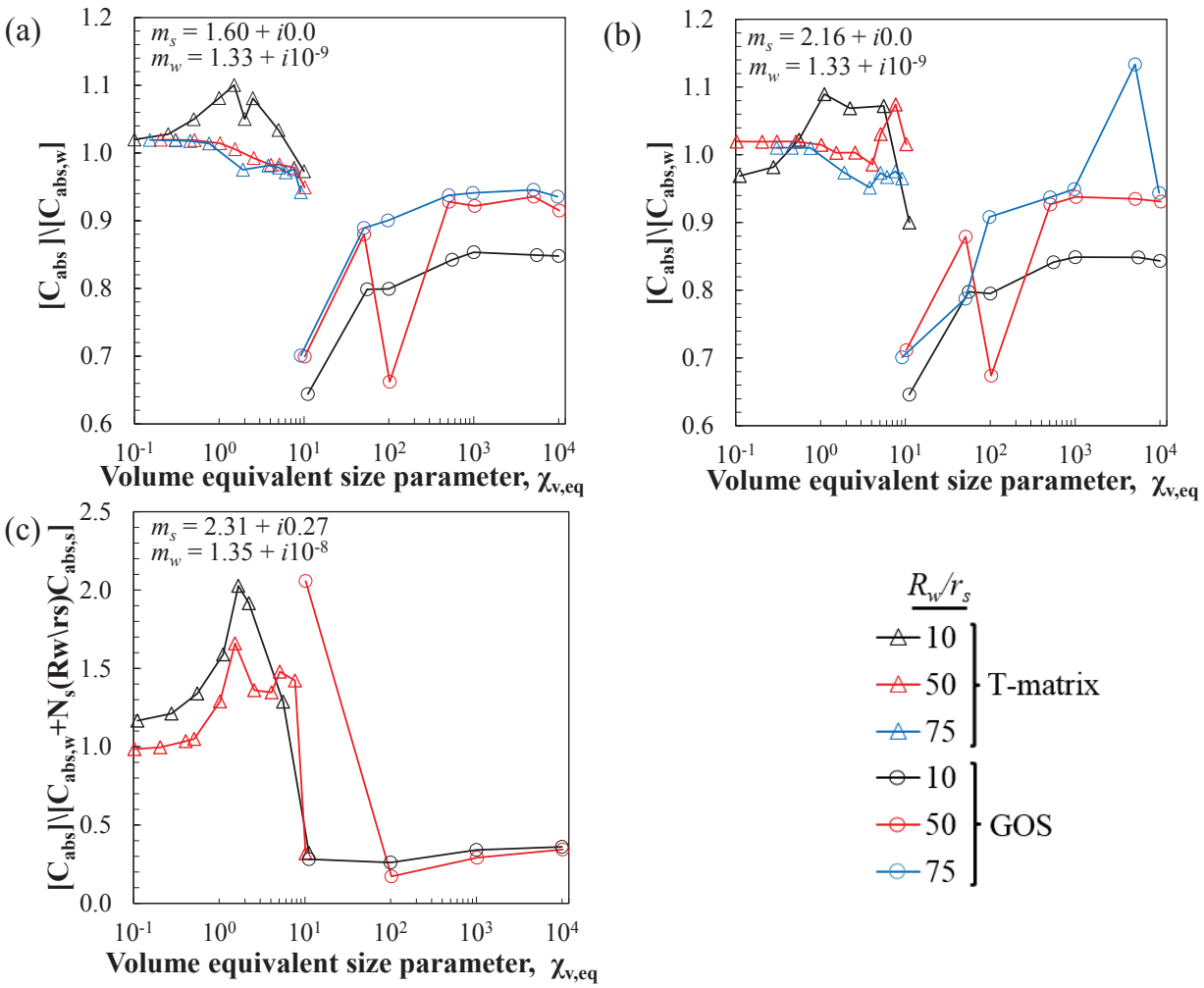

Figure 5.3: Ratio of absorption cross-sections predicted by the superposition T-matrix or GOS method and Lorenz-Mie theory for the liquid marble's aqueous core R_w for liquid marbles with core and coating particle complex index of refraction (a) $m_w = 1.33 + i10^{-9}$ and $m_s = 1.60 + i0.0$, (b) $m_w = 1.33 + i10^{-9}$ and $m_s = 2.16 + i0.0$, and (c) $m_w = 1.35 + i10^{-8}$ and $m_s = 2.31 + i0.27$.

5.3.2 Scattering cross-section

Figure 5.4 plots the scattering cross-sections C_{sca} of liquid marbles made of an aqueous core stabilized by (a) latex or (b) TiO_2 coating particles for $\lambda = 500$ nm and by (c) TiO_2 coating particles for $\lambda = 300$ nm, as functions of their respective volume equivalent size parameter $\chi_{v,eq}$. They corresponded to the same liquid marbles considered in Figure 5.2 for C_{abs}. Here also, the core-to-coating radii ratio R_w/r_s was taken as 10, 50, and 75. In all cases, it is evident that the scattering cross-sections increased monotonously with increasing volume equivalent size parameter $\chi_{v,eq}$. Figures 5.4a to 5.4b establish that the scattering cross-sections of liquid marbles stabilized with non-absorbing latex or TiO_2 particles were independent of the ratio R_w/r_s. In addition, for a given volume equivalent size parameter $\chi_{v,eq}$, the scattering cross-section of the liquid marbles stabilized with TiO_2 particles was larger than that of the latex particles. This was attributed to the larger index of refraction mismatch between the non-absorbing coating particles with respect to the aqueous core n_s/n_w and to the surrounding air n_s/n_m. Interestingly, the liquid marbles stabilized by absorbing TiO_2 particles at wavelength of 300 nm, had the smallest scattering cross-section despite having the largest refractive index mismatch relative to the aqueous core and surrounding medium (n_s =2.31). This was due to the fact that, at 300 nm, the TiO_2 particles were strongly absorbing ($k_s = 0.27$). Moreover, in the asymptotic regimes when $\chi_{v,eq} << 1$ and $\chi_{v,eq} >> 1$, the scattering cross-sections for all liquid marble considered were proportional to $\chi^6_{v,eq}$ and $\chi^2_{v,eq}$. These results were analogous to Rayleigh scattering ($\chi_{v,eq} <<1$) and geometric optics theory ($\chi_{v,eq} >>1$) for homogeneous spherical particles [53].

Additionally, Figures 5.4a to 5.4c plot the liquid marbles scattering cross-section estimated for (i) the liquid marbles aqueous core of radius R_w, (ii) the volume and projected area equivalent coated sphere, and (iii) the dimensionally equivalent coated sphere computed by Lorenz-Mie theory.

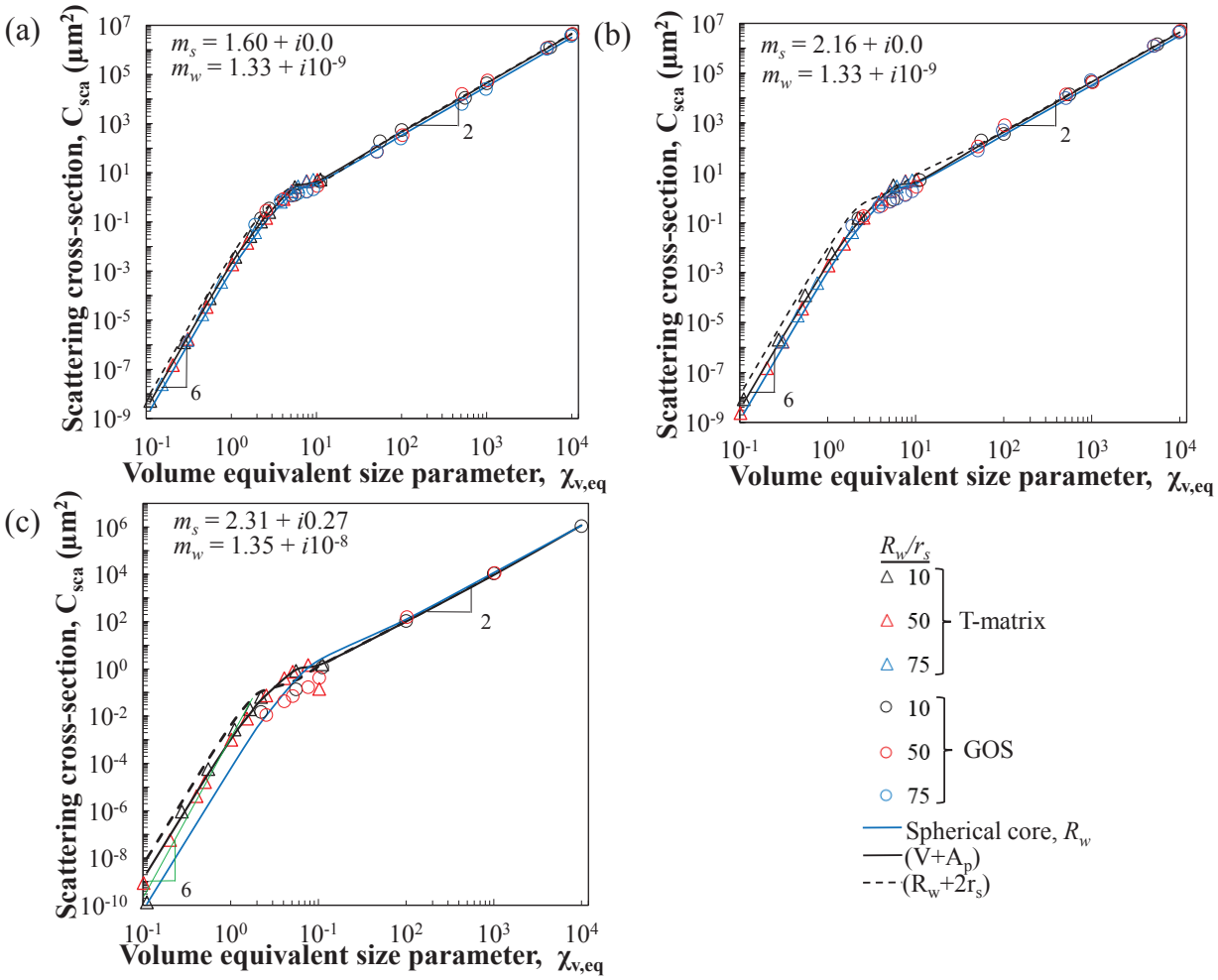

Figure 5.4: Scattering cross-sections predicted by the superposition T-matrix method and the GOS method for liquid marbles with core and coating particle complex index of refraction (a) $m_w = 1.33 + i10^{-9}$ and $m_s = 1.60 + i0.0$, (b) $m_w = 1.33 + i10^{-9}$ and $m_s = 2.16 + i0.0$, and (c) $m_w = 1.35 + i10^{-8}$ and $m_s = 2.31 + i0.27$. Also shown are predictions of C_{sca} for the liquid core alone and for the volume and projected area equivalent coated sphere, and a dimensionally equivalent coated sphere.

Figures 5.5a to 5.5c plot the ratio of the liquid marbles scattering cross-sections predicted by the superposition T-matrix or GOS methods and those estimated from Lorenz-Mie theory for an equivalent coated sphere that had identical volume and projected area. Good

agreement is observed between the predictions of the superposition T-matrix method and the volume and projected area equivalent coated sphere for liquid marbles stabilized by non-absorbing coating particles.

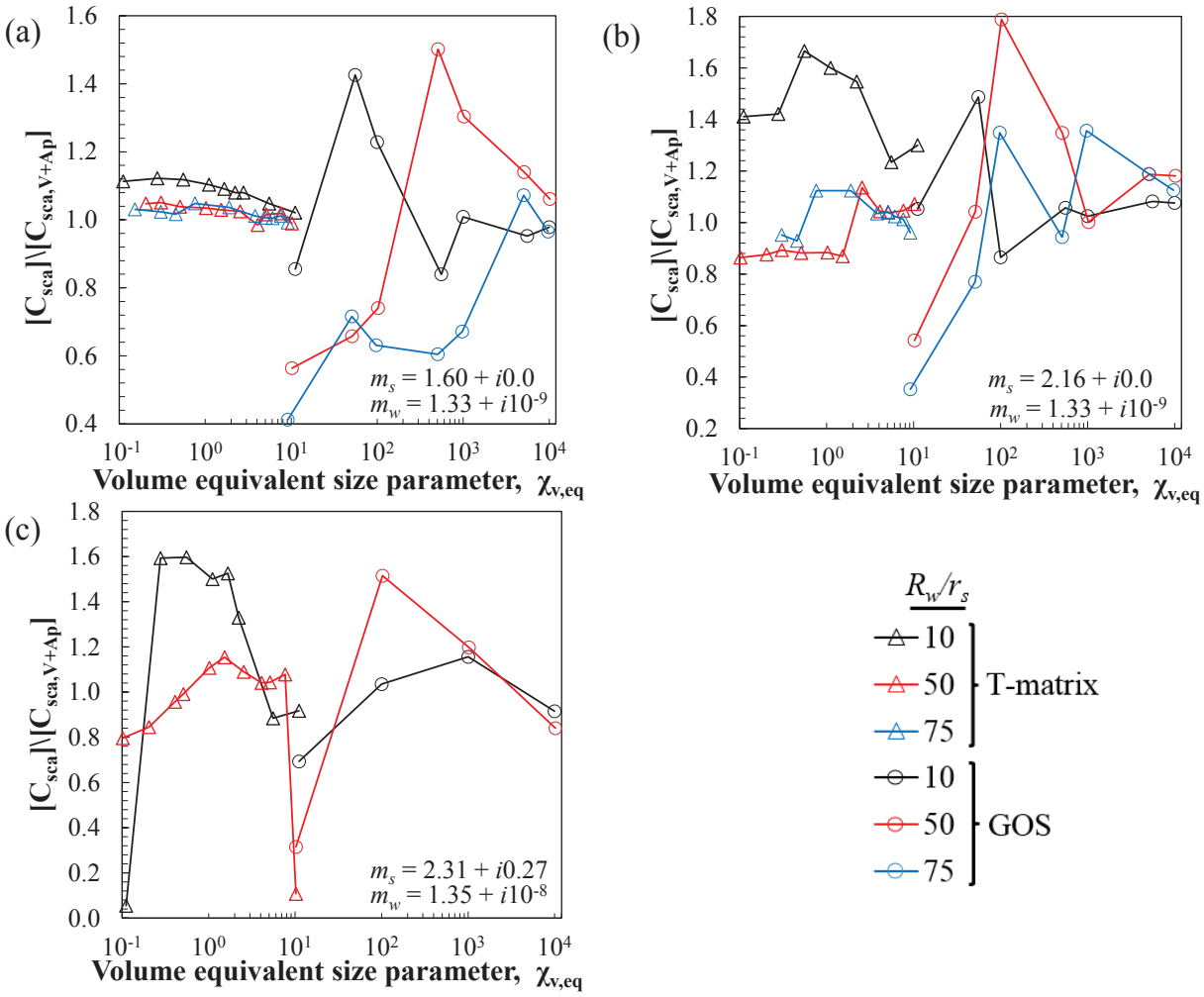

Figure 5.5: Ratio of the scattering cross-sections $[C_{sca}]/[C_{sca,V+A_p}]$ for the liquid marbles and their volume and projected area equivalent coated sphere with core and coating particle complex index of refraction (a) $m_w = 1.33 + i10^{-9}$ and $m_s = 1.60 + i0.0$, (b) $m_w = 1.33 + i10^{-9}$ and $m_s = 2.16 + i0.0$, and (c) $m_w = 1.35 + i10^{-8}$ and $m_s = 2.31 + i0.27$.

In fact, the volume and projected area equivalent coated sphere predictions agreed on

average within 15% of the superposition T-matrix method predictions of liquid marbles stabilized by non-absorbing coating particles for $\chi_{v,eq} \epsilon$ [0.1,10]. On the other hand, estimates using the liquid marbles aqueous core and the dimensionally equivalent coated sphere did not agree with the predictions from the superposition T-matrix nor with the GOS results.

5.3.2.1 Asymmetry factor

Figure 5.6 plots the asymmetry factor g corresponding to the liquid marbles discussed in the previous section as a function of the volume equivalent size parameter $\chi_{v,eq}$. In all cases, the liquid marbles exhibited forward scattering up to $\chi_{v,eq} \approx 6.0$. The inflection in $g(\chi_{v,eq})$ may be attributed to waveguide-like effects created in the region bounded by adjacent coating particles and the aqueous sphere [132]. Here again, the asymmetry factors were shown to be independent of the core-to-coating ratio R_w/r_s and nearly identical to one another for non-absobring coated spheres and a given liquid marble volume equivalent size parameter $\chi_{v,eq}$. Then, the scattering behavior of the liquid marble was dictated by its larger core dimensions, and the effect of the coating particles was minimal.

Figure 5.6 also plots the asymmetry factor estimated by Lorenz-Mie theory for the volume and projected area and dimensionally equivalent coated sphere approximations. The asymmetry factor predicted by the superposition T-matrix method and that predicted by the Lorenz-Mie theory for the volume and projected area equivalent coated sphere fell within 16% of each other for liquid marbles such that $\chi_{v,eq} < 10$. However, the asymmetry factors estimated from Lorenz-Mie theory for the dimensionally equivalent coated sphere did not agree with the predictions by either the superposition T-matrix or the GOS methods

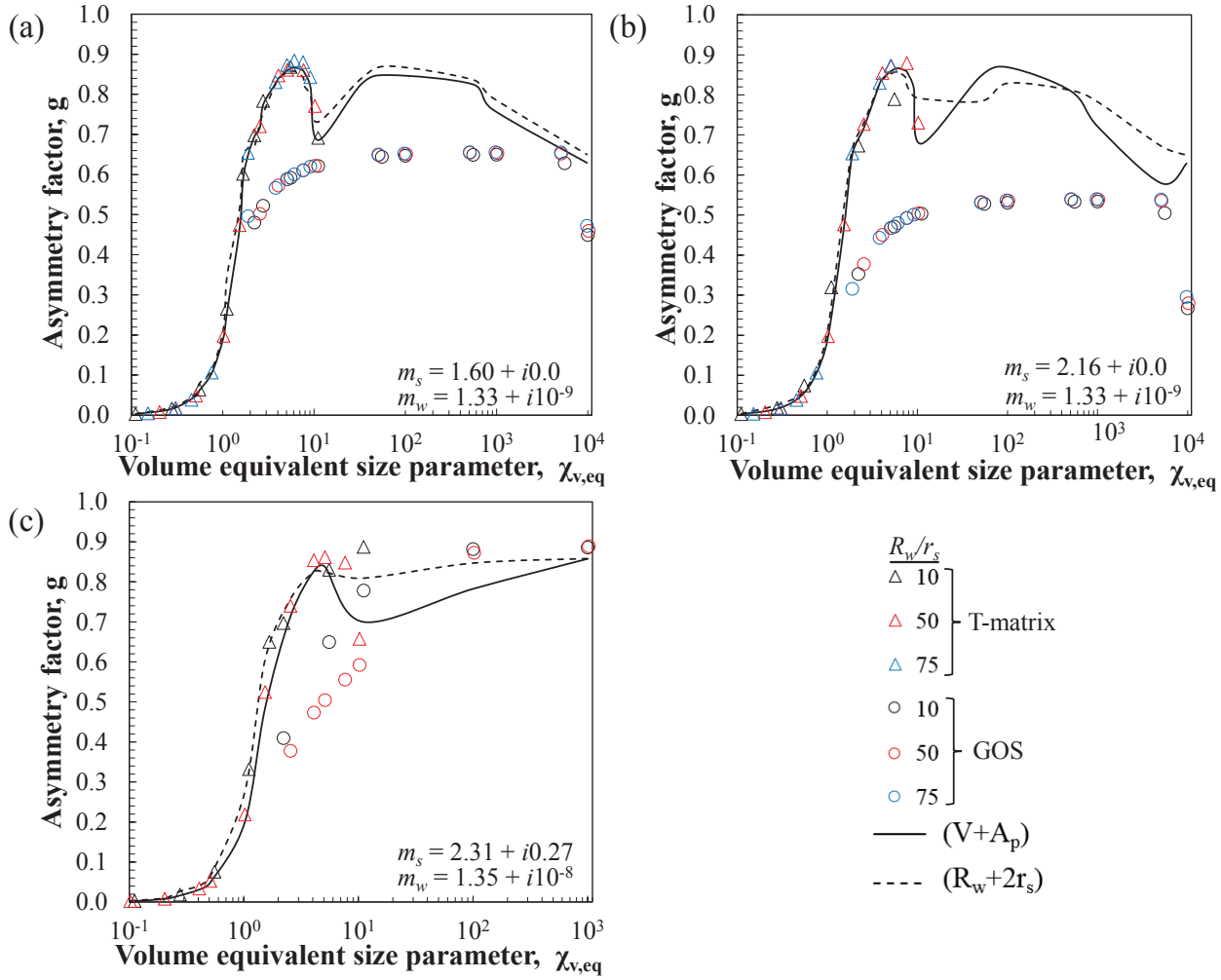

Figure 5.6: Asymmetry factor predicted by the superposition T-matrix method and the GOS method for liquid marbles with core and coating particle complex index of refraction (a) $m_w = 1.33 + i10^{-9}$ and $m_s = 1.60 + i0.0$, (b) $m_w = 1.33 + i10^{-9}$ and $m_s = 2.16 + i0.0$, and (c) $m_w = 1.35 + i10^{-8}$ and $m_s = 2.31 + i0.27$. Also shown are predictions of g for the liquid core alone and for the volume and projected area equivalent coated sphere, and a dimensionally equivalent coated sphere.

5.4 Chapter summary

This chapter predicted the integral radiation characteristics of liquid marbles made of an aqueous core stabilized by either absorbing or non-absorbing particles. Liquid marbles were modeled as a spherical core of radius R_w coated by highly-ordered tangential monodisperse spheres of radius r_s and were geometrically simulated according to core-and-coating radii ratio $R_w/r_s = 10$, 50, and 75, and volume equivalent size parameter $\chi_{v,eq}$ ranging from 0.1 to 10,000. The liquid marble's absorption and scattering cross-sections were shown to be independent of the core-to-coating radii ratio R_w/r_s and identical for cases where the stabilizing coating particles were non-absorbing. Furthermore, the absorption cross-sections of all the simulated liquid marbles were shown to be proportional to $\chi^3_{v,eq}$ for $\chi_{v,eq} << 1$ corresponding to the absorption behavior of a single sphere in the Rayleigh scattering regime. Similarly, the scattering cross-section was proportional to $\chi^6_{v,eq}$ for $\chi_{v,eq} << 1$ and $\chi^2_{v,eq}$ for $\chi_{v,eq} >> 1$ corresponding to the limiting cases of Rayleigh scattering and geometric optics theory, respectively, for a single sphere. Additionally, the liquid marble predicted asymmetry factors were found to be independent of R_w/r_s, and in fact nearly identical for a given $\chi_{v,eq}$, implying that the scattering phase function of liquid marble was dictated by the large core and that the influence of the small coating particles was minimal.

Finally, the absorption cross-section C_{abs} of liquid marbles stabilized by non-absorbing coating particles was shown to agree well with that of the aqueous core alone predicted by Lorenz-Mie theory. On the other hand, the scattering cross-section C_{sca} and asymmetry factor g for liquid marbles stabilized by non-absorbing coating particles were shown to agree well with those of the volume and projected area equivalent coated sphere approximation for volume equivalent size parameter $\chi_{v,eq} \leq 10$.

NOMENCLATURE

A_p	projected area (μm^2)
C	absorption or scattering cross-section (μm^2)
D_f	fractal dimension
F	ratio of total volume of particles to that of smallest sphere in an aggregate of particles
F_{ij}	scattering matrix elements
g	asymmetry factor
k	imaginary part of complex refractive index
m	complex refractive index, $m = n + ik$
N_s	total number of spherical particles necessary to completely coat the core
$N_{s,L}$	total number of particles in an aggregate
n	real part of complex refractive index
p	total number of spheres coating the core along the core meridian
Q	absorption or scattering efficiency factor
$q(i)$	total number of spheres coating the core at the i^{th} layer
R_w	sphere core radius (nm)
R_t	total aggregate radius, $R_t = R_w + r_s$ (m)
r_s	sphere coating radius (m)
$\mathbf{r}$	position vector
$\hat{s}$	direction vector

Greek symbols

$\Delta\theta$	latitudinal angle between adjacent spheres coating the core (rad)
$\Delta\phi$	longitudinal angle between adjacent spheres coating the core (rad)
Θ	scattering angle (deg)
λ	wavelength (m)
μ_i	distance between spheres positioned at the North pole and the i^{th} level (m)
χ	size parameter

Ω	solid angle (sr)

Subscript

abs	refers to absorption
ext	refers to extinction
i	index along the elevation direction of the spherical core, $i = 0, 1, 2, ...p$
j	index along the azimuthal direction of the spherical core, $j = 0, 1, 2, ...q(i)$
m	refers to the surrounding medium
min	minimum value
s	refers to the coating spheres
sca	refers to scattering
w	refers to the water spherical core

CHAPTER 6

Summary

The objective of the study was to develop further understanding of various transport phenomena in liquid foams and liquid marbles given their current availability in industry and potential for application in other industrial avenues. To this aim, identifying and developing governing equations and parameters that describe their mass, momentum, and thermal and radiative transport are requisite. The following summarizes the work undertaken to meet this objective.

The governing equation for the bubble radius time rate of change accounting for Ostwald ripening in foam was non-dimensionalized, yielding a dimensionless similarity parameter representative of the ratio of the average contact time between bubbles to the characteristic time for gas permeation was identified. Furthermore, building on the work of Pilon *et al.* [55], a semi-empirical model for predicting the steady-state height of liquid foams that accounts for Ostwald ripening or inter-bubble gas diffusion, derived from experimental data in this work and the literature, was developed.

Then, the stability of liquid foams generated by injecting air in aqueous surfactant solution contained in a glass column exposed to normally incident infrared radiation was experimentally investigated. Experimental results demonstrated that the steady-state foam height decreased with higher incident radiation intensities. Secondly, a one-dimensional reduced-order thermal model accounting for combined conduction and radiation in the foam layer was shown to agree reasonably well with temperature data taken across the steady-state foam layer.

Furthermore, experimental data for laminar forced convection of liquid foams flowing

in circular pipes was reported. This experimental data and data reported in the literature for foams flowing laminarly in rectangular pipes and across tube bundles was compared to analytical and semi-empirical models governing heat transfer in single-phase power-law fluids. These models were extended and shown to agree well with the experimental foam data by defining the foam's momentum properties (i.e. Reynolds number) in terms of the effective foam properties and the foam thermal properties (i.e. Nusselt and Prandtl numbers) in terms of the foam's liquid phase properties. This approach was based on the fact that in liquid foam flows a thin layer of liquid is in contact with the heat transfer boundary thus controlling convective heat transfer to bulk foam.

Finally, the integral radiative properties of liquid marbles stabilized by either absorbing or non-absorbing coatings and exposed to visible and infrared radiation were reported. Numerical data was acquired via the superposition T-matrix and GOS computational algorithms that were a function of the liquid marble optical properties, geometry, size, and spatial coordinates. A code was developed to retrieve the spatial coordinates of the liquid marble constituents that was modeled as a spherical core coated by highly-ordered tangential monodisperse spheres. The numerical results demonstrated that the liquid marbles absorption and scattering cross-sections were independent of the number coating particles used to stabilize the liquid marble when the coatings were non-absorbing. Secondly, the liquid marbles absorption cross-sections were shown to behave like a single sphere's absorption in the limiting case of Rayleigh scattering. Likewise, the scattering cross-sections were demonstrated to to be akin to the behavior of a single sphere in the limits of Rayleigh scattering and geometric optics theory. In fact, the asymmetry factors were also shown to be independent of the number of coating particles used to stabilize the liquid marble; indicating the effect of the coating particles was minimal. Secondly, for liquid marbles stabilized by non-absorbing coatings, the absorption cross-section calculated from the superposition T-matrix and GOS algorithms were shown to agree well with data obtained from Lorenz-Mie theory for a single sphere that only accounted for the liquid marble's core geometry and optical properties. Similarly, for liquid marbles

stabilized by non-absorbing coatings and of small size parameter, the scattering cross-section and asymmetry parameter were shown to agree well with data obtained from Lorenz-Mie theory for a volume and projected area equivalent coated sphere.

Overall, with respect to liquid foams, these results can be used to predict steady-state height foam generation and their response to infrared radiation in industrial settings where foam is either an undesirable byproduct of a manufacturing process or utilized as part of a process. Likewise, the results provide theoretical framework for modeling and potential usage of liquid foams in heat exchanger systems as well as for other applications involving convective heat transfer of liquid foams. Lastly, numerical data of the integral radiation properties governing electromagnetic wave interaction with liquid marbles provide insight on how they can be most efficiently used as a functional material. Finally, approximate modeling of liquid marbles via simplified equivalent geometries provide a computationally inexpensive means of identifying their integral radiation characteristics for use as a photoresponsive functional material or in optofluidic applications.

References

[1] L. Pilon, A. G. Fedorov, and R. Viskanta, "Analysis of transient thickness of pneumatic foams", *Chemical Engineering Science*, vol. 57, pp. 977–990, 2002.

[2] S. A. K. Jeelani, S. Ramaswami, and S. Hartland, "Effect of binary coalescence on steady-state height of semi-batch foams", *Transaction of the Institution of Chemical Engineers*, vol. 68, Part A, pp. 271–277, 1990.

[3] S. Hartland, J. R. Bourne, and S. Ramaswami, "A study of disproportionation effects in semi-batch foams - II. Comparison between experiment and theory", *Chemical Engineering Science*, vol. 48, pp. 1723–1733, 1993.

[4] K. Feitosa, O. L. Halt, R. D. Kamien, and D. J. Durian, "Bubble kinetics in a steady-state column of aqueous foam", *Europhysics Letters*, vol. 76, pp. 683689, 2006.

[5] K. Feitosa and D. J. Durian, "Gas and liquid transport in steady-state aqueous foam", *The European Physical Journal E*, vol. 26, pp. 309316, 2008.

[6] S.J. Neethling, H.T. Lee, and P. Grassia, "The growth, drainage and breakdown of foams", *Colloids and Surfaces A: Physicochem. Eng. Aspects*, vol. 263, pp. 184196, 2005.

[7] A. Lavergne, Y. Zhu, A. Pizzino, V. Molinier, and J.M. Aubry, "Synthesis and foaming properties of new anionic surfactants based on a renewable building block: Sodium dodecyl isosorbide sulfates", *Journal of Colloid and Interface Science*, vol. 360, no. 2, pp. 645653, 2011.

[8] X. Li, R. Shaw, and P. Stevenson, "Effect of humidity on dynamic foam stability", *International Journal of Mineral Processing*, vol. 94, pp. 14–19, 2010.

[9] W.M. Kays, M.E. Crawford, and B. Weigand, *Convective Heat and Mass Transfer*, McGraw-Hill, New York, NY, fourth edition, 2005.

[10] S. Kakac and Y. Yenner, *Convective Heat Transfer*, CRC Press, Boca Raton, FL, second edition, 1995.

[11] R.B. Bird, "On the theory of heat transfer of non-Newtonian fluid in laminar pipe flow", *Chemie Ingenieur Technik*, vol. 31, no. 9, pp. 569–572, 1959.

[12] S.D. Joshi and A.E. Bergles, "Experimental study of laminar heat transfer to in-tube flow of non-Newtonian fluids", *ASME Journal of Heat Transfer*, vol. 102, no. 3, pp. 397–401, 1980.

[13] H. Tseng, L. Pilon, and G.R. Warrier, "Rheology and convective heat transfer of colloidal gas aphrons in horizontal mini-channels", *International Journal of Heat and Fluid Flow*, vol. 27, pp. 298–310, 2006.

[14] J. Gylys, T. Zdankus, R. Jonynas, and R. Maladauskas, "Experimental investigation of in-line tube bundle heat transfer process to vertical downward foam flow", *International Journal of Heat and Mass Transfer*, vol. 54, no. 11-12, pp. 2326 – 2333, 2011.

[15] J. Gylys, S. Sinkunas, and T. Zdankus, "Analysis of staggered tube bundle heat transfer to vertical foam flow", *International Journal of Heat and Mass Transfer*, vol. 51, no. 1-2, pp. 253 – 262, 2008.

[16] K.Ueno, S. Hamasaki, E. J. Wanless, Y. Nakamura, and S. Fujii, "Microcapsules fabricated from liquid marbles stabilized with latex particles", *Langmuir*, vol. 30, pp. 3051–3059, 2014.

[17] L.L. Schramm and E.E. Isaacs, "Foams in enhancing petroleum recovery", in *Foam Engineering: Fundamentals and Applications*, P. Stevenson, Ed., pp. 149–160. Wiley-Blackwell, United Kingdom, 2012.

[18] C.E. Lockwood, P.M. Bummer, and M. Jay, "Purification of proteins using foam fractionation", *Pharmaceutical Research*, vol. 14, no. 11, pp. 1511–1515, 1997.

[19] G. Narsimhan, "A model for unsteady state drainage of a static foam", *Journal of Food Engineering*, vol. 14, pp. 139–165, 1991.

[20] R. J. Germick, A. S. Rehill, and G. Narsimhan, "Experimental investigation of static drainage of protein stabilized foams - Comparison with model", *Journal of Food Engineering*, vol. 23, pp. 555–578, 1994.

[21] I. A. Eldib, "Foam fractionation for removal of soluble organics from wastewater", *Research Journal of the Water Pollution and Control Federation*, vol. 33, no. 9, pp. 914–931, 1961.

[22] L. Pilon, "Foams in glass manufacturing", in *Foam Engineering*, P. Stevenson, Ed., pp. 149–160. John Wiley & Sons Ltd., UK, 2012.

[23] K. Ito and R. J. Fruehan, "Study of the foaming of CaO-SiO_2-FeO slags: Part II. Dimensional analysis and foaming in iron and steelmaking processes", *Metallurgical and Materials Transactions B*, vol. 20B, pp. 515–521, 1989.

[24] R. Jiang and R. J. Fruehan, "Slag foaming in bath smelting", *Metallurgical and Materials Transactions B*, vol. 22B, pp. 481–489, 1991.

[25] S-M Jung and R. J. Fruehan, "Foaming characteristics of BOF slags", *ISIJ International*, vol. 40, pp. 348–354, 2000.

[26] F. Sebba, *Foams and Biliquid Foams-Aphrons*, John Wiley & Sons, New York, NY, 1987.

[27] P. Jauregi, G.R. Mitchell, and J. Varley, "Colloidal gas aphrons (CGA): dispersion and structural features", *AIChE Journal*, vol. 46, no. 1, pp. 24–36, 2000.

[28] G. Spigno and P. Jauregi, "Recovery of gallic acid with colloidal gas aphrons (CGA)", *International Journal of Food Engineering*, vol. 1, no. 4, Article 5, 2005.

[29] P. Jauregi and J. Varley, "Colloidal gas aphrons: a novel approach to protein recovery", *Biotechnology and Bioengineering*, vol. 59, pp. 471–481, 1998.

[30] D. Roy, K.T. Valsarag, W.D. Constant, and M. Darji, "Removal of hazardous oily waste from a soil matrix using surfactants and collodial gas aphron suspensions under different flow conditions", *Journal of Hazardous Materials*, vol. 38, pp. 127–144, 1994.

[31] D. Roy, R.R. Kommalapti, K.T. Valsarag, and W.D. Constant, "Soil flushing of residual transmission fluid: application of colloidal gas aphron suspensions and conventional surfactant solutions", *Water Research*, vol. 29, pp. 589–595, 1995.

[32] R.W. Grimes, "Evaluation of a method using colloidal gas aphrons to remediate metals contaminated mine drainage waters", Western Research Institute Report WRI-02-R007, 2002.

[33] S. Ciriello, S.M. Barnett, and F.J. Deluise, "Removal of heavy-metals from aqueous-solutions using microgas dispersions", *Separation Science and Technology*, vol. 4, pp. 521–534, 1982.

[34] J. Weber and F.A. Agblevor, "Microbubble fermentation of *trichoderma reesei* for cellulase production", *Process Biochemistry*, vol. 40, no. 2, pp. 669–676, 2005.

[35] M.D. Bredwell and R.M. Worden, "Mass transfer properties of microbubbles. 1. Experimental Studies", *Biotechnology Progress*, vol. 14, pp. 31–38, 1998.

[36] N.S. Deshpande and M. Barigou, "The flow of gas-liquid foams through pipe fittings", *International Journal of Heat and Fluid Flow*, vol. 22, pp. 94–101, 2001.

[37] X. Sun, S. Wang, Y. Bai, and S. Liang, "Rheology and convective heat transfer properties of borate cross-linked nitrogen foam fracturing fluid", *Heat Transfer Engineering*, vol. 32, no. 1, pp. 69–79, 2010.

[38] P. Aussillous and D. Quéré, "Liquid marbles", *Nature*, vol. 411, pp. 924–927, 2001.

[39] T. T. Y. Tan, A. Ahsan, M. R. Reithofer, S. W. Tay, S. Y. Tan, T. S. A. Hor, J. M. Chin, B. K. J. Chew, and X. Wang, "Photoresponsive liquid marbles and dry water", *Langmuir*, vol. 30, pp. 3448–3454, 2014.

[40] G. McHale and M. I. Newton, "Liquid marbles: Principles and applications", *Soft Matter*, vol. 7, pp. 5473–5481, 2011.

[41] B. P. Binks and R. Murakami, "Phase inversion of particle-stabilized materials from foams to dry water", *Nature Materials*, vol. 5, pp. 865–869, 2006.

[42] O. Taylan and H. Berberoğlu, "Thermal radiation transport in fluidized dry water system", *Journal of Quantitative Spectroscopy and Radiative Transfer*, vol. 120, pp. 104–113, 2013.

[43] P. Aussillous and D. Quéré, "Properties of liquid marbles", *Proceeding of The Royal Society A*, vol. 462, pp. 973–999, 2006.

[44] E. Bormashenko, "Liquid marbles: Properties and applications", *Current Opinion in Colloid and Interface Science*, vol. 16, pp. 266–271, 2011.

[45] D. Dupin, S. Armes, and S. Fujii, "Stimulus-responsive liquid marbles", *Journal of the American Chemical Society Communication*, vol. 131, pp. 5386–5387, 2009.

[46] S. Fujii, M. Suzaki, S. P. Armes, D. Dupin, S. Hamasaki, K. Aono, and Y. Nakamura, "Liquid marbles prepared from pH-responsive sterically stabilized latex particles", *Langmuir*, vol. 27, pp. 8067–8074, 2011.

[47] S. Yusa, M. Morihara, K. Nakai, S. Fujii, Y. Nakamura, A. Maruyama, and N. Shimada, "Thermo-responsive liquid marbles", *Polymer Journal*, vol. 46, pp. 145–148, 2014.

[48] L. Zhang, D. Cha, and P. Wang, "Remotely controllable liquid marbles", *Advanced Materials Communication*, vol. 24, no. 35, pp. 4756–4760, 2012.

[49] K. Nakaiu, S. Fujii, Y. Nakamura, and S. Yusa, "Ultraviolet-light-responsive liquid marbles", *Chemistry Letters*, vol. 42, no. 6, pp. 586–588, 2013.

[50] J.M. Chin, S. W. Tay, X. Wang, J. Xu, and A. T. S. Hor, "Photo-responsive macro- and micro- liquid marbles", *International Patent*, , no. WO2014126536 A1, August 21, 2014.

[51] V. Sivan, S.Y. Tang, A. P. OMullane, P. Petersen, N. Eshtiaghi, K. Kalantar-zadeh, and A. Mitchell, "Liquid metal marbles", *Advanced Functional Materials*, vol. 23, pp. 144–152, 2013.

[52] X. Tang, S.Y. Tang, V. Sivan, W. Zhang, A. Mitchell, K. Kalantar-Zadeh, and K. Khoshmanesh, "Photochemically induced motion of liquid metal marbles", *Applied Physics Letters*, vol. 103, pp. 174104–1–174104–4, 2013.

[53] C.F. Bohren and D.R. Huffman, *Absorption and Scattering of Light by Small Particles*, John Wiley & Sons, New York, NY, 1998.

[54] C. F. Boyd and M. Di Marzo, "The behavior of a fire-protection foam exposed to radiant heating", *International Journal of Heat and Mass Transfer*, vol. 41, pp. 1719–1728, 1998.

[55] L. Pilon, A. G. Fedorov, and R. Viskanta, "Steady-state foam thickness of liquid-gas foams", *Journal of Colloid and Interface Science*, vol. 242, pp. 425–436, 2001.

[56] F. G. Gandolfo and H. L. Rosano, "Interbubble gas diffusion and the stability of foams", *Journal of Colloid and Interface Science*, vol. 194, pp. 31–36, 1997.

[57] S. Hilgenfeldt, S. Koehle, and H. Stone, "Dynamics of coarsening foams: Accelerated and self-limiting drainage", *Physical Review Letters*, vol. 86, no. 20, pp. 4704–4707, 2001.

[58] R. Lemlich, "Prediction of changes in bubble size distribution due to interbubble gas diffusion in foam", *Industrial & Engineering Chemistry Fundamentals*, vol. 17, no. 2, pp. 89–93, 1978.

[59] A. Colin, "Coalescence in foams", in *Foam Engineering*, P. Stevenson, Ed., pp. 75–90. John Wiley & Sons Ltd., UK, 2012.

[60] O. Pitois, "Foam ripening", in *Foam Engineering*, P. Stevenson, Ed., pp. 59–73. John Wiley & Sons Ltd., UK, 2012.

[61] S. Tcholakova, Z. Mitrinova, K. Golemanov, N. D. Denkov, M. Vethamuthu, and K.P. Ananthapadmanabhan, "Control of ostwald ripening by using surfactants with high surface modulus", *Langmuir*, vol. 27, pp. 14807–14819, 2011.

[62] A. Bhakta and E. Ruckenstein, "Decay of standing foams: drainage, coalescence and collapse", *Advances in Colloid and Interface Science*, vol. 70, pp. 1–124, 1997.

[63] L. Pilon and R. Viskanta, "Minimum superficial gas velocity for onset of foaming", *Chemical Engineering and Processing*, vol. 43, no. 2, pp. 149–160, 2004.

[64] S. Hartland and A. D. Barber, "A model for cellular foam", *Transactions of the Institution of Chemical Engineers*, vol. 52, pp. 43–52, 1974.

[65] H.M. Princen and S.G. Mason, "The permeability of soap films to gases", *Journal of Colloid Science*, vol. 20, pp. 353–375, 1965.

[66] R. Battino, "The Ostwald coefficient of gas solubility", *Fluid Phase Equilibria*, vol. 15, pp. 231–240, 1984.

[67] D. Lotun and L. Pilon, "Physical modeling of slag foaming for various operation conditions and slag compositions", *ISIJ International*, vol. 45, no. 6, pp. 835–840, 2005.

[68] J. Zhao, S. Pillai, and L. Pilon, "Rheology of microfoams made from ionic and non-ionic surfactant solutions", *Colloids and Surfaces A: Physicochemical and Engineering Aspects*, vol. 348, no. 1-3, pp. 93–99, 2009.

[69] R. Wilke and P. Chang, "Correlation of diffusion coefficients in dilute solutions", *American Institute of Chemical Engineers Journal*, vol. 1, pp. 264–270, 1955.

[70] H. Cheng and R. Lemlich, "Errors in the measurement of bubble size distribution in foam", *Industrial & Engineering Chemistry Fundamentals.*, vol. 22, pp. 105–109, 1983.

[71] Y. Ogawa, D. Huin, H. Gaye, and N. Tokumitsu, "Physical model of slag foaming", *ISIJ International*, vol. 33, no. 1, pp. 224–232, 1993.

[72] M. F. Modest, *Radiative Heat Transfer*, Academic Press, San Diego, CA, 2003.

[73] A. G. Fedorov and R. Viskanta, "Radiative transfer in a semitransparent glass foam blanket", *Physics and Chemistry of Glasses*, vol. 41, no. 3, pp. 127–135, 2000.

[74] L. Pottier, J. Pruvost, J. Deremetz, J. F. Cornet, J. Legrand, and C. G. Dussap, "A fully predictive model for one-dimensional light attenuation by *Chlamydomonas reinhardtii* in a torus photobioreactor", *Biotechnology and Bioengineering*, vol. 91, no. 5, pp. 569582, 2005.

[75] J. Zhao, S. Pillai, and L. Pilon, "Rheology of colloidal gas aphrons (microfoams) made from different surfactants", *Colloids and Surfaces A: Physicochemical and Engineering Aspects*, vol. 348, pp. 93–99, 2009.

[76] D. MacIsaac, G. Kanner, and G. Anderson, "Basic physics of the incandescent lamp (lightbulb)", *The Physics Teacher*, vol. 37, pp. 520–525, 1999.

[77] G. M. Hale and M. R. Querry, "Optical constants of water in the 200-nm to 200-m wavelength region", *Applied Optics*, vol. 12, pp. 555–563, 1973.

[78] G. C. J. Bart, *Thermal Conduction in Non Homogeneous and Phase Change Media*, PhD thesis, Delft University of Technology, 1987.

[79] S. Larmignat, D. Vanderpool, H.K. Lai, and L. Pilon, "Rheology of colloidal gas aphrons (microfoams)", *Colloids and Surface A: Physicochemical and Engineering Aspects*, vol. 322, pp. 199–210, 2008.

[80] H. C. van de Hulst, *Light Scattering by Small Particles*, John Wiley & Sons, New York, NY, 1957.

[81] M. U. Vera, A. Saint-Jalmes, and D. J. Durian, "Scattering optics of foams", *Applied Optics*, vol. 40, no. 24, pp. 4210–4214, 2001.

[82] F.A. Morrison, *Understanding Rheology*, Oxford University Press, Oxford, UK, 2001.

[83] N.D. Denkov, V. Subramanian, D. Gurovich, and A. Lips, "Wall slip and viscous dissipation in sheared foams: Effect of surface mobility", *Colloids and Surfaces A: Physicochemical and Engineering Aspects*, vol. 263, pp. 129–145, 2005.

[84] N.D. Denkov, S. Tcholakova, K. Golemanov, V. Subramanian, and A. Lips, "Foam wall friction: Effect of air volume fraction for tangentially immobile bubble surface", *Colloids and Surfaces A: Physicochemical and Engineering Aspects*, vol. 282-283, pp. 329–347, 2006.

[85] T. Mizushina, R. Ito, Y. Kuriwake, and K. Yahikazawa, "Boundary layer heat transfer in a circular tube to Netwonian and non-Newtonian fluids", *Kagaku Kogaku*, vol. 32, pp. 250–255, 1967.

[86] S.W. Churchhill and R. Usagi, "Dissolution of polydisperse silica grains in glass melts - analysis", *American Institute of Chemical Engineers Journal*, vol. 27, no. 5, pp. 1121–1128, 1972.

[87] P. Wibulswas, *Laminar Flow Heat Transfer in Noncircular Ducts*, PhD thesis, London University, London, U.K., 1966.

[88] F. P. Incropera and D. P. DeWitt, *Fundamentals of Heat and Mass Transfer*, John Wiley & Sons, New York, NY, Fourth edition, 1996.

[89] P.S. Lee and S.V. Garimella, "Thermally developing flow and heat transfer in rectangular microchannels of different aspect ratios", *International Journal of Heat and Mass Transfer*, vol. 49, pp. 3060–3067, 2006.

[90] R.J. Phillips, "Microchannel heat sinks", Master's thesis, Massachusetts Institute of Technology, Cambridge, MA, USA, 1987.

[91] R.K. Shah and A.L. London, *Laminar Flow Forced Convection in Ducts*, Academic Press, New York, NY, 1978.

[92] W.A. Khan, J.R. Culham, and M.M. Yovanovich, "Fluid flow around and heat transfer from an infinite circular cylinder", *ASME Journal of Heat Transfer*, vol. 127, pp. 785–790, 2005.

[93] W.A. Khan, J.R. Culham, and M.M. Yovanovich, "Convection heat transfer from tube banks in crossflow: Analytical approach", *International Journal of Heat and Mass Transfer*, vol. 49, pp. 4831–4838, 2006.

[94] Design Institute for Physical PRoperties, "Thermophysical properties database DIPPR 801", http://www.aiche.org/dippr/products/801.aspx, 2012.

[95] H.W. Russell, "Principles of heat flow in porous insulators", *Journal of the American Ceramic Society*, vol. 18, pp. 1–5, 1935.

[96] G.S. son Frey, "Über die elektrische Leitfähigkeit binärer Aggregate", *Zeitschrift für Elektrochemie und angewandte physikalische Chemie*, vol. 38, no. 5, pp. 260–274, 1932.

[97] Lord Rayleigh, "On the influence of obstacles arranged in rectangular order upon the properties of a medium", *Philosophical Magazine*, vol. 34, pp. 481–502, 1892.

[98] D.A. De Vries, "The thermal conductivity of granular materials", *Annex 1952-1 Bulletin of the International Institute of Refrigeration*, pp. 115–131, 1952.

[99] J.C. Maxwell, *A Treatise on Electricity and Magnetism*, vol. 1, Oxford University, New York, NY, 3rd edition, 1892.

[100] D.A.G. Bruggeman, "Berechnung verschiedener physikalischer konstanten von heterogenen substanzen", *Annalen der Physik*, vol. 24, no. 2, pp. 636–679, 1935.

[101] B. Alazmi and K. Vafai, "Analysis of variants within the porous media transport models", *International Journal for Numerical Methods in Fluids*, vol. 122, no. 2, pp. 303–326, 2000.

[102] J. Lévêque, "Les lois de la transmission de la chaleur par convection", *Annales des Mines*, vol. 13, pp. 201,305,381, 1926.

[103] A.J. Ghajar and C.C. Tang, "Importance of non-boiling two-phase flow heat transfer in pipes for industrial applications", *Heat Transfer Engineering*, vol. 31, no. 9, pp. 711–732, 2010.

[104] J. Gylys, T. Zdankus, I. Gabrielaitiene, and S. Sinkunas, "Experimental research of heat transfer from an in-line tube bundle to a vertical foam flow", *Heat Transfer Research*, vol. 40, no. 5, pp. 455–472, 2009.

[105] M. I. Mishchenko, L. D. Travis, and A. A. Lacis, *Scattering, Absorption, and Emission of Light by Small Particles*, Cambridge University Press, Cambridge, UK, 2002.

[106] M.I. Mishchenko, D.W. Mackowski, and L.D. Travis, "Scattering of light by bispheres with touching and separated components", *Applied Optics*, vol. 34, no. 21, pp. 4589–4599, 1996.

[107] S. Manickavasagam and M. P. Mengüç, "Scattering matrix elements of fractal-like soot agglomerates", *Applied Optics*, vol. 36, no. 6, pp. 1337–1351, 1997.

[108] M. I. Mishchenko, G. Videen, V. A. Babenko, N. G. Khlebtsov, and T. Wriedt, "T-matrix theory of electromagnetic scattering by particles and its applications: a comprehensive reference database", *Journal of Quantitative Spectroscopy and Radiative Transfer*, vol. 88, no. 1-3, pp. 357–406, 2004.

[109] D. W. Mackowski and M. I. Mishchenko, "Calculation of the T-matrix and the scattering matrix for ensembles of spheres", *Journal of the Optical Society of America A*, vol. 13, no. 11, pp. 2266–2278, 1996.

[110] D. W. Mackowski, "Calculation of total cross-sections of multiple-sphere clusters", *Journal of the Optical Society of America A*, vol. 11, no. 11, pp. 2851–2861, 1994.

[111] B. N. Khlebtsov, V. A. Khanadeyev, J. Ye, D. W. Mackowski, G. Borghs, and N.G. Khlebtsov, "Coupled plasmon resonances in monolayers of metal nanoparticles and nanoshells", *Physical Review B*, vol. 77, no. 3, pp. 035440, 2008.

[112] L. L. Zhao, K. L. Kelly, and G. C. Schatz, "The extinction spectra of silver nanoparticle arrays: influence of array structure on plasmon resonance wavelength and width", *Journal of Physical Chemistry B*, vol. 107, no. 30, pp. 7343–7350, 2003.

[113] H. Kimura, L. Kolokolova, and I. Mann, "Optical properties of cometary dust: constraints from numerical studies on light scattering by aggregate particles", *Astronomy and Astrophysics*, vol. 407, no. 1, pp. L5–L8, 2003.

[114] E. Lee and L. Pilon, "Absorption and scattering by long and randomly oriented linear chains of spheres", *Journal of the Optical Society of America A*, vol. 30, no. 9, pp. 1892–1900, 2013.

[115] R. L. Heng, E. Lee, and L. Pilon, "Radiation characteristics and optical properties of filamentous cyanobacterium anabaena cylindrica", *Journal of the Optical Society of America A*, vol. 31, pp. 836–45, 2014.

[116] R. L. Heng, K. Cheong Sy, and L. Pilon, "Absorption and scattering by bispheres, quadspheres, and circular rings of spheres and their equivalent coated spheres", *Journal of the Optical Society of America A*, vol. 32, pp. 46–60, 2015.

[117] M. I. Mishchenko, L. Liu, B. Cairns, and D. W. Mackowski, "Optics of water cloud droplets mixed with black-carbon aerosols", *Optics Letters*, vol. 39, no. 9, pp. 2607–2610, 2014.

[118] K.N. Liou, Y. Takano, and P. Wang, "On geometric optics and surface waves for light scattering by spheres", *Journal of Quantitative Spectroscopy and Radiative Transfer*, vol. 111, pp. 1980–9, 2010.

[119] K.N. Liou, Y. Takano, and P. Wang, "Light absorption and scattering by aggregates: Application to black carbon and snow grains", *Journal of Quantitative Spectroscopy and Radiative Transfer*, vol. 112, pp. 1581–1594, 2011.

[120] K.N. Liou, Y. Takano, C. He, P. Wang, L. R. Leung, Y. Gu, and W. L. Lee, "Stochastic parametrization for light absorption by internally mixed BC/dust in snow grains for application to climate models", *Journal of Geological Research: Atmospheres*, vol. 119, pp. 1581–1594, 2014.

[121] P. Yang and K.N. Liou, "Light scattering by hexagonal ice crystals: solutions by a ray–by–ray integration algorithm", *Journal of the Optical Society of America A*, vol. 14, pp. 2278–89, 1997.

[122] H.A. Nussenzveig and W.J. Wiscombe, "Efficiency factor in Mie scattering", *Physical Review Letters*, vol. 45, pp. 1490–4, 1980.

[123] P. Latimer, "Experimental tests of a theoretical method for predicting light scattering by aggregates", *Applied Optics*, vol. 24, no. 19, pp. 3231–3239, 1985.

[124] R. Kandilian, R.L. Heng, and L. Pilon, "Absorption and scattering by fractal aggregates and by their equivalent coated spheres", *Journal of Quantitative Spectroscopy and Radiative Transfer*, vol. 151, pp. 310–326, 2015.

[125] D. W. Mackowski and M. I. Mishchenko, "A multiple sphere T-matrix Fortran code for use on parallel computer clusters", *Journal of Quantitative Spectroscopy and Radiative Transfer*, vol. 112, no. 13, pp. 2182–2192, 2011.

[126] X. Ma, J. Q. Lu, R. S. Brock, K. M. Jacobs, P. Yang, and X.H. Hu, "Determination of complex refractive index of polystyrene microspheres from 370 to 1610 nm", *Physics in Medicine and Biology*, vol. 48, no. 24, pp. 4165–4172, 2003.

[127] S. Auvinen, M. Alatalo, H. Haario, E. Vartiainen, J. P. Jalava, and R. J. Lamminmäki, "Refractive index functions of TiO_2 nanoparticles", *The Journal of Physical Chemistry C*, vol. 117, pp. 3503–3512, 2013.

[128] G. E. Jellison, L. A. Boatner, J. D. Budai, B. S. Jeong, and D. P. Norton, "Spectroscopic ellipsometry of thin film and bulk anatase (TiO_2)", *Journal of Applied Physics*, vol. 93, pp. 9537–9541, 2003.

[129] G. Mie, "Beiträge zur optik trüber medien, speziell kolloidaler metallsungen", *Annalen der Physik*, vol. 25, no. 3, pp. 377–445, 1908.

[130] A. L. Aden and M. Kerker, "Scattering of electromagnetic waves from two concentric spheres", *Journal of Applied Physics*, vol. 22, no. 10, pp. 1242–1246, 1951.

[131] C. Mätzler, "Matlab functions for Mie scattering and absorption, version 2", *Institut fur Angewandte Physik Research Report No.*, pp. 1497–1505, 2002.

[132] M. Kerker, *The Scattering of Light, and other Electromagnetic Radiation*, Academic Press, New York, NY, 1969.